CRANFIELD UNIVERSITY

SAM OWENS

THICK-FILM PIEZOELECTRIC BIMORPH ACTUATORS FOR MEMS DEVICES

SCHOOL OF APPLIED SCIENCES

PhD THESIS

CRANFIELD UNIVERSITY

SCHOOL OF APPLIED SCIENCES

PhD THESIS

2008-11

SAM OWENS

Thick-film piezoelectric bimorph actuators for MEMS devices

Supervisor: Dr Stephen A. Wilson

August 2011

Abstract

Active flow control can be used to improve the aerodynamic efficiency of passenger aircraft, road traffic and wind turbines amongst other applications. This work describes the fabrication of an ultra-compact microvalve that has been designed as part of an active aerodynamic flow control system that generates airjets of a scale and velocity that have been shown to have desirable effects on the macroscopic air flow. The design of the microvalve is based on criteria specified by the requirements of active flow control and the piezoelectric bimorph actuator which opens and closes the valve outlet.

The static and dynamic deflection response of the piezoelectric actuator was investigated along with the tip force generated under static operation. Typical deflections of about $100\mu m$ for a $2 \times 3.75mm$ bimorph and an applied voltage of 60V were observed. A range of silicon reference springs were used to determine the tip force of the bimorph actuators by a well established technique where the force is calculated from the deflection of these springs by the actuator. The normal spring constant of the reference springs was determined using a variety of calibration methods that are described along with their advantages and limitations. The favourable deflection per unit volume ($150\mu m mm^{-3}$) and force per unit volume ($0.012 N mm^{-3}$) generated by the actuators and the relatively low operating voltages required (Vdc=30-60V) make them an attractive option for many MEMS applications.

A microvalve was fabricated using a photostructurable glass-ceramic called Foturan.

Some of the processing conditions of this material were investigated to determine the limitations they would impose on the design of the microvalve. A variable transmission mask was used to selectively control the energy delivered to the Foturan during processing which produced regions of Foturan with different etch rates. The performance of the microvalve under different internal pressures and actuation conditions was investigated using a Pitot probe. A microvalve with an outlet diameter of $260\mu m$ was used to generate a continuous air jet. The pressure distribution in the jet was measured during on-off (Vdc=30-60V) and dynamic operation (Vac=35V, Vdc=30V, f=25-500Hz). Jet velocities greater than $200ms^{-1}$ were measured for internal pressures greater than 60kPa and static actuation voltages greater than 40V.

Acknowledgements

This work could not have been accomplished without the professional and personal support of my supervisor Dr. Stephen Wilson and the valuable guidance of my more experienced colleagues both in and out of the cleanroom. I am especially grateful to Dr Renaud Jourdain who patiently guided me through the foetal stages of the project and Dr. Chris Shaw, Dr. Glen Leighton and Rob Wright who provided much needed assistance and useful conversations. The characterisation of the microvalve could not have been possible without the assistance of Dr. David MacManus who introduced me to the Pitot probe and who patiently helped me to interpret the results. The practical assistance of Andrew Stallard and Matthew Taunt was especially invaluable in setting up equipment and simply getting things done. Finally, my sanity would not have survived this long without the loving support of my wife who never once complained about my unconventional filing system.

Contents

List of Figures

List of Tables

Chapter 1

Introduction

1.1 Objectives

The general goals of this project are to characterise the force/deflection characteristics of a piezoelectric bimorph actuator and to integrate this actuator into a microvalve to control microscale air jets.

The first goal requires the measurement of tip deflection and force generated by the bimorph actuators which are important parameters that must be determined before the actuators can be used in any particular application. Small deflections are easy to measure with commercial sensors, however, sensors to measure small forces (mN) usually operate over a limited range. The tip forces generated by the actuators used in this work are not in the range of commercially available devices and so a bespoke system was developed to measure the actuator force using calibrated reference springs. This method is well known and used in the field of atomic force microscopy (AFM) where the spring constant of the cantilever sensing element is required and calibration software and hardware is often incroporated into the AFM equipment itself. The general principles can be applied to measure the spring constant of much larger reference springs with spring constants of hundreds to thousands of Nm^{-1},

it is simply a matter of selecting one or more of the variety of calibration methods available to suit the range of spring constants being measured. The microvalve was designed to incorporate the bimorph actuators to control microjets with an outlet diameter of around $200\mu m$ for aerodynamic active flow control applications. Active flow control is a relatively new area of aerodynamics which seeks to control the characteristics of the airflow over a surface or around a body by influencing the airflow close to the surface of the body commonly called the boundary layer. While the microvalves were designed for active flow control applications details of the physics of the flow of fluid around a body and the effect of active flow control systems on this flow is outside of the scope of this report, all that needs to be accomplished here is to design a microvalve that satisfies the performance criteria specified by the aerodynamicists. The microvalve was designed to be fabricated using batch fabrication techniques already common in the MEMS and semiconductor industry which allows large numbers of devices to be fabricated and ensures reproducibility of device performance and which reduces the cost of a single device. The performance of the microvalve was evaluated using a simple and inexpensive Pitot tube which was used to measure the static pressure around the microvalve outlet. The microjets were characterised during static and dynamic actuation of the controlling piezoelectric bimorph under different internal pressures and actuation voltages.

1.2 Thesis Outline

This report will first outline some background information regarding piezoelectric bimorph actuators before describing some contemporary bimorph devices that are commercially available. The tip force generated by the bimorph actuators is determined by measuring the deflection of a calibrated reference spring. The theory describing the use of reference springs and the various means by which their normal spring constants can be experimentally found are described and compared. The

final section describes the micromachining of glass and in particular the use of photostructurable glass ceramics for MEMS devices. The properties and processing requirements of a commercially available photostructurable glass (Foturan) are described. The methodology chapter describes in further detail the fabrication of the piezoelectric actuators, their preparation ready for use and details of the experimental setup used to measure their tip deflection and force. The design and fabrication of the reference springs is then presented along with a simple finite-element-model which is used to model the spring's properties. The following section deals with the methods selected to measure the spring constants and the calculations and corrections that must be used. In the final part of this section the experimental setup used to characterise the microjets is described along with the relevant calculatiions used to determine the exit velocity of the microjet. To conclude the results are interpreted and discussed. Firstly, the spring calibration methods are compared and evaluated. Next, the actuator bahaviour, particularly under dynamic actuation is discussed in light of the electromechanical coupling coefficient and the effective transverse piezoelectric coefficient is determined. The next section discusses the design of the microvalve and the suitability of photostructurable glass as the valve body in light of its processing limitations.

Chapter 2

Background

This chapter will describe the background information necessary in the discussion of piezoelectric bimorph actuators and their characterisation. First the basic principle of operation of piezoelectric materials will be discussed and some bending actuators reported in the literature will be described, focussing particularly on those actuators that are prestressed due to their laminate structure or due to the fabrication methods used in their construction. The tip force generated by the bimorph actuators is an important parameter that must be determined if the actuators are to find suitable applications. This chapter outlines some different approaches to measuring the tip force of a cantilever actuator before focussing on the use of calibrated reference springs. There are a variety of different approaches to determine the spring constant of the reference springs and the static, dimensional and dynamic methods will all be outlined and discussed. These methods can incorporate systematic errors that arise due to the relative position of the actuator to the reference spring, the position of applied loads or masses and the location of the deflection measurements. Fortunately, these errors can be corrected if sufficient information is known about the position and orientation of the actuator and the reference spring. Later in this chapter these sources of error and the necessary correction factors will be discussed. Finally, as the microvalve will be fabricated out of glass a brief outline of the wet

and dry approaches to machining glass will be presented before focussing on photostructurable glass-ceramics, their properties and processing. In particular we will concentrate on the composition and processing of Foturan, a commercially available glass that has often been used in the fabrication of MEMS and microfluidic devices.

2.1 Piezoelectric Materials

Piezoelectricity is observed in crystals with a polar axis and in crystals that develop a polar axis when subjected to mechanical stress. This effect was discovered in 1880-1881 when the brothers Pierre and Paul-Jacques Curie discovered that some crystals generated a surface electric charge when an external force is applied. This is known as the *direct piezoelectric effect*. A year later the *converse piezeoelectric effect* was discovered where an applied electric field can be used to induce a strain in a crystal. So called piezoelectric crystals can therefore be used as both sensors (to produce an electrical signal in response to a change in its physical state) and actuators (to produce a change in its physical state in response to an applied signal).

Quartz is a single crystal piezoelectric material and has been used as a transducer material for some time, however, in polycrystalline form it does not exhibit piezoelectric properties as the piezoelectric effect is dependent on the polar axis and in a polycrystalline ceramic the polar axes are randomly orientated. In ferroelectric materials this is also true, however, the polar axes can be reorientated under the influence of an external electric field thereby producing a net polar axis. Above a certain temperature called the *Curie temperature*, T_c the polarisation disappears and the ceramic loses its piezoelectric properties. This is because most commercially available piezoelectric ceramics have the *Perovskite* structure ABO_3 shown in Fig. 2.1 where A is a 2+ ion, B is a 4+ ion and O is a 2- oxygen ion. Above T_c the material changes to a symmetrical *cubic* structure which does not have piezoelectric properties. Below T_c the crystal changes to a *tetragonal* structure which extends the unit cell in the c direction and compresses it in the a direction. The unit cell is now asymmetric which results in a dipole moment either parallel or antiparallel to the c axis. This is because the central B ion sits in a bistable potential well (see Fig. 2.2) and may change the local polarisation direction by hopping between minima if an electric field is applied (this does not occur if a mechanical stress is applied). It should be noted that as the piezoelectric material is cooled below T_c there is an

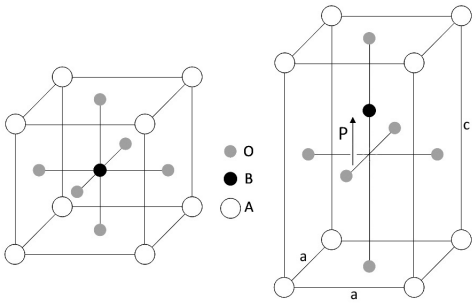

Fig. 2.1: The Perovskite structure.

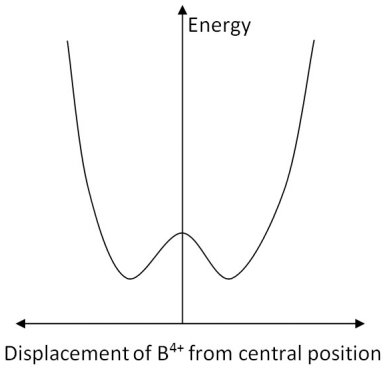

Fig. 2.2: The potential well seen by the central species in the Perovskite structure.

equal probability that the central ion will be displaced along the three orthogonal a-axes, in the positive or negative direction.

The surface charge that appears as a result of the polarisation produces an electric field that is antiparallel to the polar axis and hence is called the *depolarising field*. To minimise the electrostatic energy of the dipole the material becomes divided into smaller regions of opposite polarity called *domains*, the interface between different domains is called a *domain wall* and is of the order of 10nm [1]. In this case the polarisation of adjacent domains is antiparallel and so they are called 180° domains (see Fig. 2.3).

If an external electric field is large enough and the material is a single crystal the

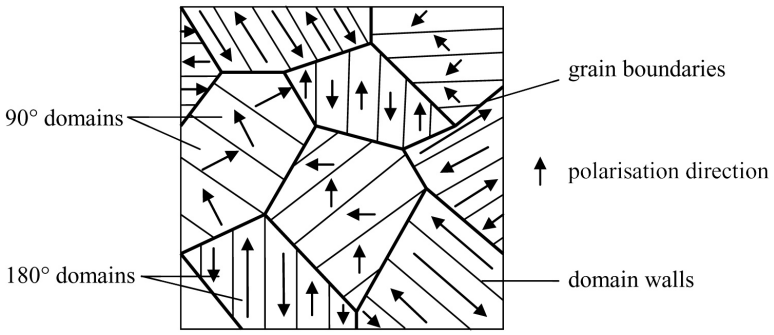

Fig. 2.3: The polycrystalline structure of a ferroelectric ceramic.

domains with their polar axis parallel to the field will grow and the antiparallel domains will shrink until a single domain is formed. Clearly the antiparallel-parallel switching of the 180° domains has a large effect on the polarisation, however, there is no change in strain after switching as the overall dimensions of the unit cell have not changed. There are also regions where the domains are 90° to each other. Switching of the 90° domains has a smaller effect on the polarisation, however, the different lengths of the a and c axes produces an increase in strain in the new direction and therefore a reduction in strain in the direction prior to switching. Externally applied mechanical stresses lead to the appearance of 90° domains which orientate themselves so as to minimise the strain.

In contrast with single crystal piezoelectric materials, polycrystalline ceramics are non-polar because the crystal axes of the individual grains are randomly orientated producing zero net polarisation. The random crystal orientations limit the extent to which the domains within a polycrystalline ceramic can be aligned. While the 180° switching can be almost complete the 90° switching is limited by the changes in strain. The alignment of the domains can be increased by applying a static electric field, usually at some elevated temperature, in a process called *poling*. When the ceramic is cooled and the external field is removed the reorientated domains are 'frozen' into place. This effect can also be observed when a piezoelectric ceramic is actuated at room temperature, when the external field is removed the ceramic

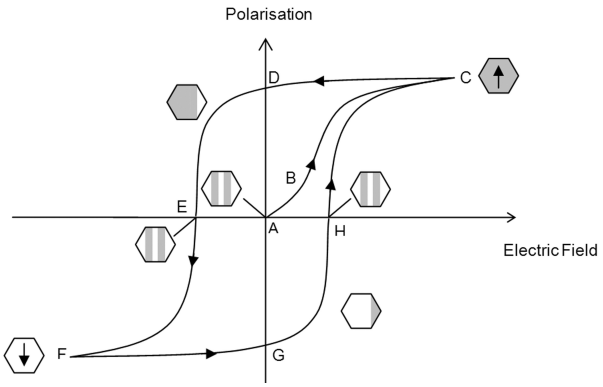

Fig. 2.4: Polarisation hysteresis in a ferroelectric ceramic.

possesess a macroscopic polarisation called the *remanent polarisation* which arises due to the domain switching. The macroscopic polarisation of the ceramic can also be reduced by applying an external field that is antiparallel to its polarisation direction or by applying an external stress to induce an internal field, this can result in the ceramic being *depoled* which will reduce the piezoelectric response of the ceramic.

A consequence of ferroelectric domain reorientation is a nonlinear relationship between the polarisation and the applied electric field and *hysteresis* where the present state of the material properties is dependent on the history of the material. In Fig. 2.4 we see a typical polarisation hysteresis loop for a piezoelectric ceramic. In the non-polarised state (A) the domains are statistically orientated producing no net polarisation. At small fields the polarisation increases linearly with the magnitude of the field (A-B), however, the field is not strong enough to cause domain switching. As the field strength increases the polarisation of some domains will align themselves as close to the field's orientation as is possible. The polarisation in this region increases nonlinearly until all of the domains are aligned and the polarisation saturates (C). As the field is decreased some of the domains will switch back to their original orientation, however, the polarisation has some magnitude at zero field called the *remanent polarisation,* P_r (D). To achieve zero polarisation the field must have a

certain magnitude called the *coercive field strength* (E). As the field continues to increase in magnitude the domains will once again align and reach saturation (F) and will gradually switch back as the field is increased again. In a perfect material the hysteresis loop would be symmetrical.

2.1.1 Piezoelectric Constitutive Equations

In a normal elastic solid the mechanical stress (force per unit area) and strain (deformation per unit length) are directly proportional to each other (Hooke's Law). The constant of proportionality is called the *elastic stiffness constant*. The stress (T_{ij}) and strain (S_{kl}) are second rank tensors and therefore the stiffness constant (c_{ijkl}) is described by a fourth rank tensor. By taking into account tensor symmetry ($T_{ij} = T_{ji}$) and the fact that some of the crystal properties are the same along certain axes (crystal symmetry), the considerable number of constants can be reduced. In a normal solid the electric flux density, called the electrical displacement D is related to the electric field by:

$$D = \epsilon_r \epsilon_0 E \tag{2.1}$$

where ϵ_r and ϵ_0 are the relative permittivity and the dielectric constant respectively. In piezoelectric materials Hooke's Law no longer holds true as electrical and mechanical parameters are coupled so that an electric field can produce a mechanical deformation (strain) and vice versa. Hooke's Law must therefore be extended to include this contribution, which leads to what are known as the *constitutive piezoelectric equations*. These equations relate the coupling between the mechanical properties (stress T_{ij} and strain S_{ij}) and the electrical properties (electrical field E_i and electrical displacement D_i). This gives rise to four pairs of equations, known as the *constitutuve piezoelectric equations*:

$$S_{ij} = s^E_{ijkl} T_{kl} + d_{kij} E_k \tag{2.2}$$

$$D_j = d_{jkl} T_{kl} + \epsilon^T_{jk} E_k \tag{2.3}$$

$$T_{ij} = c^E_{ijkl} S_{kl} - e_{kij} E_k \tag{2.4}$$

$$D_j = e_{jkl} S_{kl} + \epsilon^S_{jk} E_k \tag{2.5}$$

$$S_{ij} = s^D_{ijkl} T_{kl} + g_{kij} D_k \tag{2.6}$$

$$E_j = -g_{jkl}T_{kl} + \beta^T_{jk}D_k \tag{2.7}$$

$$T_{ij} = c^D_{ijkl}S_{kl} + g_{kij}D_k \tag{2.8}$$

$$E_j = -h_{jkl}S_{kl} + \beta^S_{jk}D_k \tag{2.9}$$

where s_{ijkl} is the elastic compliance and the superscript indicates whether this quantity is measured at constant electrical field E or constant electric displacement D. The elastic stiffness is c_{ijkl} at constant stress or strain, ϵ_{jk} is the dielectric permittivity at constant stress or strain and β_{jk} is the dielectric impermittivity at constant stress or strain. The constants of proportionality d_{ijk}, e_{ijk}, g_{ijk} and h_{ijk} relate the mechanical properties to the electrical properties with the subscripts $i, j, k = 1$ to 3. The tensor notation is often simplified into matrix notation by replacing ij and kl with p and q respectively, where $p, q = 1, 2, 3, 4, 5, 6$ in the following way:

ij or kl	11	22	33	23 or 32	31 or 13	12 or 21
p or q	1	2	3	4	5	6

The subscripts and coefficients can often be simplified by the crystallographic symmetry of the piezoelectric material, for example for cylindrically poled lead-zirconate-titanate (PZT) the non-zero coefficients are d_{31}, d_{33}, d_{15}, e_{11}, e_{13}, s_{12}, s_{13}, s_{33}, s_{44}. The material properties of PZT can therefore be written as [2]:

Elastic compliance matrix

$$s^E_{pq} = \begin{matrix} s_{11} & s_{12} & s_{13} & 0 & 0 & 0 \\ s_{12} & s_{11} & s_{13} & 0 & 0 & 0 \\ s_{13} & s_{13} & s_{33} & 0 & 0 & 0 \\ 0 & 0 & 0 & s_{44} & 0 & 0 \\ 0 & 0 & 0 & 0 & s_{44} & 0 \\ 0 & 0 & 0 & 0 & 0 & 2\left(s_{11} - s_{12}\right) \end{matrix} \tag{2.10}$$

Elastic stiffness matrix

$$c_{pq}^{E} = \begin{matrix} c_{11} & c_{12} & c_{13} & 0 & 0 & 0 \\ c_{12} & c_{11} & c_{13} & 0 & 0 & 0 \\ c_{13} & c_{13} & c_{33} & 0 & 0 & 0 \\ 0 & 0 & 0 & c_{44} & 0 & 0 \\ 0 & 0 & 0 & 0 & c_{44} & 0 \\ 0 & 0 & 0 & 0 & 0 & 2\left(c_{11} - c_{12}\right) \end{matrix} \tag{2.11}$$

Piezoelectric coefficient matrix

$$d_{jq}^{E} = \begin{matrix} 0 & 0 & 0 & d_{15} & 0 & 0 \\ 0 & 0 & d_{15} & 0 & 0 & 0 \\ d_{31} & d_{31} & d_{33} & 0 & 0 & 0 \end{matrix} \tag{2.12}$$

Piezoelectric constant matrix

$$e_{jq}^{E} = \begin{matrix} 0 & 0 & 0 & e_{15} & 0 & 0 \\ 0 & 0 & e_{15} & 0 & 0 & 0 \\ e_{31} & e_{31} & e_{33} & 0 & 0 & 0 \end{matrix} \tag{2.13}$$

Permittivity matrix

$$\epsilon_{jq}^{E} = \begin{matrix} \epsilon_{11} & 0 & 0 \\ 0 & \epsilon_{22} & 0 \\ 0 & 0 & \epsilon_{33} \end{matrix} \tag{2.14}$$

2.1.2 Piezoelectric Bimorph Actuators

A volume of piezoelectric material can be made to expand or contract depending on the orientation of the electric field relative to its internal polarisation. The expansion or contraction arises from the alignment of domains with the electric field which either increases or decreases the total strain in the direction of the electric field. Fig. 2.5 illustrates how a piezoelectric layer *contracts* laterally when the polarisation is *parallel* to the electric field in the 3-direction. The same ceramic layer would *expand* if its polarisation was *antiparallel* to the applied electric field.

The expansion or contraction of a piezoelectric plate cannot be increased indefinitely by simply increasing the applied electric field. The extent of the expansion or contraction of a piezoelectric ceramic layer is limited by domain switching. Take the example of the d_{31} mode of actuation illustrated in Fig. 2.5 where the polarisation direction is antiparallel to the applied field. As the electric field is increased from zero the ceramic layer expands in the plane of the layer until the applied field is strong enough to produce domain switching. As the polarisation direction of a domain switches through 180° the mode of actuation changes and the ceramic layer now contracts in the plane of the layer reversing the direction of the tip deflection.

The expansion and contraction of piezoelectric ceramic layers is exploited in a common device called the *piezoelectric bending actuator*. These actuators are cantilevers that use the expansion or contraction of single or multiple piezoelectric layers to generate a tip deflection perpendicular to the long axis of the actuator. The different poling configurations of these bending actuators are presented in Fig. 2.6. In a *unimorph* bender a thin piezoelectric layer is bonded to an elastic passive (non-piezoelectric) material. A *bimorph* consists of 2 layers of piezoelectric material in the form of thin plates that are bonded to each other or to a third passive layer, called a shim, that improves its mechanical reliability. The domain

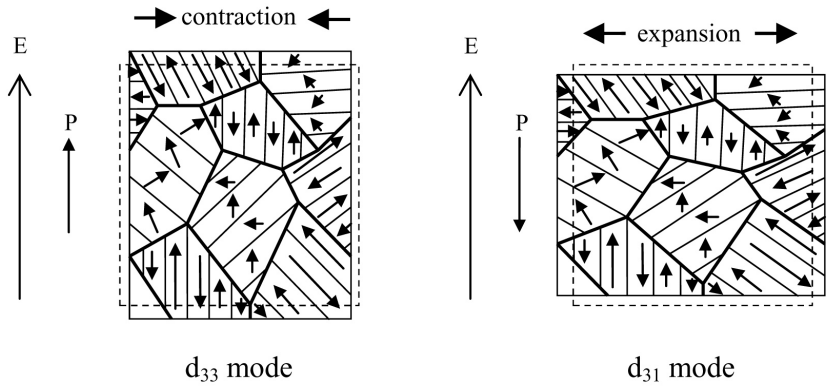

Fig. 2.5: Expansion and contraction of a piezoelectric ceramic depends on the relative orietation of the polarisation to the external electric field.

switching described above can be observed in practice as a sudden reversal in the direction of the tip deflection of a bending actuator.

When actuating a bimorph there are two possible configurations depending on the polarisation of the piezoelectric layers and the electrode configuration. As shown in Fig. 2.7 the piezoelectric layers can be connected in *series* where they have opposite polarisations and an electric field is applied across the full thickness of the device. If the piezoelectric layers have the same polarisation direction they are connected in *parallel* by applying the electric field across each layer seperately and in opposite directions. Both of these configurations achieve the same thing, that is forcing one piezoelectric layer to expand while the other contracts thereby deforming the whole structure.

Analytical equations describing the behaviour and properties of piezoelectric layered actuators repeatedly appear in the literature. We are not going to compare these different physical and mathematical approaches to analyse these actuators as we wish only to predict some simple properties of our bimorph actuators for the purpose of designing an actuator suitable for a microvalve. A definitive discussion of bimorph theory has been written by Wang and Cross who presented a detailed derivation of the resonance frequency, tip deflection and blocking force which will

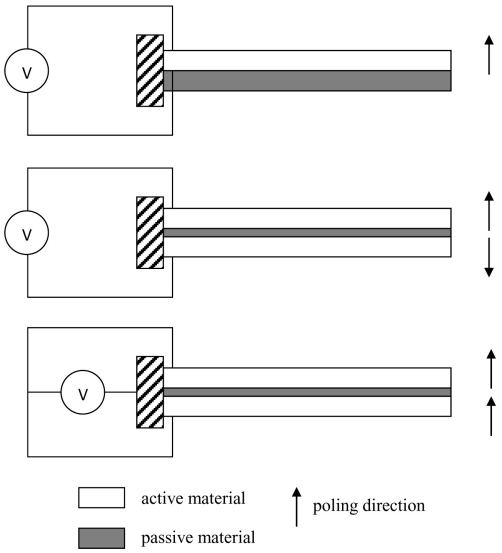

Fig. 2.6: The different configurations of unimorph (top) and bimorph (middle and bottom) bending actuators. In the bimorph the active layers can be connected in series (middle) or in parallel (bottom).

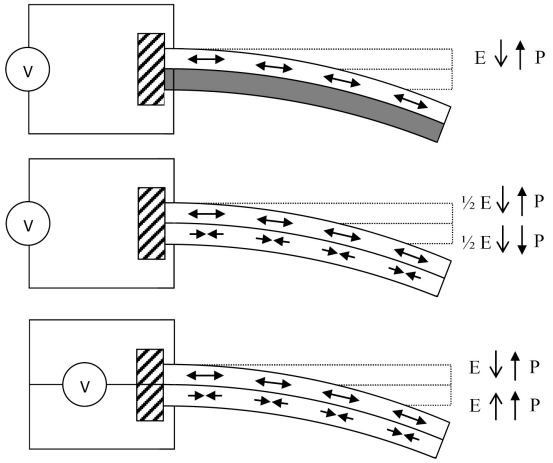

Fig. 2.7: The bending of unimorph and bimorph actuators arises from the relative orientation of the external field to the polarisation direction. In the unimorph the active layer expands or contracts acting against the passive elastic layer. In the bimorph one layer contracts while another layer expands.

be briefly outlined here [3].

To derive an expression for the fundamental resonance frequency of a bimorph Wang and Cross used the transformed cross-section method [4]. This method transforms the cross-section of a composite beam of different materials into an equivelent beam of a single material. As a result the width of the layers are modified in proportion to the ratio of the Young's modulus of the two different materials. In the case of a bimorph the width of the middle elastic layer is changed by a factor of E_m/E_p where E_m and E_p are the Young's moduli of the metal shim and the piezoelectric layers respectively. The bimorph now behaves as if it was made of one material with Young's modulus E_p. The resonance frequency of a beam of length L of uniform cross-section and mass per unit length m is:

$$f_i = \frac{\lambda_i^2}{2\pi \mathrm{L}^2} \left(\frac{E_P I_C}{m} \right)^{1/2} \tag{2.15}$$

where λ_i is a constant that depends on the mode of vibration denoted by i. For the fundamental mode of vibration $\lambda_1 = 1.875$. The mass per unit length of a bimorph can be written as:

$$m = w(t_m \rho_m + t_p \rho_p) \tag{2.16}$$

where t_m and t_p and ρ_m and ρ_p are the thicknesses and densities of the metal and piezoelectric layers respectively. The term $E_P I_C$ in equation 2.15 is called the *flexural rigidity* which, for a composite beam with a bimorph structure, is given by:

$$E_P I_C = \frac{w E_P}{2} \left(\frac{t_p^3}{3} + t_p (t_m + t_p)^2 + \frac{E_m}{E_p} \frac{t_m^3}{6} \right) \tag{2.17}$$

By substituting 2.16 and 2.17 into 2.15 we obtain:

$$f_0 = \frac{3.52 t E_P^{1/2}}{4\pi L^2} \left(\frac{2t_p^3 + 6t_p(t_m + t_p)^2 + (E_m/E_p)\, t_m^3}{3\,(t_m \rho_p + 2t_p \rho_p)} \right)^{1/2} \tag{2.18}$$

For a bimorph without an elastic layer this reduces to:

$$f_0 = \frac{3.52t}{4\pi L^2}\sqrt{\frac{E_P}{3\rho_P}} \tag{2.19}$$

To obtain an expression for the tip displacement δ of a bimorph we need to know the curvature of the beam which is defined as:

$$\kappa = \frac{d^2\delta}{dx^2} \tag{2.20}$$

where δ is the vertical displacement of the midplane of the bimorph. Wang and Cross derive an expression for the *curvature*, κ, of a bimorph by considering the bending moment and resultant extensional force of the bimorph due to its deformation:

$$\kappa = \frac{12E_P d_{31} E_3 \left(t_m t_p + t_p^2\right)}{2E_P \left(3t_m^2 t_p + 6t_m t_p^2 + 4t_p^3\right) + E_m t_m^3} \tag{2.21}$$

where E_3 is the magnitude of the electric field in each ceramic layer. The displacement of the bimorph at the tip ($x = L$) is therefore:

$$\delta = \frac{\kappa L^2}{2} = \frac{6E_P d_{31} E_3 \left(t_m t_p + t_p^2\right) L^2}{2E_P \left(3t_m^2 t_p + 6t_m t_p^2 + 4t_p^3\right) + E_m t_m^3} \tag{2.22}$$

For a given thickness of the piezoelectric layers the tip deflection drops as the thickness of the elastic layer increases (see Fig. 2.8). If the active layers are the same thickness, an elastic layer of thickness $t_m = 0.4t_p$ is sufficient to increase the mechanical strength with only a small decrease in tip deflection.

When an electric field is applied to the piezoelectric layers the resulting bending moment will deform the bimorph. For most applications it is necessary to know the *blocking force* required to maintain the tip of the actuator in its initial position ($\delta = 0$). The blocking force of a composite beam can be found in many reference works [5]:

$$F_B = \frac{3E_P I_C \delta}{L^3} = \frac{3E_P I_C \kappa}{2L} \tag{2.23}$$

where we have substituted the simple expression for δ found by integrating equation 2.21. The expressions for flexural rigidity (2.17) and curvature (2.21) can now be substituted either analytically or numerically.

When designing a bimorph for a particular application the analytical expressions for the resonance frequency f_0, tip deflection δ and blocking force F_B can be used to determine the optimum dimensions of the active and passive layers and the most appropriate materials for the elastic layer. For example the model devised by Wang and Cross can be used to estimate the capabilities of the bimorph actuators used in this project. For a $2 \times 3.75mm$ bimorph the tip deflection and blocking force as a function of the thickness of the elastic and ceramic layers is shown in Fig. 2.8. The deflection and force are linearly dependent on the shim thickness for a given thickness of the ceramic layers. The blocking force is linearly dependent on the thickness of the active layer, however, the tip deflection is far more sensitive to the thickness of the active ceramic layers. A compromise must therefore be made between tip deflection and tip force depending on the needs of the particular application. It is important to keep in mind that the devices need to be robust enough to be handled and if necessary integrated into a device. Models like this one are only a guide and are limited by knowledge of the material parameters and caution should be exercised when designing devices with thin layers whose elastic properties can differ from the properties and behaviour of bulk materials.

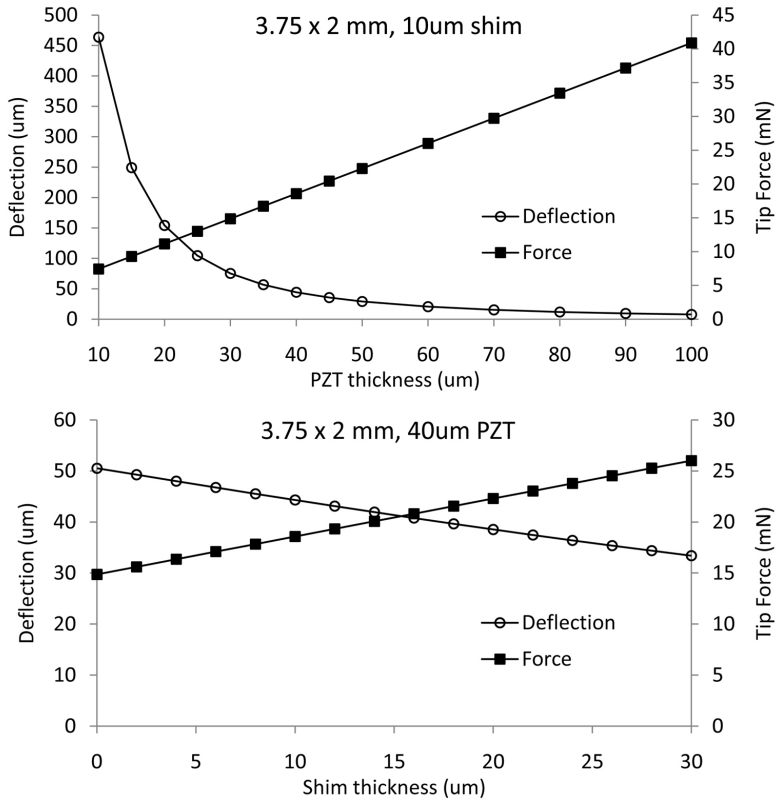

Fig. 2.8: Wang & Cross predictions of the tip deflection and blocking force generated by a bimorph actuator with dimensions $2 \times 3.75mm$.

2.1.3 Prestressed Piezoelectric Actuators

Conventional piezoelectric actuators generally offer large forces and small displacement (multilayer actuators) or large displacement and small forces (bimorphs), however, it was found that actuators that have residual prestresses show improved electromechanical behaviour. These devices generally have a unimorph structure where a piezoelectric ceramic layer is bonded to a substrate with different thermomechanical properties. Here we will briefly outline some prestressed piezoelectric actuators that have been reported over the last 20 years or so (the different electromechanical properties of these devices are tabulated and compared by Juuti [6]).

One of the first of this type of device was called *RAINBOW* which stood for Reduced And INternally Biased Oxide Wafer [7]. These devices are fabricated from a high lead content piezoelectric ceramic wafer such as PZT, which is placed on a graphite plate and baked at high temperature. The graphite chemically reduces the oxides in the ceramic to produce a layer with high metallic lead content. As the remaining PZT and the reduced layer have different coefficients of thermal expansion (CTE), internal stresses are generated when the wafer is cooled which causes the wafer to a form a dome. The wafer can be laser diced to produce actuators of almost arbitrary geometry [8]. It has been reported that the reduced layer is in tension which changes to compression at the interface between the reduced material and the nonreduced ceramic. The d_{31} coefficient varies continuously through the thickness of the device which produces higher displacements than conventional unimorph devices [9]. In 1996 a unimorph was developed around the concept of *RAINBOW* but which required lower processing temperatures. The *CERAMBOW* device (CERAMic Biased Oxide Wafer) consisted of a ceramic layer ($432\mu m$) solder bonded to a brass substrate ($127\mu m$) which was again prestressed due to the thermal mismatch between the layers and which produced greater displacements than a conventional unimorph of the same

dimensions. Around the same time NASA was developing the *THUNDER* device (THin layer composite UNimorph ferroelectric DrivER) which consisted of a PZT ceramic layer which was adhesively bonded on one side to an alumiunium layer and on the other side to a metal backing layer of steel or brass [10]. The adhesive was a polyimid epoxy that was cured at $150°C$ and produced internal stresses as a result of the different CTE. At this time *CRESCENT* was also reported which was another ceramic-epoxy-metal unimorph which required high temperature curing of the epoxy ($250°C$) and which produced larger displacements than a unimorph bonded at room temperature. Yoon *et al* improved upon the *THUNDER* device by making an asymmetrical device using layers of light weight composites which replaced the heavy metal layers and reduced the weight of the devices by 30%. These Lightweight Piezo-composite Curved Actuators (LIPCA) were generally of the glass-carbon-glass-PZT structure which was adhesively bonded and prestressed due to the different CTE [11]. Several different designs of the LIPCA structure have been compared the conclusion being that the ceramic layer and the neutral axis should be as far apart as possible with the ceramic layer placed on the compressive side of the neutral axis because ceramics are stronger in compression than in tension [12]. As the improved deflection of prestressed actuators is attributed to enhancement of the d_{31} coefficient, Li *et al* [13] designed a functionally graded device where the passive material was replaced by layers of PZT or ZnO with different d_{31} parameters. This approach allows the d_{31} gradient to be closely controlled to optimise the actuator performance. The final prestressed device is called PRESTO (PRESTRessed electrOactive component with postfired biasing layer) and uses a sintered ceramic wafer which is constrained by a layer of material in the form of a AgPd electrode or a low temperature co-fired ceramic (LTCC). By using bulk ceramic material without adhesives and with an LTCC constraining layer, observed deflections were less than half that of equivalent *THUNDER* and *RAINBOW* devices.

The actuator used in this investigation is formed by adhesively bonding the active

ceramic and passive titanium layers at elevated temperature which produces a prestress due to the different CTE of the layers, however, it differs from the above devices in that it has a bimorph structure whereas the actuators above are essentially unimorphs. As a bimorph is symmetrical we would expect to see little or no deformation after fabrication as the prestresses are symmetrical about the neutral axis.

2.2 Calibrated Springs - Measuring *k*

The techniques used to determine the normal spring constant k of a cantilever spring can be grouped into three categories: *dimensional* models, *static* methods and *dynamic* methods. The techniques described here are widely used to determine the spring constant of atomic force microscope tips and the majority of the available literature discusses spring calibration in this context. These three different approaches will be briefly outlined along with their relative merits before we consider some of them in more detail.

Dimensional methods calculate the normal spring constant from the material properties and beam dimensions. Static methods involve applying a static or fixed load to the cantilever and measuring the resulting deflection. As the spring constant of the cantilever is defined as the the ratio of the applied force to the resulting deflection, commonly known as *Hooke's Law*, the spring constant can be directly calculated. Dynamic methods involve investigating the vibrational response of the cantilever under various conditions. The advantage of dynamic methods is that knowledge of the material parameters and some dimensional information is not required to derive the normal spring constant. There are several excellent review articles that consider the full spectrum of calibration methods in great detail and the reader is referred to them for further details [14, 15, 16], however, we will briefly outline their application and any outstanding strengths and weaknesses.

In *static* methods a known force is applied to the tip of the cantilever and the spring constant is calculated directly from the tip displacement. One way to apply a known force is to use a precalibrated pendulum and a vertically mounted cantilever. The two are carefully brought into contact and the spring constant is calculated from the deflections of both the pendulum and the cantilever. While this method is mathematically simple there are several practical problems

associated with physically mounting and calibrating the vertical cantilever-pendulum system. The spring constant of the cantilever must first be estimated before the pendulum can be designed as the inaccuracies in this method increase with increasing disparity between the spring constants of the pendulum and the spring. A second method is to bring the unknown cantilever into contact with a precalibrated reference spring with a known spring constant. The spring constant is again determined from the relative deflections of the two springs. This method is much easier to implement in practice, however, the springs need to be very carefully aligned as the point of contact will greatly influence the measured deflection and again the spring constants must be comparable to reduce inaccuracy. The third method is to mount small objects of known mass onto the tip of the cantilever and measure the tip deflection. If the deflection of the beam due to its own mass is assumed to be negligible, at least in comparison with the deflection due to the added mass, then the spring constant can be found from the the tip deflection. This method can be applied to cantilevers of arbitrary shape and unknown spring constant. The problems with this method are that the mass must be carefully positioned on the cantilever tip, often by hand, and fixed, for example with glue, which makes this technique destructive.

Compared to static methods *dynamic* methods are generally more complex as the spring must be driven at a range of frequencies and the amplitude of the spring's vibrations measured. Often there is considerable uncertainty in material properties and cantilever dimensions especially when structures are fabricated from thin films that are difficult to physically characterise. One means of eliminating the need to know these properties is to measure the fundamental resonance frequency of the spring before and after a small mass, usually a microsphere of some material, is attached to the tip of the spring. As long as the mass of the microsphere is known then the normal spring constant can be found from the fundamental resonance. Although this method can be applied to springs of arbitrary shape the positioning of the masses is crucial and very tedious. An alternative is to measure the resonant

frequency in vacuum of an unloaded cantilever. This method has some limitations as the mass of the cantilever is required and the spring must generally be of a single material as the thickness of any deposited layers is difficult to measure accurately. This method has been extended for cantilevers in air by modelling the system as a beam vibrating in a fluid environment. The advantage of this method is that it is nondestructive although this method is considerably more complex mathematically and can only be applied to cantilevers with a rectangular geometry. Even when a spring is not being externally driven it is constantly being driven by its own thermal vibrations. By modelling the cantilever as a simple harmonic oscillator the resulting tip deflection can be measured and used to determine the normal spring constant. This method is widely used to calibrate springs with very low spring constants such as AFM cantilevers as it is noncontact, nondestructuve and can be applied to springs of arbitrary shape. Usually AFM systems are designed to incorporate the necessary hardware and software to calibrate the AFM tips in this way.

As is clear from this short overview there are a variety of methods that can be used to determine the normal spring constant of a spring. The method chosen will depend on the spring geometry, overall dimensions, what is already known about the material properties and spring dimensions, the available equipment and how robust the springs are. Unfortunately most of the theoretically complex techniques can only be used for rectangular cantilevers where $length \gg width \gg thickness$ though there is a considerable amount of literature which extend these techniques mathematically to describe triangular shaped springs.

One of the objectives of this project was to determine the tip force of a piezoelectric bimorph. To this end the reference spring method was used as it suited the equipment and facilities available. The reference springs will be calibrated by means of *dimensional models*, *static added mass method*, and *dynamic methods*. Let us now consider these methods in more detail.

2.2.1 Static Methods

There are three well established methods of applying a static load to a spring to determine its spring constant. The simplest way is to mount a small fixed mass on the tip of the spring and measure its deflection (Fig. 2.9 (a)). To determine the deflection of the beam under its own weight the tip position is measured with the spring mounted upright (that is horizontally), then the tip position is remeasured after rotating the measurement system about the long axis of the spring. The spring deflection due to its own weight is therefore half the difference in deflection between the two positions. The next method is to mount the spring vertically and bring it into contact with a free hanging pendulum (Fig. 2.9 (b)). The spring is moved horizontally to deflect the pendulum and the resulting pendulum and spring deflections are measured. The force exerted on the spring due to the weight of the pendulum can be calculated from the relative deflections using the expression [15]:

$$k_z = \frac{mg}{L}\frac{\Delta Z_P}{\Delta Z_C} \tag{2.24}$$

where m is the mass of the pendulum, g is the acceleraton due to gravity, L is the length of the pendulum, ΔZ_P is the displacement of the pendulum and ΔZ_C is the displacement of the spring.

The pendulum method can be adapted by replacing the pendulum with a reference spring with a known spring constant. The reference spring is brought into contact with the unknown spring and its base is moved a known distance. The sum of the resulting deflections of the reference spring and the unknown spring equal this distance, therefore the spring constant of the unknown spring is found using the following expression:

$$k_z = k_z^{ref}\left(\frac{\Delta Z_{ref}^{base}}{\Delta Z} - 1\right) \tag{2.25}$$

where ΔZ is the deflection of the unknown spring, ΔZ_{ref}^{base} is the known distance that the base of the calibrated spring is moved and k_z^{ref} is the spring constant of

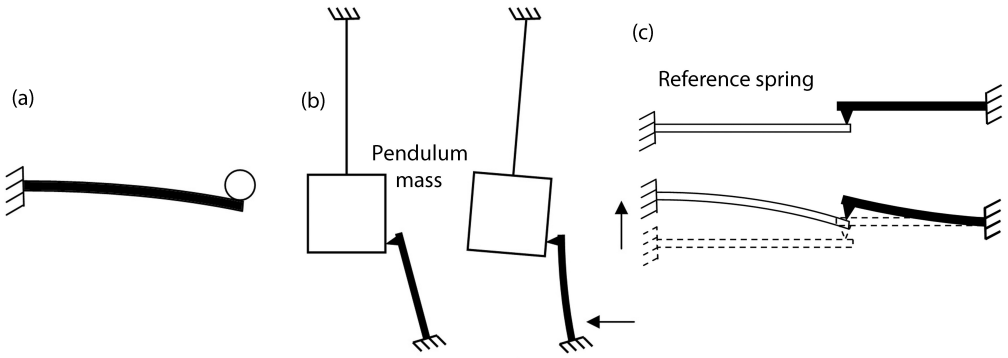

Fig. 2.9: Static methods to determine the normal spring constant of a reference cantilever. Note the deflections and angles have been exaggerated.

the precalibrated spring.

The advantage of these static methods is that they can be applied to springs of arbitrary shape, however the implementation of these methods is difficult in practice. The pendulum method requires the spring to be mounted vertically and a pendulum with a spring constant of a similar magnitude to the unknown spring. This is crucial as the accuracy of this method diminishes as the difference in the spring constants increases. The calibrated cantilever method also requires both springs to have a similar spring constant and the accuracy is also dependent on the positioning and alignment of the springs. Correction factors may have to be applied if the unknown spring has a stylus tip or is brought into contact with the reference spring at an off-end or off-axis position. Finally, the static added mass method does not require an initial estimate of the spring constant, however, it is strongly dependent on the position of the added mass. To determine the deflection due to the springs own mass the measurement system must also be rotated about the spring which is difficult to accomplish in practice.

2.2.2 Dimensional Models

These are the simplest methods to implement and give a good first estimate of the spring constant of a rectangular or V-shaped spring. Generally to use these models it is only necessary to know the material properties of the beam and its dimensions. Ideally the cantilever material is modelled as an isotropic linearly elastic solid which is appropriate for amorphous materials, however, for crystalline materials some caution must be exercised as many materials have anisotropic elastic properties due to their crystal structure. As long as the crystal orientation is fixed in the longitudinal axis of the beam then the elastic properties of the crystal in this orientation can be used.

Let us first consider dimensional models for rectangular cantilevers.
Euler-Bernoulli beam theory yields a simple expression for the normal spring constant k_z of an end loaded thin beam with rectangular cross-section [18]:

$$k_z = \frac{3EI}{L^3} \tag{2.26}$$

where I is the second moment of inertia of the cross-section of the beam and E is the Young's modulus. For a beam of a single material and rectangular cross section I is given by [19]:

$$I = \frac{wt^3}{12} \tag{2.27}$$

where t, w and L are the thickness, width and length of the cantilever respectively. By substituting for the moment of inertia we obtain:

$$k_z = \frac{Et^3w}{4L^3} \tag{2.28}$$

These models usually assume a uniform beam cross-section and that $L \gg w \gg t$. When fabricating cantilevers using anisotropic etching, whether wet or dry, there will always be some undercut or lateral etching which produces a trapezoidal beam

cross-section. This must also be taken into account unless the thickness is extremely small and the width is correspondingly large. Poggi [20] used the Euler-Bernoulli beam equation in conjunction with the second moment of inertia of a trapezoidal beam which is written [21]:

$$I_{trapezoid} = \frac{t^3(a^2 + 4ab + b^2)}{36(a + b)} \tag{2.29}$$

where a is the width of the narrower side and b the width of the longer side of the trapezoid.

To derive a similar analytical description for triangular or V-shaped springs presents a greater challenge. The starting assumption is that the two converging arms of a triangular spring can be approximated by two rectangular beams that are joined at one end. This so-called *parallel beam approximation* (PBA) can be applied in its simplest form by simply doubling the result for a rectangular cantilever [17]. The PBA has been gradually refined to remove ambiguities associated with the spring shape as most AFM probes are A-shaped rather than V-shaped and therefore the results depend on the choice of length and width used, for example, L can be defined as the length of each skewed arm or as the length of the arm perpendicular to the base. The shorter the arms the more ambiguous the result as the contact area between the beams increases. There are a number of different analytical expressions in the literature, we will use that of Sader which includes the skew angle of the beams [17]:

$$k_z = \frac{Ewt^3}{2L^3} cos\theta \left(1 + \frac{4w^3}{b^3}\left(3cos\theta - 2\right)\right)^{-1} \tag{2.30}$$

where b is the width at the base of the triangle, θ is the half angle between the arms and w is the width of each arm measured parallel to the edge of the substrate rather than perpendicular to the edge of the arm. This expression assumes uniform parallel bending whereas in the case of a V-shaped spring the inside edges

of the beams bend inwards more than the outer edges ands the beams become warped. The benefits of taking this so-called anticlastic bending into account may be outweighed by the increase in complexity of this approach.

2.2.3 Dynamic Methods

The accuracy of the dimensional models depends on how accurately the geometry of the springs is known. The difficulty in accurately measuring the thickness of a rectangular beam can be addressed by substituting the spring constant into the expression for the resonance frequency of a simple harmonic oscillator which gives:

$$f_0 \approx \frac{t}{2\pi L^2}\left(\frac{E}{\rho}\right)^{\frac{1}{2}} \tag{2.31}$$

where ρ is the density of the cantilever (this can be compared to 2.19 for a piezoelectric bimorph with no elastic layer). If this expression is rearranged for t this can be substituted into the Euler-Bernoulli result for k_z to give:

$$k_z \approx \frac{2\pi^3 w\left(f_0 L\sqrt{\rho}\right)^3}{\sqrt{E}} \tag{2.32}$$

A more accurate expression for the resonant frequency in vacuum is used by Clifford and Seah [17]:

$$f_0 = \frac{a_1^2}{2\pi\sqrt{12}}\sqrt{\frac{Et^3}{L^4\rho}} \tag{2.33}$$

where $a_1 = 1.8751$. This results in a more accurate expression for k_z:

$$k_z = a_2 w\frac{\left(Lf_0\sqrt{\rho}\right)^3}{\sqrt{E}} \tag{2.34}$$

which simply replaces the factor of $2\pi^3$ (62.0126) with a_2 =59.3061.

The *dynamic added-mass* or *Cleveland* method exploits the dependence of the resonant frequency on the mass of the beam by changing the mass and measuring the change in resonant frequency. For a simple harmonic oscillator the resonant frequency is related to the mass of the oscillator by the following:

$$f = \frac{1}{2\pi}\sqrt{\frac{k}{m+m^*}} \tag{2.35}$$

where k is the spring constant, m^* is the *effective mass* of the cantilever beam and m is an additional mass positioned at the end of the beam. The effective mass of a cantilever beam arises because the beam becomes stiffer closer to its base and as a result not all of the beam length oscillates with the same amplitude which effectively reduces the mass of the beam by a factor 33/140. By rearranging 2.35 we obtain

$$m = \frac{k}{(2\pi f)^2} - m^* \tag{2.36}$$

If several masses are used and the resonant frequency is determined for each new mass then a plot of m against $1/(2\pi f)^3$ would produce a straight line with gradient k. This process can be very time consuming so often the resonant frequency is found before and after a single mass is added to the beam. In this case when the beam is unloaded $m = 0$ and $f = f_0$ giving:

$$m^* = \frac{k}{(2\pi f_0)^2} \tag{2.37}$$

When a mass of $m = m_1$ is added to the beam the resonant frequency becomes $f = f_1$

$$k_z = (2\pi f_1)^2 (m_1 + m^*) \tag{2.38}$$

These combine to eliminate the effective mass m^* to give

$$k_z = \frac{(2\pi)^2 m_1}{1/f_1^2 - 1/f_0^2} \tag{2.39}$$

The accuracy of this method is determined by the positioning of the end loaded mass and the measurement of the end masses. The further from the end of the beam that the added mass is placed the smaller its effect will be on the resonant frequency. The size of the added mass placed a distance ΔL from the end of the spring can be corrected to give the equivalent mass at the very tip of the beam using:

$$m_{eff} = m_{meas} \left(\frac{L - \Delta L}{L} \right)^3 \tag{2.40}$$

where L is the beam length, ΔL is the off-end distance of the added mass, m_{meas} is the measured mass of the added microsphere and m_{eff} is the *effective mass* at the beam tip. This error can be considerable depending on the length of the cantilever, the shorter the cantilever the larger this errror will be for a given off end distance. The second source of error is in the measurement of the added mass. The mass is normally determined by optically measuring the diameter of the added microsphere, calculating its volume and then using its density to determine its mass. Generally these microspheres are not perfectly spherical so the diameter of the major and minor axes are measured and the average diameter found from $D_{av} = \sqrt{D_1 D_2}$. This method also assumes that the microspheres are fully dense without voids or pores and surface deformities.

The *thermal tune* method is perhaps the most widely used as the required software and hardware are often built into commercial AFMs. This method applies the equipartition theorem to the beam motion which relates the thermal vibrations of the cantilevers fundamental mode to its thermal energy:

$$k_D = \frac{k_B T_0}{\langle \Delta z^2 \rangle} \tag{2.41}$$

where k_B is the Boltzmann constant, T is the temperature and $\langle \Delta z^2 \rangle$ is the mean square displacement of the cantilevers free end and k_D is the dynamic spring constant. The dynamic spring constant is related to the static spring constant and depends on the mode of vibration and the geometry of the cantilever, however, for the fundamental mode of a rectangular cantilever $k_D = 1.03 k_z \approx k_z$ as the beam deflection due to a static load is similar to the shape of the fundamental mode of vibration of a rectangular cantilever. This approximation does not hold for higher order vibration modes. The mean square displacement is found by integrating the power spectral density (PSD) over the resonance peak. The PSD shows the power density distribution in the frequency domain of the thermal vibrations of the beam. Broadband noise sources can simply be subtracted and sources at discrete

frequencies can be ignored as long as they are sufficiently far away from the resonance peak. The noise can be eliminated by fitting the well known expression for the thermal noise power spectral density of a simple harmonic oscillator to the response of the cantilever at its fundamental resonance:

$$PSD\left(\omega\right) = A + \frac{B\omega_0^4}{\left(\omega^2 - \omega_0\right)^2 + \frac{\omega^2\omega_0^2}{Q^2}} \tag{2.42}$$

where A, B, ω_0 and Q are fitting parameters. The parameter A represents the broadband white noise, ω_0 is the resonance frequency and Q is the quality factor which is the ratio of the peak height to its full width at half maximum. Q should be $\gg 1$ which means that the vibrations are not overly damped. The mean square displacement $\langle \Delta z^2 \rangle$ can be found by integrating the second term in 2.42 over the frequency domain. Two modifications to the thermal tune method were necessary. Firstly, cantilevers are not ideal springs so the energy of their oscillatory modes is not the same as that of a simple harmonic oscillator. Secondly, the displacement of the cantilever tip is measured by the optical lever method which involves bouncing a laser beam off the surface of the spring which then illuminates a detector, as the spring moves the laser spot moves across the detector. The motion of the cantilever is not perpendicular to the path of the laser so the measured deflection is not the real deflection of the cantilever as there are angular changes dependent on its bending mode. The finite spot size of the laser will also introduce an uncertainty, however this only becomes important for small cantilevers of a few $100\mu m$ in length [22]. The thermal oscillations of a cantilever beam will contain noise contributions from all vibrational modes. Butt and Jaschke take all these modes into account to calculate the total thermal noise as measured using the optical lever technique [23]:

$$\langle \Delta z^{*2} \rangle = \frac{16 k_B T}{3\alpha_i^2 k} \sum_{i=1}^{\infty} \left(\frac{sin\alpha_i sinh\alpha_i}{sin\alpha_i + sinh\alpha_i} \right)^2 \tag{2.43}$$

where α_i are constants that depend on the mode of oscillation (i=1 for the fundamental). This can be simplified by numerically evaluating the summation

term which is 1/4 for a free cantilever:

$$\sqrt{\langle \Delta z^{*2} \rangle} = \sqrt{\frac{4k_B T_0}{3k}} = \sqrt{\frac{4}{3}\langle \Delta z^2 \rangle} \tag{2.44}$$

where $\sqrt{\langle \Delta z^{*2} \rangle}$ is the root-mean-square deflection of the beam as measured with the optical lever technique, k is the spring constant and $\sqrt{\langle \Delta z^2 \rangle}$ is the rms deflection of the beam due to thermal vibrations. The first 10 vibration modes of the beam account for 99.93% of the rms deflection $\langle \Delta z^2 \rangle$ and 96% of $\langle \Delta z^{*2} \rangle$. Proksch points out that it is unnecessary to consider the higher modes as real vibration measurements have a finite bandwidth which will simply not detect higher vibrational modes and that other noise contributions from ambient or electronic sources will also be detected [22].

Another dynamic technique that is considerably less complex is the *unloaded dynamic frequency method* which relates the resonance frequency of the cantilever in vacuum to the spring constant:

$$k_z = M_{eff} m \omega_{vac}^2 \tag{2.45}$$

where m is the mass of the cantilever, ω_{vac} is the radial resonant frequency of the fundamental mode of the beam in vacuum and M_{eff} is the normalised effective mass of the beam [24]. For a cantilever with aspect ratio $L/w > 5$ the normalised effective mass is 0.2427. This simple method has some practical difficulties in that the mass of the cantilever must be calculated from the beam dimensions which may require time consuming optical and SEM measurements of beam dimensions. Metal coatings on the cantilevers will also lead to errors as the thickness of these coatings can be difficult to accurately determine. Sader eliminated the need to know the cantilever's mass by describing a rectangular cantilever oscillating in a fluid environment. In this model only the plan view dimensions of the beam are needed, the quality factor in the fluid Q_f and the density and viscosity of the fluid

in which the measurements are made. As in the thermal tune method $Q \gg 1$ and $L \gg w \gg h$, however in practice the results hold for aspect ratios of $L/w > 3$. Sader's result for the spring constant is [25]:

$$k = 7.5246\rho_f w^2 L Q_f f_0^2 \Gamma_i(Re) \tag{2.46}$$

where Re is the Reynold's number, a dimensionless variable that is the ratio of the inertial forces in a fluid to the viscous forces and for a cantilever is given by:

$$Re = \frac{2\pi\rho_f f_0 w^2}{4\eta_f} \tag{2.47}$$

where ρ_f the density of the fluid, f_0 the resonance frequency of the beam, w the beam width and η_f the viscosity of the fluid. Γ_i is the imaginary component of the *hydrodynamic function* which is a function of the Reynold's number. The hydrodynamic function is dimensionless and is obtained by solving the equations of motion of the fluid for an infinitely long rigid beam oscillating transversely in a fluid. Sader used the exact analytical result for a rigid beam with a circular cross-section and introduced a correction function to give the hydrodynamic function of a rectangular beam. As the hydrodynamic function is considerably complex an online calculator is provided by Sader [26] to determine Γ_i under different conditions and actuator dimensions.

2.2.4 Comparison of Calibration Methods

The calibration methods described in the previous sections can be grouped into *static* and *dynamic* categories as illustrated in Fig. 2.10. The calibration technique that is most suitable for a particular device will depend on the cantilever shape, dimensions, available facilities and time. The dimensional models are very easy to implement, however, the accuracy of these models depends on the accuracy of the measurements of the device dimensions. Even with electron microscopy it is time consuming and difficult to measure accurately the cantilever thickness and uniformity. The Young's modulus of thin films is often unknown unless the device is large enough and fabricated from a well known material to assume bulk properties. Any thin metal films or surface layers that are deposited as part of the device design or to improve surface reflectivity will also contribute to the uncertainty in material properties. The dimensional models also impose restrictions on the beam geometry as they generally apply to rectangular cantilevers though some models have been extended to describe simple V-shaped beams. The usefulness of finite-element models of the cantilever are likewise dependent on the uncertainties in device dimensions and material properties. Uncertainties in beam thickness can be eliminated by determining the resonance frequency of the beam and incorporating it into the standard Euler-Benoulli beam equation, however, care must be taken as the measured resonance frequency will depend on whether the cantilever was tested in air or vacuum.

Static methods are mathematically simple but there are several practical difficulties associated with them. First of all these methods involve applying a known force to the cantilever tip. This can be done in several ways: (1) by securing a small mass to the beam tip, (2) by bringing the uncharacterised beam into contact with a calibrated pendulum or (3) a calibrated reference spring. In the first case a small sphere must be physically attached to the beam which must be done by hand and as a result is tedious and often destructive. The major sources of error in this

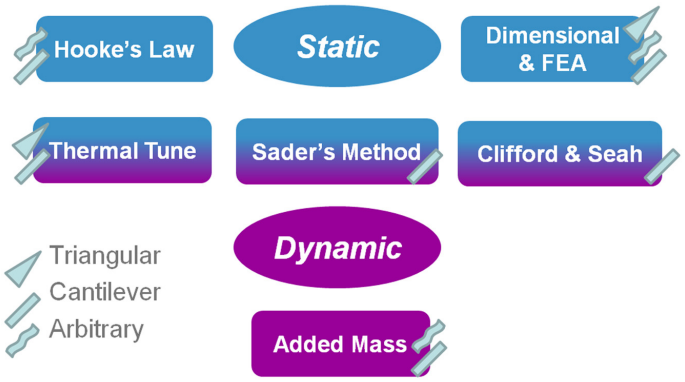

Fig. 2.10: A summary of the different calibration methods used in this investigation and their suitability for different spring geometries.

method are the measurements of the mass of the attached sphere and the position of the mass. The main difficulties associated with the calibrated pendumum is that the pendulum and cantilever need to be vertically mounted so that their relative displacements can be measured. The spring constant of the spring must also be estimated in advance so that the spring constant of the pendulum can be matched to that of the unknown spring. The pendulum can be replaced with a reference spring which means that measurements can often be made inside a standard AFM. There are even commercially available reference cantilevers manufactured by Veeco Probes in the range of $k = 0.157 - 10.4Nm^{-1}$ for this purpose. This is beneficial as the spring constant of the unknown spring should be in the range $0.3 - 3k_{ref}$ to minimise errors. The disadvantages of using a reference spring are the same as for the pendulum method. The main benefit of both of these methods is that they are non-destructive and can be applied to cantilevers of arbitrary shape. The Cleveland method or dynamic added mass technique suffers from many of the same errors as the static added mass method, that is, mass calibration and placement. Even so this method can be used to characterise cantilevers of an arbitrary shape without having prior knowledge of its spring constant or material properties.

The thermal tuning and Sader method both use the thermal noise spectrum of the

spring which restricts this technique to cantilevers with $k < 1Nm^{-1}$. Thermal tuning can be carried out automatically in some AFM machines as they incorporate the necessary hardware and software to calculate the rms tip deflection required in this method and automatically correct for errors arising from the optical lever measuring technique. The Sader method also requires some information extracted from the thermal noise spectrum of the beam such as the Q-factor, resonance frequency and the properties of the ambient air (or fluid). The hydrodynamic function can be intimidating to calculate, however, some online sources provide tabulated results or a means of calculating them. In both thermal tuning and the Sader method the resonance peak is fit with the simple harmonic oscillator model which helps to eliminate noise.

Without access to these automated functions the simpler unloaded frequency method can be used if the resonant frequency in a vacuum is known, however, the normalised effective mass M_{eff} will need to be calculated for a non-rectangular cantilever and the beam thickness must be determined. Cantilevers with deposited metal layers cannot be calibrated in this way.

2.2.5 Correction Factors and Sources of Error

In this project calibrated silicon springs were used to determine the tip force of a piezoelectric bimorph actuator. This approach is similar to the reference spring method of determining the spring constant of an unknown cantilever, however, in this case the tip force of the actuator is of interest. Measurements of the spring constant of the calibrated springs and of the deflection of the actuator-spring system need to be corrected to account for the geometry of the system and the limitations of the spring calibration methods used. Fig. 2.11 illustrates the source of these errors when using a reference spring with an off-end point of contact and measurement position (note that the geometries are exaggerated). Corrections must also be made when using the added mass method due to the off-end position of the mass and the measurement of the mass itself. In this section these correction factors will be discussed, though details and an example of these calculations will be left until a later section.

Non-contact measurements of deflection are normally of the optical lever type which reflect a laser beam off the sample onto a detector. Inaccuracies arise due to the finite spot size although this error is negligible for cantilevers longer than a few $100\mu m$, however, the position of the laser spot on the cantilever can lead to much larger inaccuracies in the measured deflection. It is a relatively simple matter to correct these errors if the off-end position of the laser spot and the tip gradient of the cantilever are known and assuming that the laser spot is small enough to assume a constant gradient. The gradient of the beam can be calculated using the beam equations or found via finite-element modelling, this information combined with the off-end distance can be used to find the real tip deflection.

The off-end corrections also depend on whether the laser is incident on the actuator or the reference spring. In the case of the cantilever reference springs their length varies from 8-21mm which is considerably longer than the bimorph actuators, the

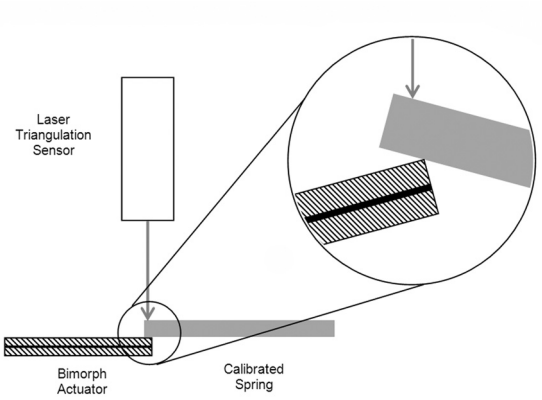

Fig. 2.11: The sources of error due to the off-end point of contact between the actuator and reference spring when making force measurements and the off-end measurement position (not to scale).

longest of which is 3.75mm. This considerable difference in length between the actuator and the reference springs means that for a given deflection their tip angles will differ as illustrated in Fig. 2.12. If the tip angle and the off-end distance are known then the correction factor that determines the real tip displacement (with zero off-end distance) and tip force can be found through geometry. The details of how these corrections are calculated will be discussed in a later section.

Static and dynamic methods that involve measuring the resonance frequency before and after adding a small mass to the end of the beam will incur errors due to the placement of the masses. When a mass is positioned near the cantilever tip the effect of that mass on the spring will diminish the further the mass is from the tip, off-axis placement of the masses can produce torsional effects though this error is generally small and can be neglected. The correction for an off-end mass on a rectangular cantilever is:

$$M_{eff} = M_{meas}\left(\frac{L - \Delta L}{L}\right)^3 \tag{2.48}$$

where M_{meas} is the measured mass of the added particle, M_{eff} is the effective mass of an equivalent particle perfectly mounted at the tip of the cantilever, L is the

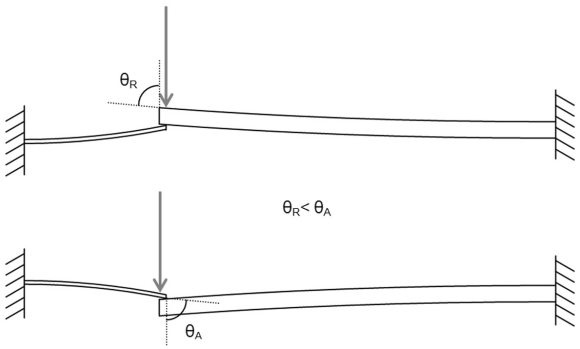

Fig. 2.12: The different measurement configurations when making tip force measurements of an actuator (left) with a reference spring (right).

length of the cantilever and ΔL is the off-end loading position of the mass. This expression is also a good approximation for V-shaped cantilevers as long as $L/\Delta L < 0.1$. To illustrate the importance of this effect consider an off-end loading distance of 5% of the cantilevers length which will reduce the effective mass of the particle by almost 15%. Even for cantilevers that are tens of mm long and spherical masses of a few hundred microns in diameter the reduction in M_{eff} will still be around 3%. A similar correction factor is also necessary when using a reference cantilever to measure the spring constant of an unknown spring (see Fig. 2.11). In this situation the known cantilever must contact the reference cantilever as close to the tip as possible, if the spring constant is measured with a tip offset of ΔL then the spring constant of the free tip is found using:

$$k_{tip} = k_{offset}\left(\frac{L-\Delta L}{L}\right)^3 \tag{2.49}$$

where k_{tip} is the spring constant experienced at the tip of the spring and k_{offset} is the spring constant measured at an off-end position. If the reference cantilever is not horizontal with respect to the sample the spring constant must be corrected for the tilt angle. AFM cantilevers are usually mounted at an angle of about 12°. If force measurements are made in this way the results are overestimated by a

factor of $cos^2\theta$ where θ is the tilt angle measured relative to the horizontal. This tilt angle also results in the spring constant of the reference cantilever being underestimated by the same factor so these two sources of error cancel out. For other methods the calculated spring constants must be modified in the following way to obtain the effective spring constant:

$$k_{eff} = \frac{k}{cos^2\theta} \tag{2.50}$$

A final source of error that applies to AFM probes is the protruding tip which extends from the cantilever and can produce a torque that contributes to the cantilever deflection angle and hence the measured deflection [27].

2.3 Micromachining Glass

Silicate or phosphate glasses are attractive materials for MEMS, microfluidic devices and lab-on-a-chip applications due to their excellent material properties. They are chemically resistant, optically transparent, have a low thermal conductivity and are bio-compatible. Glass is often used to seal and package MEMS devices as it can be readily bonded to silicon and has a similar thermal expansion coefficient. Unfortunately, the properties of glass that make it appropriate for many microsystems applications also make it difficult and relatively costly to micromachine. The micromachining techniques that are commonly used to selectively remove material can be grouped into three categories: mechanical, wet and dry. Mechanical techniques include conventional milling and sawing, ultrasonic milling, powder blasting and laser ablation. These methods usually have a higher material removal rate, however, brittle materials like glass are difficult to mechanically machine as brittle fracture can lead to surface damage. The effectiveness of laser micromachining is also limited by the brittleness and low thermal conductivity of glass which results in debris and poor surface quality, though these effects can be limited by using ultra-short pulses or small spot sizes. Powder blasting and ultrasonic machining erode the surface with abrasive powders and can produce complex shapes at high erosion rates though these methods are limited by the tool size and difficulties in masking. In comparison wet etching of glass is rather slow and isotropic which produces relatively low aspect-ratio features and makes it difficult to produce straight side walls. Wet etching can be improved by increasing the etch rate, increasing the resistance of the masking layers that define the surface features and decreasing the defects in the mask [28, 29, 30]. The upper limit of the etch depth of the glass depends on both the etch rate of the glass and the etch rate of the mask layer, once the mask layer has been completely etched away then the glass will be isotropically etched. If an inert mask material such as silicon or gold is used then the quality of the masking layers

is important as any defects in the mask will allow the etching solution to penetrate to the glass beneath. Typically, Cr-Au is used as a mask where the Cr acts as an adhesion layer for the Au, however, the stresses present in thick films (>100nm) can cause cracking and peeling and if the surface is hydrophilic the damaging effects of small defects and pinholes is increased. A multilayer mask consisting of several thin Au layers and additional photoresist layers has proven effective as the film stresses are reduced and the multiple layers minimise the damage caused by pinholes [31]. Etching solutions for glass are based on HF which reactes with the oxides in the glass to produce insoluble products. These products can reduce the etch rate and increase the surface roughness of the glass so one solution is to add HCL which reacts with the insoluble flourides to produce soluble products [32]. While wet etching occurs by means of surface chemical reactions, dry chemical etching occurs by means of both chemical reactions and physical sputtering. Dry etching in SF_6 [13], $SF_6 + Ar$ [35] and CH_4/CHF_3 plasma [33] have been reported though difficulties arise due to the nonvolatile reaction products that can coat the surface of the glass and reduce the etch rate.

Many of the problems of etching conventional glasses are bypassed by exploiting another family of glasses called photostructurable glass ceramics (PSGC). Glass ceramics are so called because they have a fine grained crystalline structure formed by heterogenous nucleation and crystal growth. In PSGCs the nucleation of the polycrystalline structure is controlled by the addition of a small amount ($< 5\%$) of nucleating agent. Once nucleating centres are formed by heating to the nucleating temperature (T_n) the glass can be crystallised by further heating to the crystallisation peak temperature (T_p). The additive serves to separate the two steps of nucleation and crystallisation by initiating the nucleation process. The nucleating agent must be carefully chosen as it can adversely affect (i.e increase) the melting temperature, decrease transparency and increase the thermal expansion coefficient of the glass [39].

From as far back as 1949 it has been known that the optical absorption spectrum of cerium containing glasses changes upon exposure to near-UV light radiation [36]. This has been interpreted as the photoionisation of Ce^{3+} to Ce^{4+} by optical absorption [37, 38]. This is beneficial as cerium is the most abundant rare earth metal and can be readily added to the glass melt in the form of CeO_2. The CeO_2 acts as a *photoinitiator* which can be used to reduce metal ions in the *nucleating agent* to form atoms which can be aggregated and willl then act as nucleating centres for crystallisation.

Some work has already been done to investigate the effect of the CeO_2 on the properties of lithium aluminium silicate ($LiO_2 - Al_2O_3 - SiO_2$) glasses [39, 41, 42]. Differential thermal analysis (DTA) has been used to determine the transition temperature (T_g) and the crystallisation peak temperature (T_p) of the glass. DTA involves heating or cooling a sample along with an inert reference material under identical conditions. As the samples are heated the temperature difference between them is measured by means of thermocouples. Changes in the differential temperature can be positive or negative indicating generation of heat or absorption of heat which can be used to determine the thermal properties or phase changes in the sample and find the optimum conditions for crystal growth. Using this technique it has been found that adding CeO_2 to LAS glasses reduces T_g and T_p, reduces the activation energy for crystal growth, encourages bulk (rather than surface) crystallisation and reduces the size of the crystal grains [39]. The optimum conditions for crystal nucleation and growth are highly dependent on the composition of the glass and any additives used [40].

It was not until the early 1990s that serious effort was given to the study of PSGCs as an engineering material for microsystems [43, 44, 45]. PSGCs can be used to build microstructures by selectively ionising the photosensitive additive present in the glass which leads to selective crystalllisation and as these regions are more soluble in HF they can be removed leaving the vitreous material intact.

SiO_2	$75 - 85wt.\%$
Li_2O	$7 - 11wt.\%$
K_2O	$3 - 6wt.\%$
Al_2O_3	$3 - 6wt.\%$
Na_2O	$1 - 2wt.\%$
ZnO	$0 - 2wt.\%$
Sb_2O_3	$0.2 - 0.4wt.\%$
Ag_2O	$0.05 - 0.15wt.\%$
CeO_2	$0.01 - 0.04wt.\%$

Table 2.1: The composition of Foturan^{TM} by weight from [44]

2.3.1 Foturan

A commercially available form of lithium-aluminium-silicate PSGC is manufactured by Schott under the tradename Foturan^{TM}. Foturan has been used to build a variety of microstructures as will be discussed in this section. The precise composition by weight of Foturan^{TM} is given in Table 2.1. When Foturan^{TM} is exposed to near UV radiation the *photoinitiator* CeO_2 and the *nucleating agent* Ag_2O work together to form an invisible image in the glass. When the glass is first in its molten form Ce^{3+} ions are formed by reduction:

$$2Ce^{4+} + Sb^{3+} \leftrightarrow 2Ce^{3+} + Sb^{5+} \tag{2.51}$$

When the solidified glass is exposed to UV radiation of wavelength 312 nm and energy density of $20J/cm^2$ the Ce^{3+} ions are further ionised to form the Ce^{4+} state:

$$Ce^{3+} + h\upsilon(312nm) \rightarrow Ce^{4+} + e^- \tag{2.52}$$

The photoelectron can be absorbed by the Ag^+ ions to form silver atoms

$$Ag^+ + e^- \rightarrow Ag \tag{2.53}$$

and the glass now contains an invisible image of the illumination pattern which is then fixed by thermal treatment. The glass is baked in a two step process to

Material Properties	***Glass***	***Glass Ceramic***
Density (g/cm^2)	2.37	2.41
Young's Modulus ($10^3 N/mm^2$)	78	88
Poisson's ratio	0.22	0.19
Knoop hardness (N/mm^2)	4600	5200
Thermal expansion α_{20-300} ($10^{-6}/K$)	8.53	8.64
Thermal conductivity at $20°C$ (cal/g$°C$)	1.35	2.73
Transformation temp. ($°C$)	465	590
Maximum safe processing temp. ($°C$)	400	700
Electrical conductivity at $25°C$ (Ohm cm)	8.1×10^{12}	5.6×10^{15}
Electrical conductivity at $200°C$ (Ohm cm)	1.3×10^{7}	4.3×10^{7}
Dielectric constant ϵ (1MHz)	6.5	5.7
Loss factor δ at $20°C$ (1MHz) ($\times10^{-4}$)	65	25
Refractive index (546.1nm) $25°C$	1.515	-
Acid resistance DIN 12116 (mg/dm^2)	0.4	0.9
Alkali resistance DIN/ISO 695 (mg/dm^2)	96	250

Table 2.2: Material properties of Foturan^{TM} from [46]

crystallise the glass around the Ag nucleating sites. Firstly, the glass is slowly heated to $500°C$ and maintained for one hour allowing the Ag atoms to agglomerate to form nanoclusters. The Ag clusters must be allowed sufficient time to reach a critical size before they can serve as nucleating centers for crystallisation. The temperature is then increased slowly to $600°C$ for one hour to allow crystals of lithium metasilicate (Li_2SiO_3) to form around the Ag nanoclusters. The crystallised glass has different physical properties from the vitreous glass as shown in Table 2.2.

The different physical properties of the crystallised glass such as density and thermal expansion can increase surface roughness and deform the glass after the crystallisation process. This can be minimised by exposing as small a surface area as possible, even when wishing to remove large areas of material it is better to remove a trench or channel *around* the required area rather than expose the whole area and etch it all away. The deformation that appears after the heat treatment step makes it necessary to planarise and polish the glass substrate before moving on to the etching. The main component of the glass is SiO_2 which is soluble in 10% HF solution. It is advisable to do the etching at room temperature in a

Hole Depth *(μm)*	***Minimum Hole Diameter*** *(μm)*	***Minimum Hole Separation*** *(μm)*
75-200 ±10	25 ±5	35 ±10
200-400 ±20	50 ±15	60 ±15
400-1000 ±30	120 ±20	140 ±20
1000-1500 ±40	180 ±30	210 ±30

Table 2.3: Dependence of minimum hole dimensions on the thickness of the Foturan plate reported by [44]

conventional etch bath though the etch rate can be increased considerably by using ultrasonic agitation. While ultrasonic agitation reduces the etch selectivity the reduced etch time goes some way to compensate for this. The mechanism for the dissolution of SiO_2 in HF is complex and not completely understood at a molecular level [29], however, the process can be described by the following simplified mechanism:

$$SiO_2 + 4HF \rightarrow SiF_4 + 2H_2O \qquad SiF_4 + 2HF \rightarrow H_2SiF_6 \tag{2.54}$$

The etch rate of crystallised Foturan^{TM} is around $10\mu m/min$ and the etch selectivity, that is the ratio of the etch rates of vitreous to crystallised material can be 20:1 or higher. When etching through a Foturan substrate the smallest possible hole size is limited by the thickness of the glass substrate, the etch selectivity and the size of the crystallites. Typial wall angles range from 1-4°. It is difficult to achieve high aspect ratio holes as the etch solution cannot reach the bottom of the hole though this can be improved by etching the Foturan from both sides and by using ultrasonic agitation. Double sided etching presents its own problems as the hole will have a constriction in the middle and difficulties arise in aligning and masking both sides of the substrate. Dietrich gives some useful tolerances for etching holes which are presented in Table 2.3 [44].

The surface roughness that results from the etching process can be improved by

post-etch annealing at $570°C$ for 5hrs [47, 48] or by coating in polysilazine (Si, N, C, H polymers) and cyclohexane (C_6H_{12}) before baking at $95°C$ for 4 hours to produce a SiO_2 coating that smoothes the etched surface of the glass [49]. These processes are particularly important for microoptical components where surface finish is important or microfluidic devices where the flow through a microchannel can be affected by the wall roughness.

The initial sensitising of Foturan can be done in a several ways. It is possible to use a mask aligner that is used for convenional photolitography processes though these tend to have a relatively low intensity UV source ($\sim mW/cm^2$) requiring exposure times of several hours [44]. The operator must also be aware that intervening optical components may absorb the near-UV wavelengths required to sensitise the Foturan^{TM}. A simpler and more intense UV source is a short arc mercury lamp normally used to cure photosensitve epoxies. These have a typical output of tens of mW/cm^2 and in a region of the UV spectrum that can be varied by changing the type of mercury bulb used. When using this kind of lamp to sensitise the Foturan^{TM} a simple shadow mask can be used which is placed between the glass and the UV source and does not necessarily require masking layers to be deposited directly on the glass substrate. This approach is suitable for producing submillimetre glass components, however, for smaller features ($< 100\mu m$) pulsed lasers are widely used [50, 51, 52, 53].

Pulsed laser sources make it is possible to precisely control the position of sensitised regions within a volume of glass to produce micro-optical components, sealed microfluidic chambers and even components that are completely free to move around inside cavities in the glass [54, 55, 56]. These true 3D structures are possible because the energy dose delivered by a pulsed laser source can be precisely controlled and the beam can be brought to critical focus inside the body of the glass away from the surface. In this way 3D structures can be made without the need to stack and bond components.

The wavelength of the pulsed laser sources varies (193, 248, 308, 351nm in [52]; 355, 266nm in [53, 57]; 775nm in [55, 54, 50, 51]). Most of these wavelengths are far from the 312nm required to photoionise Cr^{3+} so the sensitising mechanism must be different. This mechanism is not well understood, however, multiphoton absorption by defect states has been suggested and some evidence indicates that, in the case of femtosecond laser excitation, free carriers are generated by the scission of the Si-O bond rather than via $Ce^{3+} \rightarrow Ce^{4+}$ [58]. While femtosecond lasers have great potential for producing true 3D microstructures, relatively large ($> 100\mu m$) and simple components do not require a complex and expensive laser system and a conventional UV lamp and shadow mask are sufficient.

Chapter 3

Methodology

This chapter provides details of the microvalve fabrication and implementation of the spring calibration techniques described in the previous chapter. First we will consider the fabrication and the characterisation of the piezoelectric bimorph used in this investigation. This includes details of how the deflection and force characteristics of the actuators were investigated under static and dynamic conditions.

The fabrication and characterisation of the silicon reference springs will follow with details of the calibration methods used to determine the normal spring constant. The finite-element model used to support the calibration methods is also outlined with the ANSYS script supplied in an appendix.

Finally, the fabrication of the microvalve and the testing setup is described in detail. The photostructurable glass used for the valve body is characterised and the exposure conditions are investigated to determine the optimum conditions for the microvalve design and the exposure equipment used. A means of fabricating a variable transmission mask is also described which enables the etch rate of the photostructurable glass to be closely controlled.

3.1 Design and Fabricaton of the Actuator

The multilayer structure of the piezoelectric bimorph actuators was designed as part of the European Framework 6 Project "Q2M - Quality to Micro". The aim of the project was to develop high quality actuator composites that could be micromachined on the wafer scale and to develop transfer bonding techniques that could be used to transfer components from one substrate to another. Details of the piezoelectric multilayer structure and its fabrication has been reported elsewhere [59, 60]. The bimorph structure consists of a $10\mu m$ titanium shim which is adhesively bonded between two layers of $40\mu m$ PZT. The ceramic layers were thinned from 2mm×50mm diameter PZT ceramic wafers (TRS610HD, TRS Technologies Inc.) by means of a 8-inch wafer precision face grinder (Cranfield Precision Ltd). The fabrication steps for the multilayer structure are as follows:

1. The surface of the PZT wafers is prepared by machining to reduce surface roughness and deformity (grinding wheel diamond grit size=6-12μm, wheel spindle speed =99rpm, sample spindle speed=1600rpm, $1\mu m/s$ feed speed, water lubrication with $0.1\mu m$ filter).

2. The machined surface is cleaned in deionised water, IPA and acetone before being cleaned in an oxygen-argon plasma (100W, 100mbar, $O_2 - Ar$ flow of 50 SCCM, 10mins).

3. A Cr(10nm)/Au(100nm) electrode is then sputtered onto one of the machined surfaces. These metallised surfaces will contact the titanium shim during the adhesive bonding step.

4. The $10\mu m$ titanium shim is cleaned in IPA and acetone before being etched in a commercially available titanium etchant (Laporte) for 20s to improve surface wetting.

5. The metallised surfaces of the PZT wafers are bonded to the titanium shim

using a BCB adhesive (spun at 1000rpm, 30s) and bonded at $200°C$, 100kg/wafer for 8 hours using a wafer bonding machine (Suss Substrate Bonder SB6 VAC/SKM) to produce a bonding layer $< 4\mu m$ thick.

6. One side of the multilayer structure is thinned by grinding to the required thickness ($40\mu m$).

7. Cr (10nm)/Au (100nm) electrodes are then deposited on the machined surface after oxygen plasma cleaning (see step 2) and patterned using a conventional lift-off technique.

8. A glass carrier wafer is bonded to the surface with the patterned electrodes using a water soluble UV sensitive adhesive at room temperature (Delo Photobond 4464, spun at 2000rpm) and cured with a Hönle UVA Spot H-lamp for 40s.

9. The second PZT layer is then machined to the required thickness.

10. The PZT surface is then cleaned in an oxygen plasma (see step 2) before the second set of patterned electrodes are deposited with the usual lift-off procedure. The second set of electrodes must be carefully aligned with the first set of patterned electrodes through the glass carrier wafer and UV epoxy.

11. A thin layer of photoresist is deposited on the surface of the wafer to protect it during the next dicing step.

12. The actuator geometry is then defined by laser dicing with a 780nm Ti:Saphire femtosecond laser (Micreon Gmbh, Hannover, Germany) delivering 150fs pulses and $30\mu m$ spot size

13. The diced wafer is cleaned in hydroflouric acid (2.5% HF solution) and nitric acid to remove surface debris caused by the laser dicing and to clean the edges of the actuators thereby exposing the shim.

14. The wafer is cleaned in photoresist developer MF-319 (Shipley Microposit) and deionised water to remove all traces of surface photoresist.

15. The wafer is placed in a water bath at $40°C$ (>5hrs) to remove the UV sensitive epoxy and release the individual actuators.

16. The actuators are finally cleaned in deionised water, IPA and acetone.

17. The actuators are then series poled at $2v\mu m^{-1}$ at $120°C$ for 15 minutes.

The benefits of this type of "top down" fabrication approach is that bulk ceramic material can be used. The piezoelectric and material properties of bulk material are generally well known and are usually superior to piezoelectric materials prepared in the "bottom up" approach. The grinding and laser dicing steps also allow the thickness of the ceramic layers and plan view geometry of the actuators to be chosen to suit a variety of applications.

The primary bond between the ceramic layers and the titanium is formed at $200°C$. As the ceramic and the titanium shim have different thermal expansion coefficients the multilayer structure is prestressed, however, the symmetrical bimorph structure minimises unwanted deformation. The capabilites of the actuator can be estimated using the analytical expressions for tip deflection, blocking force and resonant frequency described in section 2.1.2. If the bimorph is to be integrated into a microvalve to open and close a $200\mu m$ diameter outlet then we can estimate the minimum force required to open the valve by considering the force due to the internal pressure of the microvalve acting against an area the size of the outlet orifice. Assuming the internal pressure of the microvalve is 1 atm (about 100kPa) above the ambient (also 1 atm) and the outlet orifice is $200\mu m$ in diameter then the force over the outlet area can be estimated by:
$1 \times 10^5 Pa \times \pi(100\mu m)^2 = 3mN$. Therefore we require at least 3mN tip force to open the outlet against 1 atm internal pressure. Using the bimorph equations formulated by Wang and Cross this tip force should be readily achievable with a

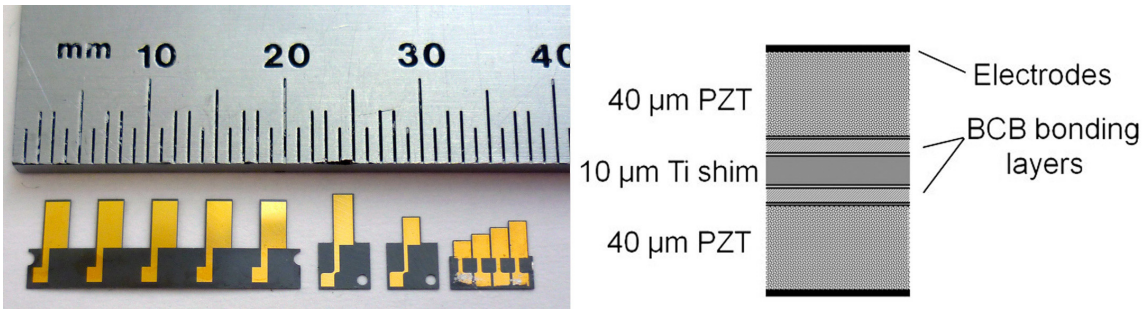

Fig. 3.1: The piezoelectric actuators used in this investigation (left) and their multilayer structure (right). The dimensions of the actuators are as follows (from left to right): $2 \times 3.75mm$ in an array of five devices, $1.6 \times 3.75mm$, $1.4 \times 2mm$ and $1.4 \times 1.2, 1.7, 2.2, 2.7mm$.

bimorph actuator with dimensions of the order of a few mm. With this in mind a range of bimorph cantilever devices were prepared with different lengths and widths ($1.4 \times 1.2mm, 1.7mm, 2.2mm, 2.7mm$; $1.4 \times 2mm$; $1.6 \times 3.75mm$; $2.0 \times 3.75mm$) though the total thickness of the bimorph structure was kept constant at $90\mu m$. These actuators are shown in Fig. 3.1. The deflection behaviour and tip force generated by these actuators was investigated under static and dynamic operating conditions as will be described in the following section.

3.2 Characterisation of Bimorph Actuators

Generally, the important performance parameters for piezoelectric bending actuators are the tip deflection, tip force and the required electrical operating conditions. The force characterisation of the actuators was accomplished by using a commercially available laser triangulation sensor (Keyence LKG32) to measure the displacement of a calibrated reference spring and the same displacement sensor was used to directly measure the actuator displacement under static and dynamic conditions.

The experimental arrangement used to make these measurements is shown in Fig. 3.2 and Fig. 3.3. The actuator and reference springs were mounted on a 3-axis stage each built from three micrometers with 25mm travel (Edwards Optics) and a USB microscope (Microcapture) was used to help with alignment. Electrical contact was made with the actuators by clamping them between glass plates that had Cr-Au electrodes sputtered onto their surface and wires secured to them with conducting epoxy. The glass plates were securely clamped to the actuators by larger acrylic plates that were bolted together. The whole clamp was itself mounted on a 3-axis stage ready for testing. Before making the tip force measurements the reference springs were bonded to microscope slides with Black Wax (Apiezon) which made them easier to handle.

Static deflection measurements were taken by positioning the laser spot of the displacement sensor a fixed distance ($200\mu m$) from the end of the actuator and by applying a DC potential between the shim and the outer (top and bottom) electrodes. The offset distance was to ensure that the laser spot of the sensor was not incident on the ceramic near the edge of the actuator which may be fractured during the laser dicing processing. As the bimorph was piezoelectric it exhibited creep so the deflection measurements were taken after a settle time of 2 minutes. Changes in the displacement can be read from the display on the sensor's control

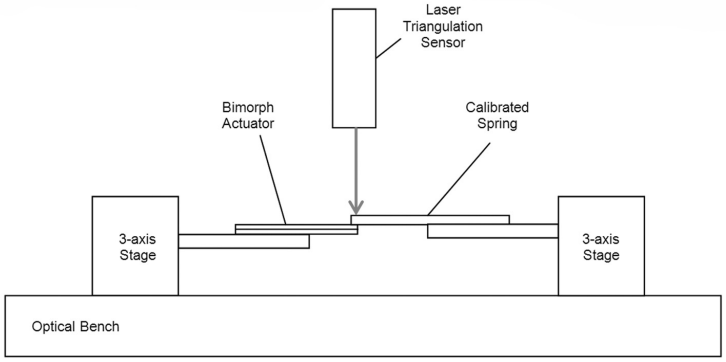

Fig. 3.2: A schematic of the measurement setup used to determine tip deflection and tip force.

unit or by using the supplied software which allows the sensor to be interfaced with a PC. The sensor head itself can store around 65,000 datapoints which can be collected at a user defined sampling rate and then transferred to the PC. This allows time dependent deflection measurements to be taken which was how the bimorph creep and relaxation were observed. The same arrangement was used for dynamic testing the only difference being that an AC amplifier (Chroma) was used to apply an AC and DC offset voltage of a certain magnitude and frequency ($< 1kHz$). When testing a free actuator it is able to oscillate in the positive and negative directions unhindered, however, when integrated into a microvalve the motion of the actuator is restricted in one direction due to the presence of the microvalve outlet as shown in Fig. 3.4. By applying a DC voltage to produce a positive deflection roughly equal to the amplitude of the deflection during AC operation the sinusoidal deflection of the beam is shifted so that the outlet is closed when Vac is at its negative extreme. It should be remembered that an applied voltage that generates an electric field in opposition to the internal polarisation of the actuator can depole the ceramic layers if the field is too large. For this reason the magnitude of Vac must be reduced accordingly so that Vac+Vdc does not exceed the poling potential. The shaded area in Fig. 3.4 represents the fraction of the actuation cycle when the outlet is open. In simple AC operation the outlet is

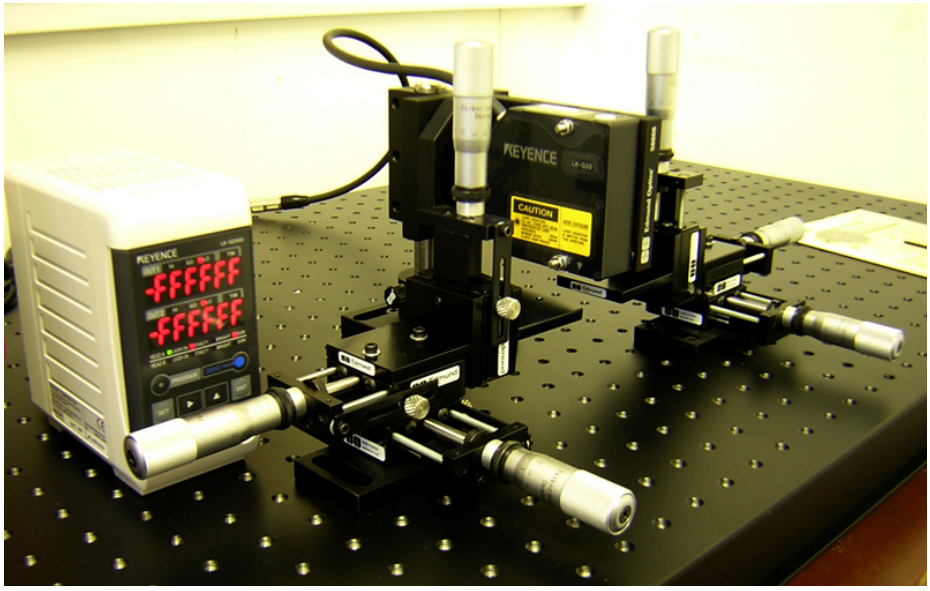

Fig. 3.3: The measurement setup used to determine tip deflection and force. The laser reference spring is mounted on the right x-y-z stage and the actuator is mounted on the left stage.

open for half a cycle, however, by using an offset voltage this can be increased.

The force generated at the tip of the actuators was found by mounting an actuator underneath the laser triangulation sensor and by bringing a reference spring into contact with it. If the tip force of an actuator in the positive direction (up) is being investigated the actuator is first centred under the displacement sensor with the laser spot a fixed distance from the actuator tip and on its central axis. The bimorph is then moved downwards a small distance (around $500\mu m$) to allow the reference spring to be positioned under the laser with a given off-end distance and at the optimum distance from the sensor. The deflection sensor had a limited range with a "sweet spot" where the deflection errors of the sensor are minimised and it is important that the reference spring is in this region before measurements are taken. The sensor is zeroed at this point and the actuator is slowly raised until contact is made with the reference spring and a deflection of around $1\mu m$ is registered. This ensures that the actuator and reference spring are in contact with

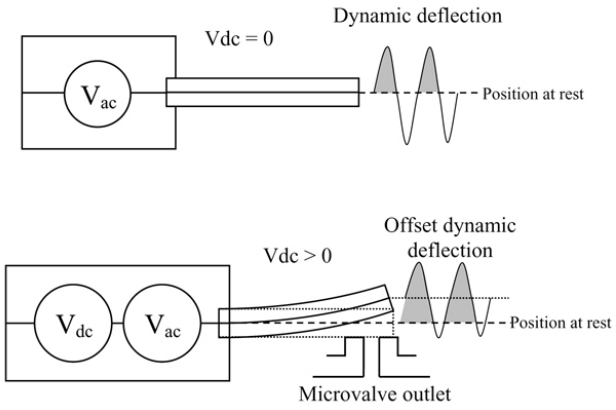

Fig. 3.4: Dynamic operation of the actuators in a microvalve requires both a DC and AC component. The actuator is restricted in the microvalve and a DC offset voltage can be combined with Vac to shift the tip deflection.

each other before a actuation voltage is applied. To measure the tip force in the negative direction (down) the reference spring is first positioned and aligned with the laser spot before being moved downards to allow the actuator to be positioned under the laser at the optimum position. The reference spring is then raised into contact with the actuator so that a deflection of $1\mu m$ is registered. The tip force measurements were made using three reference springs with different spring constants.

The resonance frequency of the reference springs and the actuators was determined using a laser-Doppler-vibrometer (Polytec) and an impedance analyser (HP 4192A LF) was used to determine the piezoelectric coupling coefficient.

3.3 Design and Fabrication of Reference Springs

Preliminary measurements of actuator tip force using a modified microbalance (KIT, Karlsruhe, Germany) indicated that around 10mN tip force was generated by a $1.6 \times 3.75mm$ bimorph, so the reference springs were designed to deflect $100\mu m$ for an applied force of 10mN to give sufficient deflection to reduce noise while maintaining a linear deflection response. The material for the reference springs was $\langle 111 \rangle$ silicon due to its well known isotropic properties in the $\langle 111 \rangle$ plane.

With these criteria in mind the dimensions of a set of rectangular springs were determined using equation 2.28. The width of the cantilever springs was set at 1mm and the thickness of the silicon was assumed to be around $300\mu m$ which would allow springs to be fabricated of the order of a few tens of millimeters long which would make them easier to handle and allow more to be fabricated on a standard 6-inch wafer. As there was a variety of actuators to test, a large array of springs was designed with a variety of spring constants so that multiple force measurements could be made. There were 24 rectangular springs divided up into four sets of six ranging from 10-21.5mm in length. The difference in length between adjacent springs was 0.5mm and they were separated by 2mm.

Triangular or V-shaped springs were also designed using equation 2.30. The dimensions used in both equation 2.28 and 2.30 are identified in Figure 3.5. The individual arms of the V-springs were separated by an angle of 30° and were 0.5mm in width (measured perpendicularly to the edge). The initial estimates of the spring constants of the cantilever and V-shaped springs as a function of the length are presented in Fig. 3.6.

The geometry of the springs was defined by first depositing and patterning an etch mask onto a $300\mu m$ silicon wafer and then by removing material using deep-reactive-ion etching (DRIE). This is a well established technique that etches

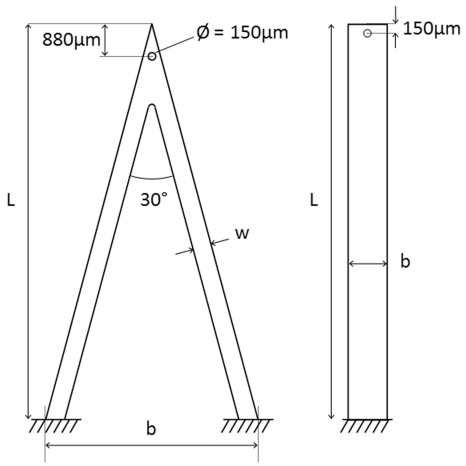

Fig. 3.5: The design of the calibrated silicon springs

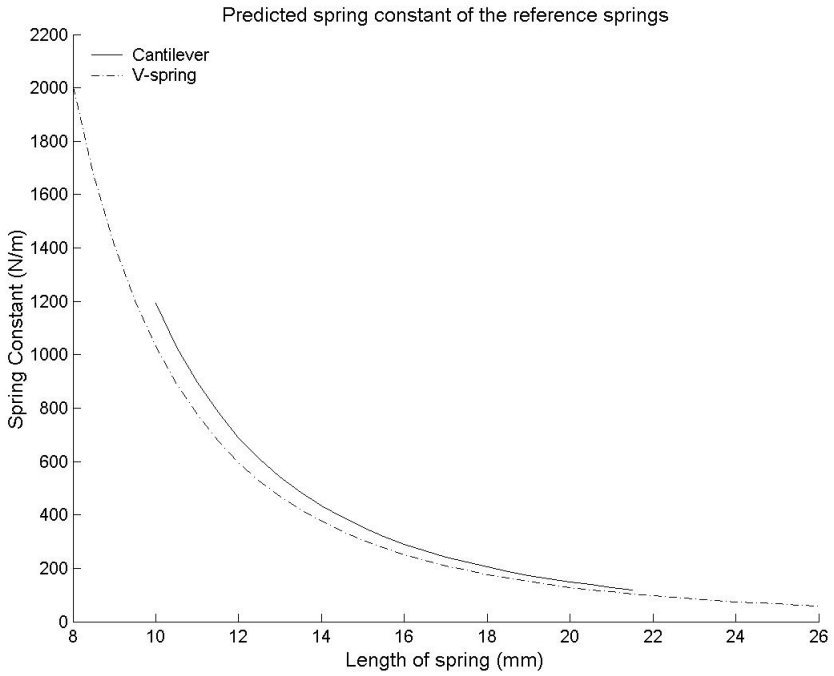

Fig. 3.6: Predicted spring constants of the silicon reference springs

	Etch	***Passivation***
Platen power	15W	
	SF_6 130sccm	C_4F_8 85sccm
O_2	13sccm	
Coil power	600W	600W
Platen	15W	0
Time	13s	8s
APC	65.8%	

Table 3.1: DRIE processing parameters

the silicon in a plasma of reactive gases that removes material via surface chemical reactions and physical sputtering. The etch recipe used is outlined in Table. 3.1 and is often called the Bosch process. The material removal rate varies depending on the surface area of material that is to be removed and the operating parameters, in this case the removal rate was around $1.25\mu m/min$. The masking layer was formed by depositing a $100nm$ aluminium layer directly onto the $300\mu m$ silicon wafer as the aluminium forms a nonvolatile flouride layer which is resistant to this dry etching recipe. Conventionally, a thick layer of photoresist is used as the mask, however, the photoresist is also etched in the plasma albeit at a slower rate than the silicon. Mask layers of photoresist that were thick enough to survive the etching step suffered from shrinkage and charring due to the high temperatures and long etch times. The aluminium layer was patterned by spinning a layer of photoresist onto the aluminium and patterning it with conventional photolithography. The wafer was then etched in a commercially available etchant (LaPorte Aluminium Etchant) to form a positive image of the reference springs. Before dry etching it was necessary to mount the silicon wafer onto a $500\mu m$ glass backing wafer with Black Wax (Apiezon) which would allow the silicon wafer to be etched completely through. After etching and releasing the springs, each spring set was secured to a microscope slide with Black Wax (Apiezon) so that it would be easier to handle and less likely to break.

Initial spring designs incorporated a stylus tip and were fabricated from $500\mu m$ silicon wafers. The wafers were thinned by an additional dry etch step to achieve

the desired beam thickness and which also defined the stylus tip. These design features were eventually discarded as the dry etching was not homogenous enough to ensure that the springs had a uniform thickness and the presence of a stylus introduces another correction factor into the force measurements. The stylus tip also required a double sided alignment step which introduced an uncertainty in the stylus position, this in turn would introduce more errors into the force measurements as an off-axis tip would produce torsional bending. These points are illustrated in Fig. 3.7 which shows a magnified view of a cantilever spring that has been thinned to around $100\mu m$ and has an off-axis stylus tip indicated by the arrow. The light grey channel was etched away to define the spring dimensions. The surface of the cantilever spring is rough and pitted due to the dry etching process. The unetched silicon visible at the top, bottom and left-hand-side of the image is only partially polished (this is the backside of the wafer) which likely contributed to the surface roughness.

For these reasons the final design was simplified as shown in Fig. 3.5 the only feature being a small hole near the tip of the springs which was used to position the small masses used in the their calibration. The simplified spring design required only three fabrication steps: (1) deposition of 100nm aluminium (sputtered at 300W), (2) photolithography and wet etching of the aluminium, (3) DRIE. Fig. 3.8 shows a finished wafer of cantilever reference springs which is still mounted on a glass backing wafer. The small holes in the base of the springs were for identification purposes. The small features adjacent to the cantilevers were silicon components that were intended to be used as masses for the static calibration of the springs, however, the masses were too small to be of use. The thickness of the springs was found by measuring the thickness of the silicon wafer before processing and optical measurements were made of the upper and lower surface of the beams to determine the beam width.

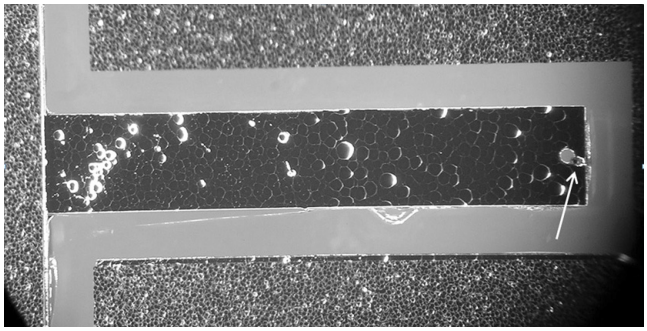

Fig. 3.7: The first spring design with a stylus tip (beam width =1mm).

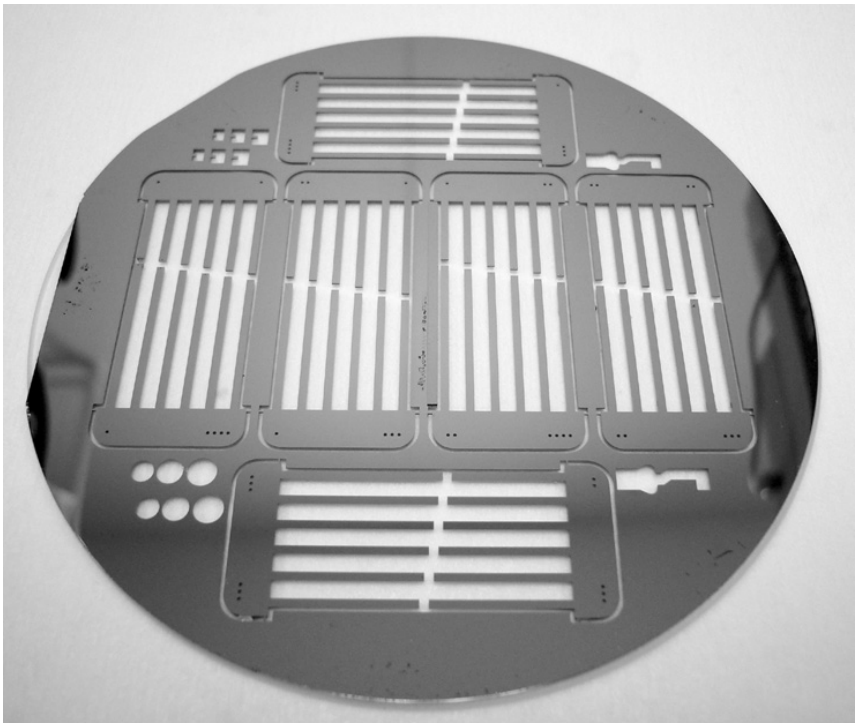

Fig. 3.8: A wafer of cantilever silicon springs.

3.3.1 Finite-Element Modelling of the Reference Springs

A simple finite-element model of the reference springs was constructed in ANSYS and used to predict the spring constant and resonance frequencies. The springs were modelled as simple rectangular cantilevers and V-shaped springs without tips and perfectly clamped at the base. The geometry was meshed using the *solid64* element type which is used for linear anisotropic 3D solids with 8-nodes. The cantilever was modelled using quadrilateral elements but tetrahedral elements were needed to fit the V-springs geometry. The anisotropic stiffnes matrix of $\langle 111 \rangle$ silicon was calculated from the more common $\langle 100 \rangle$ orientation and input into ANSYS. The *stiffness matrix* of $\langle 111 \rangle$ silicon can be found in Ref. [61] where the physical properties of the $\langle 111 \rangle$ orientation (upper case) are described in terms of the $\langle 100 \rangle$ (lower case) result:

$$C_{111} = \begin{pmatrix} C_{11} & C_{12} & C_{13} & 0 & C_{15} & 0 \\ \dots & C_{11} & C_{13} & 0 & -C_{15} & 0 \\ \dots & \dots & C_{33} & 0 & 0 & 0 \\ \dots & \dots & \dots & C_{44} & 0 & -C_{15} \\ \dots & \dots & \dots & \dots & C_{44} & 0 \\ \dots & \dots & \dots & \dots & \dots & C_{66} \end{pmatrix} \tag{3.1}$$

$$C_{11} = \frac{c_{11} + c_{12} + 2c_{44}}{2}; \quad C_{12} = \frac{c_{11} + 5c_{12} - 2c_{44}}{6} \tag{3.2}$$

$$C_{13} = \frac{c_{11} + 2c_{12} - 2c_{44}}{3}; \quad C_{15} = \frac{c_{11} - c_{12} + 2c_{44}}{3\sqrt{2}} \tag{3.3}$$

$$C_{33} = \frac{c_{11} + 2c_{12} + 4c_{44}}{3}; \quad C_{44} = \frac{c_{11} - c_{12} + c_{44}}{3} \tag{3.4}$$

$$C_{66} = \frac{c_{11} - c_{12} + 4c_{44}}{6} \tag{3.5}$$

where $c_{66} = 165.7GPa, c_{12} = 63.9GPa, c_{11} = 79.6GPa$. The spring thickness and plan view dimensions were measured optically and input into the FE model. To determine the spring constant all nodes at the base of the spring were clamped and a small force of 10mN was applied to a single node in the middle of the beam tip. The spring deflection was calculated using a *static* analysis and a *modal* analysis was used to determine the fundamental resonance frequencies. This data was compared to the spring constant and resonant frequencies of the fabricated springs found by static mass measurements and laser-Doppler-velocimetry. The ANSYS script used to model the cantilever is given in Appendix A.

3.4 Calibration of Reference Springs

As described in Section 2.2 there are a variety of techniques that can be used to determine the normal spring constant of a reference spring. The silicon springs used in this project were calibrated using the following methods (more details and definitions of variables can be found in section 2.2.2 and 2.2.3):

1. Static added mass - static deflection measurements using a small end mass.
2. Finite-element analysis - using ANSYS as described in section 3.3.1.
3. Dimensional models - the Euler-Bernoulli model using the second moment of inertia of a beam with both a rectangular and trapezoidal cross-section as found from the following equations:

   $k_z = \frac{3EI}{L^3} \qquad I_{rect} = \frac{bt^3}{12} \qquad I_{trapezoid} = \frac{t^3(a^2+4ab+b^2)}{36(a+b)}$
4. Clifford and Seah's modified dimensional model which incorporates the resonance frequency of the spring to eliminate the need to know the thickness of the beam:

   $k_z = a_2 w \frac{\left(L f_0 \sqrt{\rho}\right)^3}{\sqrt{E}} \quad a_2 = 59.3061.$
5. Dynamic added mass (or *Cleveland*) method - changes in the resonance frequency are measured as small masses are added to the spring tip:

   $k_z = \frac{(2\pi)^2 m_1}{1/f_1^2 - 1/f_0^2}$

Sader's hydrodynamic method and thermal tuning were not used as they are suited to reference springs with normal spring constants $< 1 N m^{-1}$.

The static method used in this investigation was simply to fabricate small masses which were hung from the end of the spring under investigation. The tabulated values of the masses are given in Table 3.9 and are shown in Fig. 3.9. They were formed from 700μm diameter solder wire which was wrapped around a cylindrical

Mass number	***Mean Mass*** ($\times 10^{-5} kg$)	***St. Dev.***($\times 10^{-7} kg$)
1	9.7	2.0
2	16.1	7.5
3	22.3	1.9
4	29.3	1.9
5	41.7	1.3
6	51.8	1.9
7	62.4	1.6
8	89.8	0.71

Table 3.2: The average value and standard deviation of the wire masses used in the static deflection measurements.

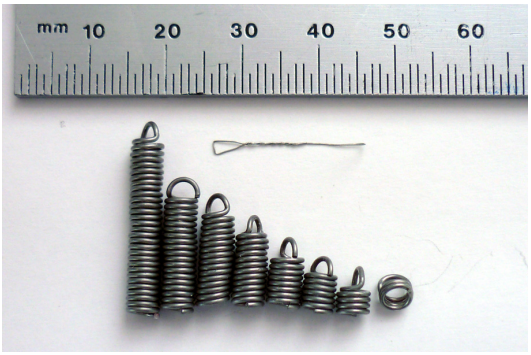

Fig. 3.9: A selection of bespoke masses used to determine the spring constant from static deflection measurements (numbered 1 to 8 from right to left).

former, the number of turns was increased to produce several weights of increasing mass. The masses were hung from the end of the cantilever spring by means of a wire loop (200μm diameter wire) that was suspended from the tip of the spring and which hung below the spring and suspended the masses on a hook.

Ideally the mass should be mounted at the very centre of the tip of the spring and the deflection of the spring would likewise be measured at its tip. In practice it is very difficult to position a suspended mass at the tip of the spring by hand, however, a USB microscope was used to position the mass as close to the tip of the spring as the thickness of the wire allowed (i.e. an off-end distance equal to the radius of the wire). The mass was allowed to settle for 2 minutes to allow vibrations to dissipate before measurements were taken. The triangulation

Microspheres - Physical Properties	
Density	2480-2520 kgm^{-3}
Softening Temperature	$650°C$
Coefficient of thermal expansion	$90 \times 10^{-7}/°C(30 - 300°C)$
Strength	29 $kgmm^{-2}$
Vickers Hardness	550 $kgmm^{-2}$
Refractive Index	1.51

Table 3.3: Material properties of the glass microspheres used as end masses (taken from [62].

displacement sensor could not be used to measure the displacement of the spring tip due to the wire used to suspend the masses, however, before the mass was suspended the laser spot of the sensor was position a fixed distance from the tip of the spring (typically $500\mu m$), this fixed distance was used to apply corrections to compensate for the off-end loading and measurement. The deflection of the springs was found for 3 different masses and these measurements were in turn repeated 3 times.

Clifford and Seah's modified dimensional model requires knowledge of the resonant frequency of the reference spring. This was determined by laser-Doppler vibrometry (LDV) which is a noncontact technique based on laser interferometry that is used to measure small displacements with great accuracy. The Polytec LDV system used in this investigation has a piezoelectric element which is used to shake the reference springs at a range of frequencies while the tip displacement of the spring is simultaneously measured. The LDV generates a spectrum of vibration amplitude with respect to driving frequency. At the resonant frequency of the spring the vibration amplitude of the spring tip is a maximum.

The dynamic added mass method solves equation 2.36 for k by adding several masses to the beam tip and finding the fundamental resonance frequency for each mass. A plot of m vs $1/(2\pi f)^3$ produces a straight line with gradient k. The masses were in the form of soda-lime glass microspheres (Polysciences Inc.) the physical properties of which are given in Table 3.3. The dimensions of the

microspheres were measured optically and the mass was calculated before attaching them to the spring. To reduce the uncertainty in the mass of the glass microspheres they were assumed to be ellipsoidal and the diameter was measured in two perpendicular directions. When using the added mass method it is important to accurately measure the mass of the microsphere and its off-end position on the reference spring. The $150\mu m$ diameter hole near the spring tip allowed the masses to be accurately and consistently positioned but there was still the problem of fixing them in position. One method is to first clean the silicon springs in 5% HF before uniformly applying a small amount of glycerol to the hole region near the spring tip. The spheres can then be positioned over the 150um hole and the meniscus of the glycerol secures the spheres in place. The springs are then baked at $750°C$ for 3 hours which vaporises the glycerol and softens the glass sphere sufficiently so that it bonds to the silicon [63]. Fig. 3.10 and Fig. 3.11 show how the glass mass bonds to the silicon spring. This bonding method is permanent as the glass even flows into the $150\mu m$ alignment hole preventing its easy removal (though it may be possible to do so by wet eching with HF). While it is possible to determine the spring constant by using a single added mass, more accurate results are obtained by using several masses. An alternative to this destructive method is to use a small amount of petroleum jelly which is viscous enough to secure the mass while being easy to remove in solvent. In this way several glass microspheres were used to determine the spring constant of the reference springs. In practical terms, this was done using the following procedure:

1. A number of glass microspheres were secured to a length of double sided adhesive tape which allowed them to be labelled and their dimensions to be optically measured.

2. A small amount of petroleum jelly was evenly and thinly spread onto a microscope slide.

3. Using fine pointed tweezers a single measured microsphere was then touched

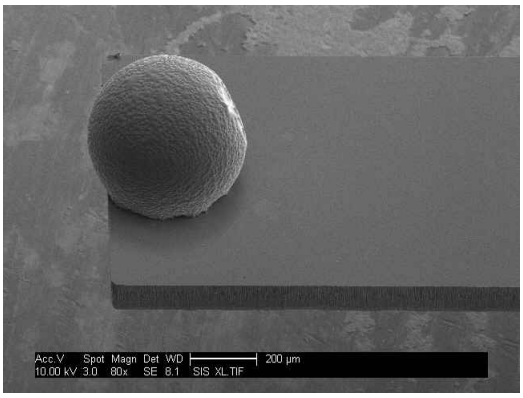

Fig. 3.10: SEM image of a glass microsphere bonded to a spring tip by sintering at $700°C$

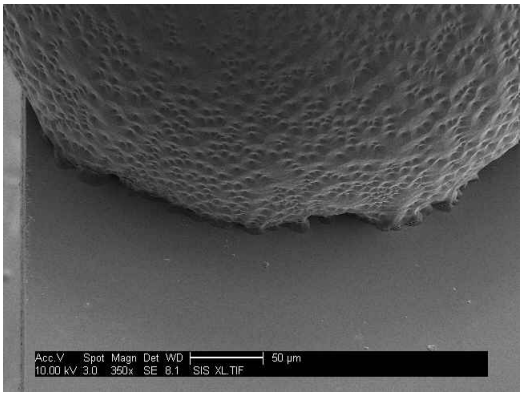

Fig. 3.11: A magnified SEM image of the interface between the glass microsphere and the silicon spring.

to the petroleum jelly before being deposited onto the reference spring tip.

4. The vibration amplitude spectrum of the spring and mass was found using LDV.

5. The glass mass can then be transferred back to its position on the double sided adhesive tape before cleaning the spring and adding another end mass and remeasuring the resonance frequency.

This procedure is considerably less time consuming than the sintering method and does not damage the reference springs. Only two grades of glass microsphere were

used (420-500μm and 250-300μm in diameter) so three of each size were attached in turn to each reference spring. The calculations and corrections used to determine the normal spring constant will be described in detail in a later section.

3.5 Design and Fabrication of a Microvalve

Piezoelectric microvalves commonly use a piezoelectric disc to restrict the flow through a channel, often by moving a flexible membrane [64]. Piezoelectric discs can generate large forces ($> 100N$), however the stroke length is usually rather small (a few tens of microns) which restricts the flow through the outlet. The advantage of using a piezoelectric bimorph is that the stroke length is increased considerably although the forces generated are smaller. The use of a bimorph type actuator presents some practical limitations to the fabrication and use of the microvalve, for example the processing temperature must not exceed around $150°C$ as this would damage the adhesive bond between the ceramic layers and the shim. This also limits the uses of the valve to controlling nonconducting media because the top, middle and bottom electrodes of the actuator are exposed inside the valve. A flexible membrance could be used to isolate the actuator from the medium passing through the valve, however, the small forces generated by the bimorph will likely not be enough to deform the membrane under useful differential pressures.

A simple design concept for the microvalve is presented in cross-section in Fig. 3.12. The bimorph actuator is clamped at its base between two components which will allow the actuator beam to deform under an applied voltage thereby directly controlling the flow through the outlet. This design uses the internal (positive) pressure of the valve to seal the outlet. The grey component in Fig. 3.12, which we will call the outlet component, forms a shallow cavity under the bimorph to prevent it from being completely clamped along its length. As the valve must encapsulate the actuator and form a seal around it the base of the actuator is seated in a shallow channel that forms a planar surface to which the top component can be bonded. There are several practical problems in implementing this relatively simple design, most of which result from using a photostructurable glass for the valve body. Before presenting the final design it is necessary to outline some properties of Foturan and the limitations that arise from the

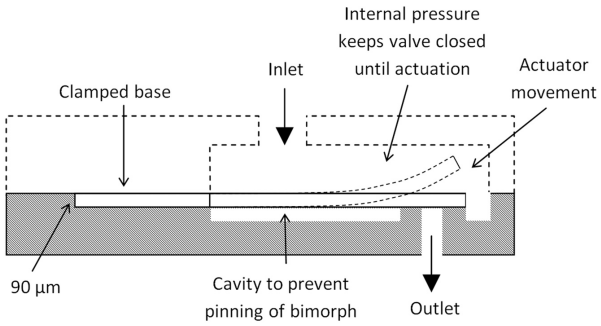

Fig. 3.12: The basic concept of the microvalve design.

processing steps used to fabricate components.

3.5.1 Processing and Characterisation of Foturan

The manufacturer of Foturan (Schott) recommends that components be made by etching through the full thickness of the glass plate. The reason for this is that the etch rate and uniformity are difficult to control, especially over relatively large areas. When removing large areas of material it is better to define the outline of the area to be removed rather than the full area. This is illustrated in Fig. 3.13 which shows two Foturan components that have been processed and crystallised with the aim of producing a cross shaped hole (the grey areas represent the crystallised Foturan). The design on the right is preferred for several reasons. Firstly, it will etch quicker as there is less material to remove and the etch rate will therefore be more uniform. Ultrasonic agitation can be used to increase the etch rate and assist in the removal of material at the bottom of the channel, however, the channel must not be too narrow as this will adversely affect the etch rate. It is important to minimise the etch time (without compromising etch selectivity) as the amorphous Foturan will also be removed, albeit at a much slower rate than the crystallised material. Overetching of the amorphous Foturan leads to rounded corners and significant differences ($> 10\mu m$) between the mask dimensions and the

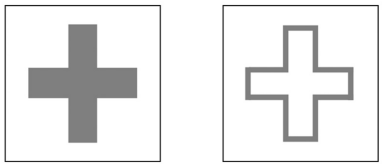

Fig. 3.13: Two approaches to etching a cross shaped hole in a Foturan plate. The approach on the right minimises the amount of material that is crystallised, the required etch time and the surface deformations.

component dimensions caused by lateral etching. If the ratio of the etch rate of vitreous material to crystallised material is known then the component shape and dimensions can be modified to compensate. Out of the two components in Fig. 3.13 the component on the right will also require less lapping and polishing as it will be less deformed than the component on the left. Deformations arise because of the different relative densities of the vitreous and crystallised Foturan. As the Foturan crystallises during the heat treatment the change in volume produces local surface deformations of a few tens of microns which must be removed to produce a flat component. By crystallising as small a volume of material as possible the surface deformities can be minimised. Fig. 3.14 shows some crystallised alignment marks that are $250\mu m$ in width, the deformation of the glass is clearly visible in the centre of the image where vitreous material is surrounded by crystallised regions. If the Foturan plate is $500\mu m$ thick the width of the outline of any hole or component (right) should be around $200\mu m$ wide, narrower crystallised channels will require longer etch times. The optimum dimensions of the outline of any feature will depend in the thickness of the Foturan substrate, however, the optimum width is not crucial as surface deformations cannot be completely eliminated because the heat treatment also generates pits and bubble-like features on the surface of uncrystallised regions which are usually a few microns in height/depth.

To investigate the surface properties of Foturan before and after etching a Dektak

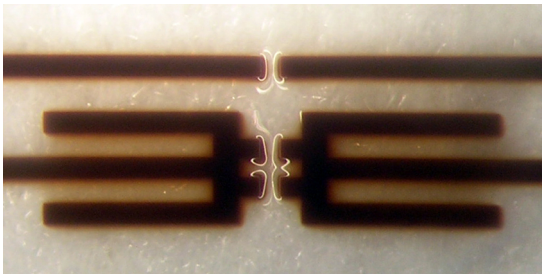

Fig. 3.14: The dark regions are crystallised Foturan in the form of alignment marks $500\mu m$ wide. The reflected light clearly shows the surface deformation that results from the volume difference between the vitreous and crystallised glass.

	Crystallised (nm)	*Amorphous* (nm)
Ra	187	31
Ry	-649	-109
Rp	712	148
Rt	1172	257

Table 3.4: The post-etch surface roughness of Foturan found using profilometry (9min etch in 10%HF to roughly half the plate thickness).

profilometer was used to measure the post-etch average roughness Ra, maximum valley depth Rv, maximum peak height Rp and peak to valley Rt of crystallised Foturan. The measurements were averaged over two cut-off lengths $80\mu m$ and $250\mu m$. Typical post-etch measurements of Foturan (9 minutes etch time) are given in Table 3.4. In all measured samples the post etch roughness is greater for the etched crystallised glass than the etched vitreous glass. The SEM images in Fig. 3.15 show the contrast between the two etched surfaces, it should be noted that the scale of the left and right images are $20\mu m$ and $200\mu m$ respectively. The surface of the crystallised Foturan (right) contains spikes and depressions that result from defects in the glass that alter the local etch rate. The bubbles and pits described earller may be the cause of the spikes and mesas on the etched surface but they have so far not been observed in crystallised regions. The left hand image shows that the vitreous glass is still pitted by the etching process which attacks scratches and imperfections in the surface. This shows the need to thoroughly

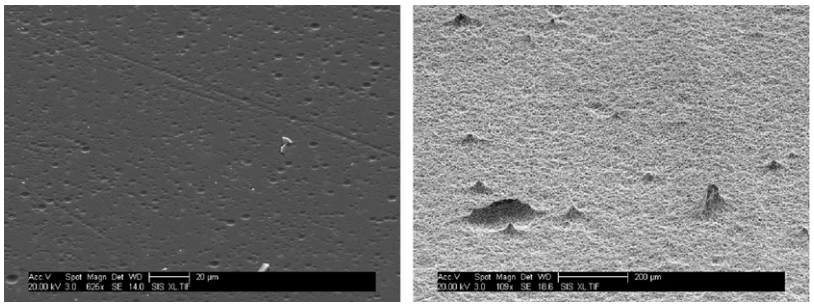

Fig. 3.15: SEM images of uncrystallised (left) and crystallised (right) Foturan after etching in HF. Note the different scales: left - $20\mu m$, right - $200\mu m$.

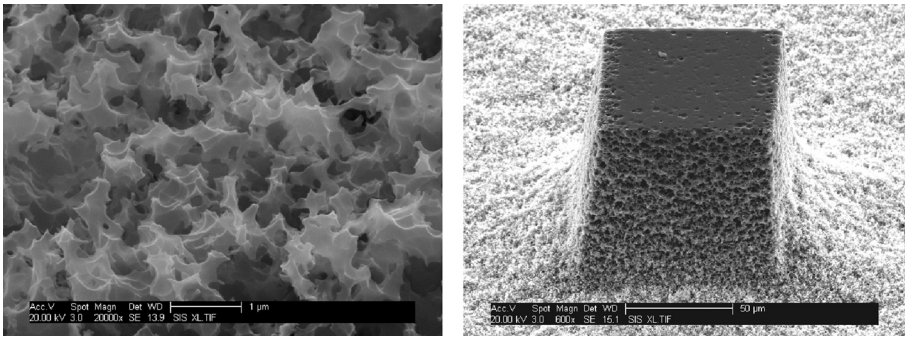

Fig. 3.16: A 20,000x magnification of crystallised and etched Foturan (left, scale=$1\mu m$) and a $100\mu m$ square (right, scale=$50\mu m$).

polish the Foturan component after etching if a low surface roughness is required.

A closer examination of the surface of crystallised Foturan that has been partially etched shows how the HF preferentially attacks the crystal boundaries producing a dendritic and almost porous surface (Fig. 3.16). Surface profilometry was seen to leave visible lines on the surface of the etched Foturan which is evidently caused by the passage of the Dektak stylus which damages the delicate structure of the etched glass. Clearly, partially etched Foturan is not a suitable surface on which to mount components or to deposit metal layers.

The vitreous and crystallised Foturan etch at different rates because the high density of crystallites increases the surface area that the HF can attack. It is

reasonable to assume that the exposure dose will affect the etch rate as the number of nucleating sites formed depends on the incident photon flux. The smaller the number of nucleating sites the smaller the number of crystallites that will form during the heat treatment. The crystallised glass will consist of fewer and perhaps larger crystallites that either share grain boundaries or are surrounded by vitreous regions. The density of grain boundaries will therefore be smaller which will reduce the etch rate. The manufacturer estimated that a 15 minute exposure to a UV lamp would saturate the glass and achieve optimum nucleation so this was used as a starting point for experimentation. Fig. 3.17 presents the dependence of the etch rate and etch selectivity on the exposure time. The etch selectivity is defined as the ratio of the etch rate of the crystallised Foturan (Ec) to the etch rate of the amorphous Foturan (Ea). The plot of the etch rate of the crystallised material, Ec, as a function of the exposure time (left) suggests that the etch rate saturates around 18 minutes of exposure time. The etch selectivity indicates a linear dependence on exposure dose, however, we would expect it also to saturate around the same exposure time as Ec when the optimum crystallisation of the Foturan is achieved. The lateral etch rate was found by measuring the dimensions of surface features ($100, 250, 500, 1000\mu m$ squares of amorphous material surrounded by crystallised material) and comparing them to the mask dimensions. The dimensions shown in Fig. 3.18 are approximate as they were found from SEM images of the sample and it was not possible to completely compensate for the observation angle (70°). The wall angle was found to be about 7°. Fig. 3.18 indicates a strong link between feature size and lateral etch rate.

The optimum exposure time can be estimated by considering the emission spectrum of the UV source. The lamp used to sensitise the Foturan was a Hönle UVASPOT 400/T (Fig.3.19) which has a power output of 450W and is generally used as a high output UV source for industrial and research applications (e.g. curing of UV activated polyester resins, UV sensitive adhesives and irradiation of chemical, biological or pharmaceutical agents). Due to the dangerous levels of UV

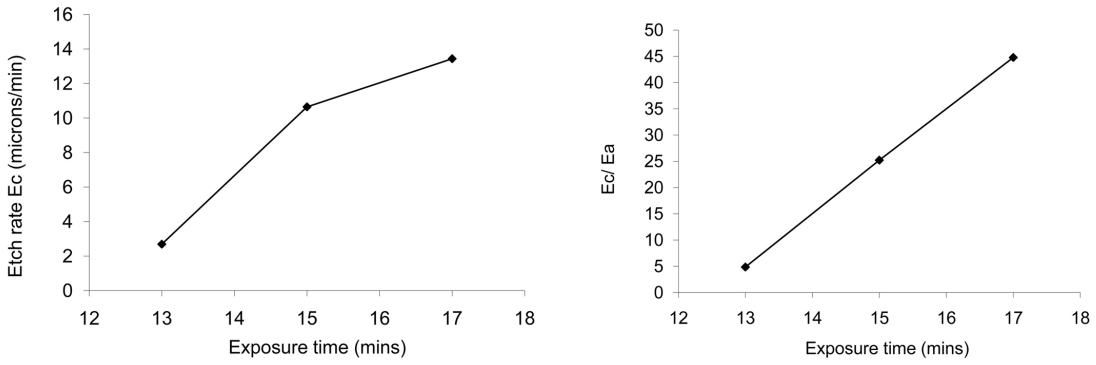

Fig. 3.17: Foturan etch rate and selectivity. Ea and Ec are the etch rates of amorphous and crystallised material.

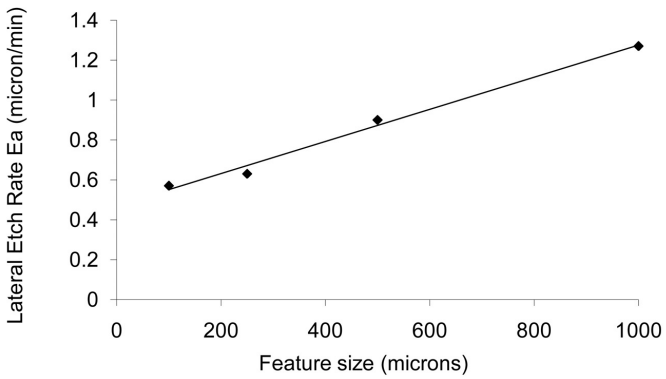

Fig. 3.18: The lateral etch rate of amorphous Foturan.

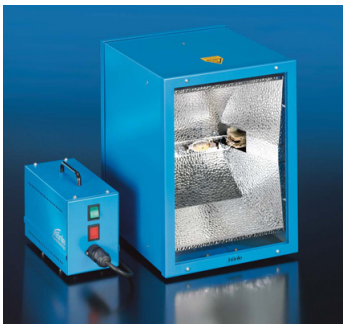

Fig. 3.19: The Hönle UVASPOT 400/T lamp used to sensitise the Foturan.

produced by the lamp it was mounted face down on a metal box which had two shutters to prevent accidental exposure to the radiation. One shutter slid between the lamp and the sample chamber and the second opened the front of the sample chamber. The shutters were arranged in such a way that a sample could not be loaded while the chamber was being illuminated. This arrangement made it vital to position the sample in the middle of the chamber otherwise the shutters would block some of the radiation.

The emission spectrum of the lamp is shown in Fig. 3.20 which shows a modest peak around 312nm. To obtain a quantitative value of the power emitted around 312nm a UV sensor (Karl Süss UV intensity meter model 1000) was used to measure the output of the lamp at 405nm. Fig. 3.21 shows the time dependent output of the lamp at 405nm which illustrates the need to allow the lamp to warm up so that the output stabilises. The normalised intensity spectrum of the lamp shows that its output at 312nm is about 70% of its output at 405nm. After a 10minute settling time the output of the lamp at 405nm was $20.1 mW cm^{-2}$ and therefore its output at 312nm was about $14 mW cm^{-2}$. The manufacturer states that Foturan needs $20 J cm^{-2}$ which would require exposure for 23min 48sec to a source whose output at 312nm is $14 mW cm^{-2}$. Another factor that needs to be taken into account is the optical absorption of the shadow mask. To pattern the Foturan it is exposed through a mask which is made from patterned metal layers

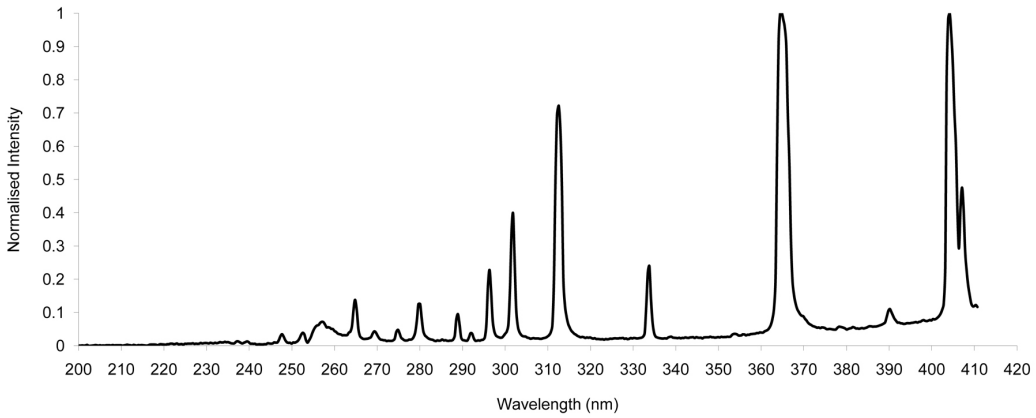

Fig. 3.20: The emission spectra of the Hönle UVASPOT H-lamp. At 405nm, Intensity=20.1 $mWcm^2$

on a borosilicate glass substrate. The glass substrate reduces the intensity at 405nm by about 6%, however, this does not necessarily mean that the intensity at 312nm is also reduced by 6% as glass is generally more absorbing at shorter wavelengths. The optical transmission spectrum of the glass substrate was found using a Perkin Elmer Lambda 7 spectrophotometer and is presented in Fig. 3.22. The optical absorption is uniform for wavelengths from 350nm to 600nm, however, for shorter wavelengths the absorption quickly increases until the intensity is completely attenuated around 270nm. At 312nm the glass transmits about 60% of the intensity at 405nm ($8.4mWcm^{-2}$) therefore we would expect the exposure time stated earlier to underestimate the optimum conditions by about 40%. This would suggest that the optimum exposure time is in fact 39min 41s.

After some experimentation it was found that the optimum exposure time of the Foturan was considerably less than 39min 41s. During this project two batches of Foturan were ordered, the optimum exposure time for the first batch was around 19min and for the second batch it was about 28min. Electron dispersive X-ray spectroscopy (EDS or EDX) data was collected for these two batches of Foturan to see if there were significant differences in their chemical composition. EDX is an

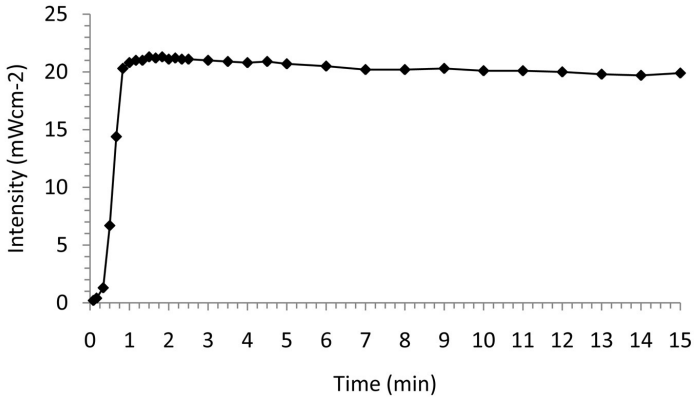

Fig. 3.21: The change in output intensity of the H-lamp as a function of exposure time (405nm).

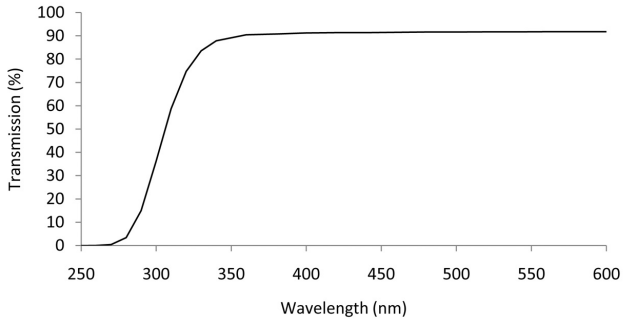

Fig. 3.22: Optical transmission spectrum of borosilicate glass.

analytical technique that determines the elemental composition of a sample by analysing the X-rays emitted by the sample in response to a beam of energetic particles or electromagnetic radiation. A typical EDX spectrum of Foturan (first batch) is presented in Fig. 3.23 and the quantitative composition by weight is given in Fig. 3.24. The variation in the most abundant elements (Si, O) is 1-2% whereas the variation in the less abundant elements is 0.1%. Surprisingly, the fraction of the nucleating agent Ag is only 0.1-0.2% and the quantity of UV sensitive Ce is not even detectable using this method. This suggests that the optimum UV exposure dose is highly dependent on the composition of the Foturan if such small variations in composition can produce changes in the optimum exposure time of almost 50%. It is likely, however, that the calculation of the optimum exposure time is in error as it assumed that the Foturan is only sensitive to 312nm radiation. In a previous section (2.3) it was pointed out that pulsed lasers are often used to directly pattern Foturan. The wavelengths of these lasers vary considerably which suggests that there is more than one mechanism which sensitises Foturan and these mechanisms were not taken into account when calculating the optimum exposure time.

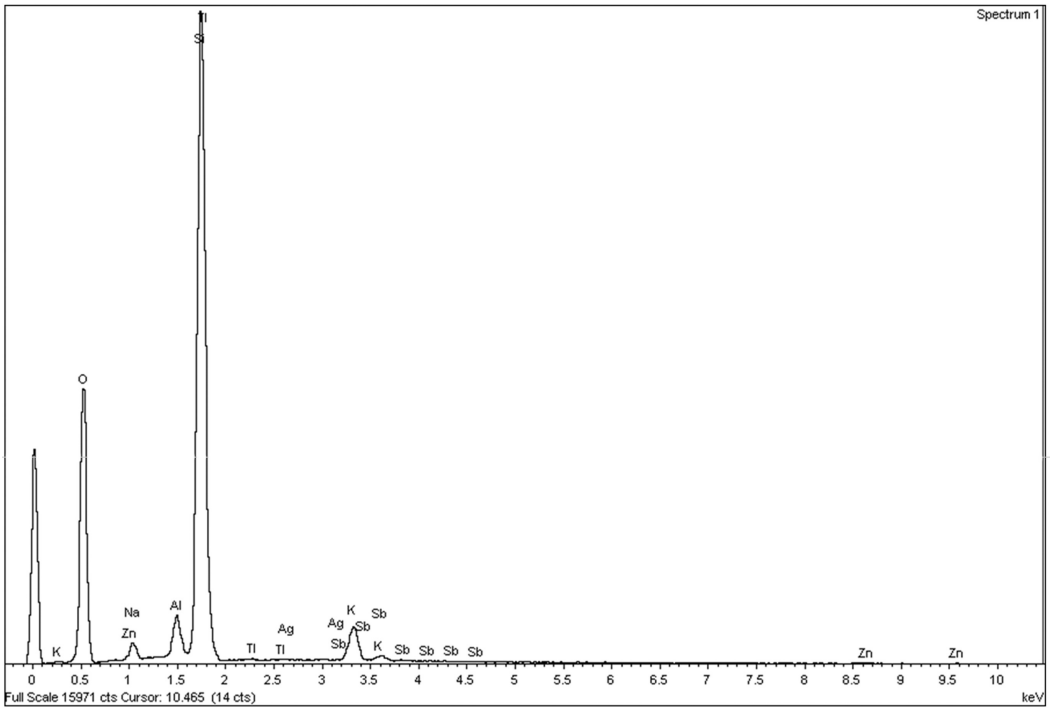

Fig. 3.23: EDX spectrum of the first batch of Foturan.

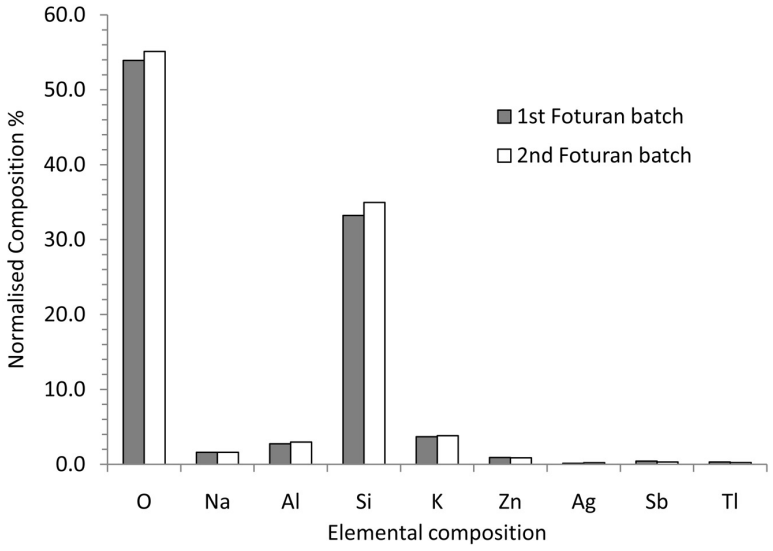

Fig. 3.24: Comparison of the EDX spectrum of two different batches of Foturan.

3.5.2 The Foturan Microvalve

The design criteria for the Foturan microvalve were (1) the valve must generate synthetic jets around $200\mu m$ in diameter with a velocity of $200ms^{-1}$ and (2) the valve will be actuated with a piezoelectric bimorph. The outlet dimensions and exit velocity were selected for the application of *active flow control* [65]. Active flow control seeks to control the flow of air (or water) over an aerodynamic surface by influencing the flow near the surface. There is a large amount of literature on the topic, however, the principles and current state of research in this area are both outside the scope of this report.

The geometry of the bimorph actuator presents some limitations on the design of the microvalve in a number of ways. The microvalve must allow access to the electrodes on the top and bottom surface of the actuator and via the metal shim. The tip of the bimorph must open and close the valve without the need for sealing membranes or tip mounted objects that may damage the actuator or reduce the tip deflection/force generated. Finally, we need to keep in mind the processing limitations of Foturan described in the previous section.

The simplest way to achieve these goals would be to modify the simple design presented in Fig. 3.12 (section 3.5) to satisfy the above criteria. A modified microvalve design is presented in Fig. 3.25. In practice there are several problems with this design, most of which result from the use of Foturan for the valve body and the need to accomodate the actuator between components while maintaining a flat profile. As shown in Fig. 3.25 the valve body is now constructed out of four $500\mu m$ thick Foturan components that clamp the bimorph actuator to the outlet aperture. Electrical connections are made from the edge of the valve and contact is made with the surface electrodes of the actuator by means of Cr/Au electrodes that are sputtered directly onto the Foturan components that clamp the top and bottom surfaces of the actuator. Electrical contact is made with the shim by

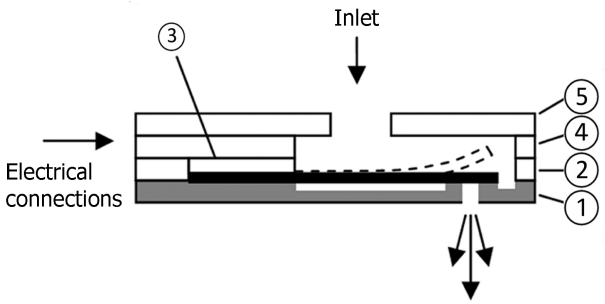

Fig. 3.25: The cross-section of a microvalve composed of several stacked Foturan components.

placing a small amount of conducting silver paint on the edge of the actuator which is then used to make an electrical connection to an external electrode. The positive internal air pressure of the valve ensures that the outlet is sealed by the bimorph actuator until a voltage signal is applied to deflect the actuator away from the outlet. The microvalve dimensions are essentially determined by the length of the bimorph actuator which is required to generate sufficient tip force and tip displacement to open the outlet against the internal pressure. The five components of the microvalve body are as follows: (1) the first component contains the aperture that is opened and closed by the actuator, an electrode is sputtered onto its surface to contact the bottom electrode of the actuator and there is a shallow cavity under the bimorph to equalize the pressure around the actuator away from the outlet; (2) this component frames the actuator and aligns it with the outlet and electrodes; (3) this is fabricated as part of 2 but after etching and release it is further lapped and polished to reduce its thickness by an amount equal to the thickness of the actuator so that it can sit on the actuator base to clamp it; (4) this layer planarises, provides structural support and allows access to the top electrode of the actuator; (5) this final component seals the valve and forms the inlet for the compressed air supply, electrodes are also sputtered onto its surface to contact the top electrode.

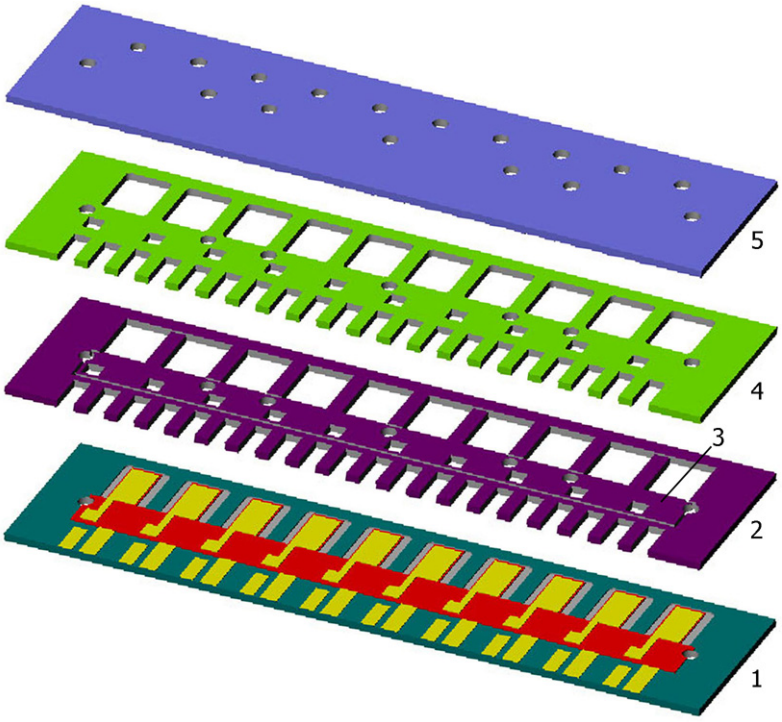

Fig. 3.26: A CAD model of the microvalve components.

This simple design can be extended to an array of microvalves that can be used for active flow control. Fig. 3.26 shows a design for an array of 10 microvalves (2mm x 11mm x 46mm) each with their own electrical connections. This microvalve array requires an array of 10 bimorph actuators, however, the actuators are fabricated from 2.5-inch PZT wafers as shown in Fig. 3.27 which limits the number of actuators in a single array. To address this issue the wafer was diced to give arrays of 5, 3, 2 and 1 actuators which can be arranged into an array of 10. The purpose of the circular holes that lie along the centre of the long axis of the valve components in Fig. 3.26 is to assist with the alignment the components with the actuators. As shown in Fig. 3.27 the actuator arrays are terminated with semicircular features that align with each other and with the holes in the Foturan components. The components are aligned by inserting a 1mm diameter pin into the holes during assembly. The holes are also used to make electrical connection with the shim of the actuator by using conducting silver paint to contact the edge

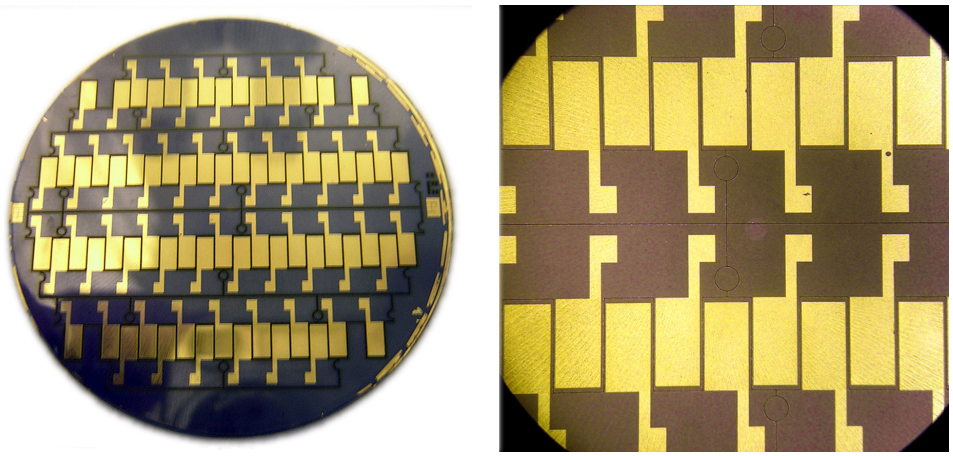

Fig. 3.27: A 2.5-inch wafer of the multilayer strcture used to make the bimorph actuators.

of the semicircular feature and draw a conducting path to the external surface of the valve body or an external electrode.

An important feature of the valve design is the way that the electrical connections are made with the bimorph actuator. The bimorph itself is only $90\mu m$ thick and each ceramic layer is only $40\mu m$ so the integrity of the ceramic layers is a major concern as cracks in either or both of these layers may cause shorting between the electrodes and the central shim and turn the bimorph into a unimorph or worse. External connections cannot be made directly with the actuator as any connecting pins or plugs that are applied perpendicularly to the actuators surface could easily cause damage. The solution was to deposit metal layers directly onto the Foturan components 5 and 1 in Fig. 3.25, which are used to connect to the top and bottom actuator electrodes respectively. The electrical connections are shown in more detail in Fig. 3.28. The bottom electrode of the actuator makes surface contact with the electrode on component 1. The top actuator electrode is brought into contact with the electrode on component 5 by means of a small spring that is clamped between the actuator and component 5. Component 3 and 4 contain small windows that align to allow the spring to be placed between the components.

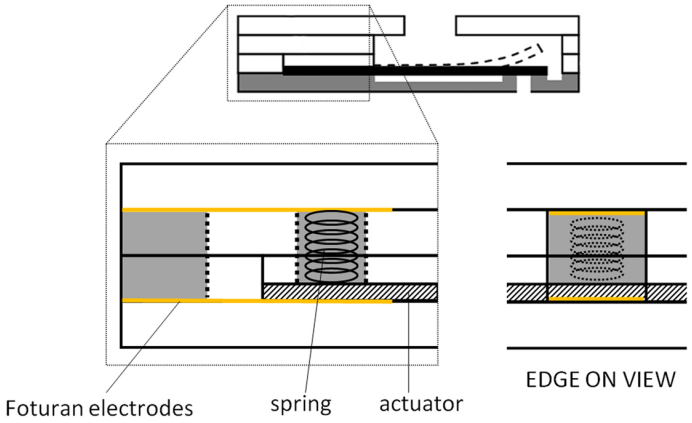

Fig. 3.28: Detail of how electrical connections are made to the actuator in the microvalve.

The spring coil was less than 1mm in diameter and was formed by simply coiling a strand of wire (200μm in diameter) around a cylindrical former. The spring was sufficiently elastic to make a good surface contact with the electrode without damaging the ceramic. To ensure that a good electrical connection was made a small amount of conducting silver paint was applied to the surface electrodes of the actuator and the point of contact on the Foturan electrodes.

There are two approaches to deposit metal electrodes onto Foturan. The first method is to use a convenional lift-off procedure and the second is to use a shadow mask. In the lift-off process photoresist is spun onto the Foturan and patterned before depositing the metal electrodes. The Foturan must be thoroughly cleaned and prepared with an adhesion promoter (hexamethyldisalizane, HMDS) to improve the adhesion of the photoresist to the glass which has a tendency to peel around the edges of features during development. To obtain a uniform layer of photoresist it must be spun onto a flat substrate which means that this step must be done before the Foturan is etched. If the substrate is not circular then the photoresist tends to gather in the corners forming regions of thicker photoresist which will require long exposure and development times to the detriment of more central features. If using this method it is important to polish the Foturan to

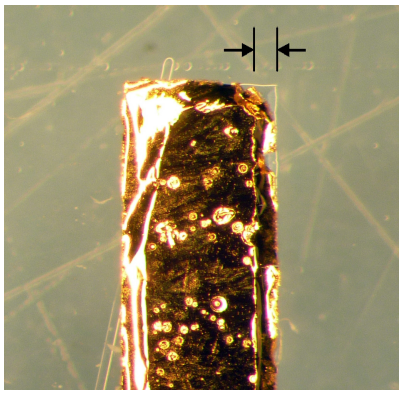

Fig. 3.29: Peeling of an electrode on the surface of a Foturan component caused by wet etching (electrode width = 1mm).

present a flat surface with low surface roughness onto which the electrodes can be deposited. Once the electrodes have been deposited using the lift-off technique the component is then etched. Unfortunately HF tends to attack the interface between the glass and the metal electrodes causing peeling along the edges of the electrodes. The result of this is shown in Fig. 3.29 which shows a 1mm diameter electrode strip after etching in 10% HF to remove the crystalised Foturan. The etching solution has caused the electrode to peel away from the glass around its perimeter and pinholes in the metal layers have allowed the etching solution to cause blisters away from the edge. The original outline of the electrode is visible at the top right of the electrode where the metal layers acted as an etch mask. The masking effect of the metal layers produces a step of around $10\mu m$ between the surface of the electrode and the surrounding glass. This effect could make it difficult to seal the valve once the components are stacked together and adhesively bonded. For this reason the area covered by the electrode metal was redesigned as shown in Fig. 3.30 to cover as large an area as possible and thereby reduce the area of the etched surface.

The alternative approach of sputtering the metal electrodes through a shadow mask was also tried using the same mask design as used above. When using a

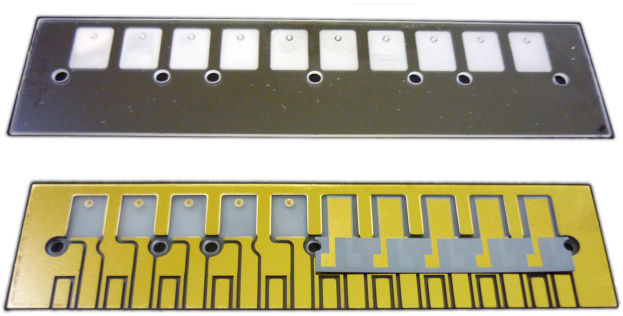

Fig. 3.30: The outlet component before and after electrode deposition.

shadow mask the electrode layers are sputtered directly onto the etched Foturan components which eliminates the problem of electrode peeling. There will be some surface damage caused by the etching, however, this will be negligible if they are well polished and planarised before etching and the etch time is minimised.

The shadow mask was made using the same process used to fabricate the reference springs, that is by first depositing a 100nm layer of aluminium onto a normal $500\mu m$ silicon wafer that had been thoroughly cleaned prior to deposition. Photolithography and wet etching were used to pattern the aluminium to form a negative image of the electrode pattern. The aluminium layer served as an effective etch mask for deep reactive ion etching (DRIE) of the silicon. The shadow masks produced in this way are shown in Fig. 3.31 and were used to deposit the electrodes on the Foturan components after they had been wet etched. The etch rate during DRIE was not constant over the full area of the wafer and the features in the upper region of the top mask in Fig. 3.31 suffered noticably from lateral etching. When using the shadow mask the aluminium surface was placed into contact with the Foturan component which minimised the effect of the lateral etching of the silicon. If a shadow mask is used after etching the Foturan the surface of the component will be flat unlike the first approach where the electrodes acted as a mask during HF etching. This means that the area of the bottom electrode layer does not have to be enlarged and can be simplified (Fig. 3.26

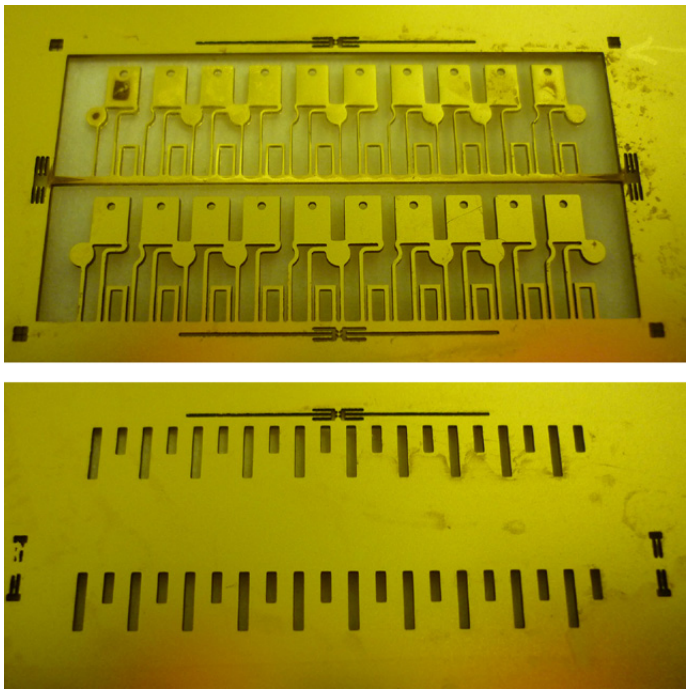

Fig. 3.31: The silicon shadow mask used when depositing the surface electrodes on the Foturan.

bottom component).

3.5.3 Fabricating a Transmission Mask

The outlet component (Fig. 3.30) is the most complicated component to fabricate as it requires not only electrodes but also a shallow cavity around the outlet of the valve and an outlet hole through the full thickness of the component. These last two features were obtained by carefully controlling the energy dose delivered to the Foturan. It has been established that the etch rate of the crystallised Foturan is dependent on the exposure parameters. It is also reasonable to conclude that the crystallisation (and therefore the etch rate) is dependent on the two step heating process during which the crystallites are first nucleated then grown. The dependence of the etch rate on the heating process was not investigated as the parameters supplied by the manufacturer are widely accepted. Details of the

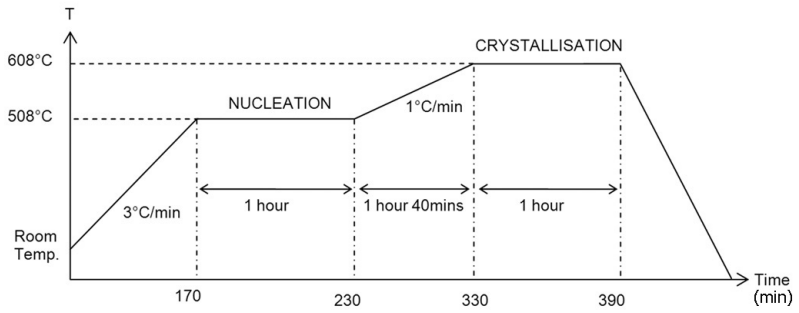

Fig. 3.32: The baking cycle used to nucleate and crystallise Foturan.

baking process is shown in Fig. 3.32. The recommended temperatures for the nucleation and crystallisation steps were $500°C$ and $600°C$ however the temperature of the oven tended to oscillate even when the set point was reached. To prevent the temperature of the oven dropping below the critical temperatures the oven was set $8°C$ above the desired temperature which caused the temperature to oscillate between $500°C$ and $520°C$ ($600°C$ and $620°C$).

It has been shown that it is not possible to produce a usuable stepped profile in a Foturan component using the processes described above as the surface of partially etched (fully crystallised) Foturan is rough and nonuniform. An alternative is to selectively crystallise the Foturan near the surface of the glass so that a step is generated when the crystallised material is completely etched away. This requires careful control of the UV energy density so that only the material near the surface receives an energy dose sufficient to promote crystallisation. This approach would require an intermediate mask with areas of different transmission coefficients. One way of producing such a mask (also known as a grey-scale mask) is to use a matrix of dots of varying pitch and size to locally control the transmission coefficient and its gradient. A simpler approach is to use regions with different absorption coefficients caused by intermediate layers of some absorbing material. As the shadow masks used to produce Foturan components were made from metal layers

sputtered on a glass substrate the thickness of these metal layers were adjusted to produce a simple transmission mask with 3 different transmission coefficients - 0%, 100% and something in between.

The shadow masks were made by sputtering a Ti (or Cr)/Au bilayer onto a glass substrate. Normally, a thin layer of Ti or Cr (10nm) is used to improve the adhesion of the Au layer (100nm) to the glass substrate. To produce a shadow mask a layer of photoresist is spun into the substrate, patterned using photolithography and the metal layers are selectively removed by wet etching. This process was adapted to produce areas where the Au is selectively removed leaving a thin layer of absorbing Ti (or Cr) which will absorb some fraction of the incident radiation.

The first task was to determine the transmission spectra of thin layers of Ti and Cr. Glass substrates were cleaned with IPA and acetone and baked at $100°C$ to remove surface moisture. They were then loaded into a Nordiko PVD system before sputtering layers of Ti and Cr with different thicknesses. Transmission spectrum of the layers was found using a Perkin-Elmer Lambda 7 spectrophotometer. The rate of metal deposition was found by depositing metal for 10mins before measuring its thickness with a Dektak profilometer. The deposition rates were 0.42nm/s for Cr (200W) and 0.31nm/s for Ti (300W).

The optical transmission spectra of Ti, Cr and the glass substrate are presented in Fig. 3.33 (deposition time is used instead of metal thickness). The transmission quickly drops to around 10% after depositing about 15nm of Cr and 11nm of Ti. The thickness of Ti layers is less sensitive to changes in the deposition time so it will be easier to control its transmission properties. The transmission profile of Ti is also more uniform than Cr in the range of wavelengths investigated. For these reasons Ti was chosen for the absorbing layer of the transmission mask. The transmission of the thin metal layers at 312nm was extracted from the transmission spectra and is presented in Fig. 3.34.

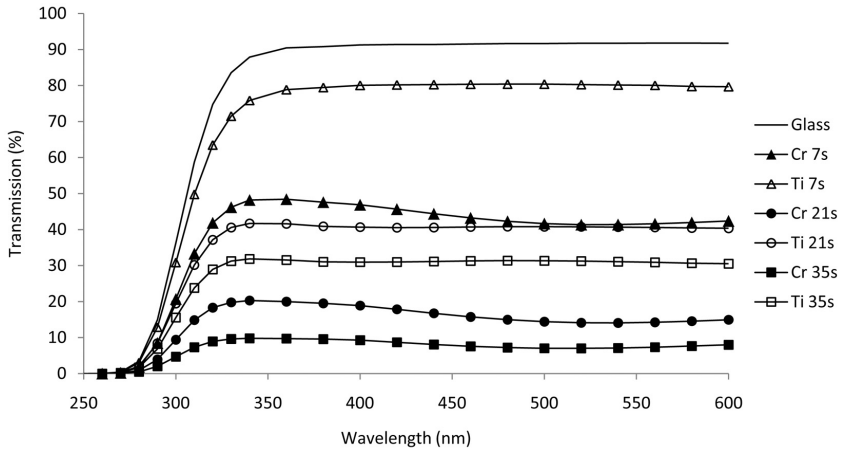

Fig. 3.33: The optical transmission spectra of Cr and Ti on glass.

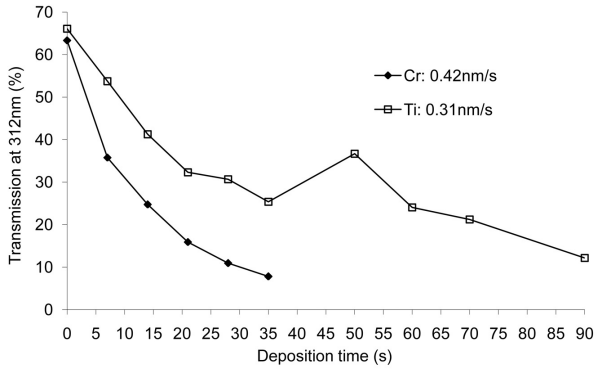

Fig. 3.34: The optical transmission spectra of Cr and Ti at 312nm.

A mask can now be fabricated with 3 distinct regions: transparent regions where the metal layers have been completely removed, regions where the Ti/Au bilayer is present (0% transmission) and regions where only the Ti layer is present (<100% transmission). The required thickness of the absorbing Ti layer also depends on the properties of the UV source, the sensitivity of the Foturan and the depth to which we want to etch the Foturan. First of all the optimum exposure time was found which maximised the etch rate of the Foturan (it was found that overexposure *reduced* the etch rate) then different transmission masks were made with different thicknesses of Ti using the process sequence shown in Fig. 3.35 and described below:

1. A Ti /Au (100nm) bilayer was deposited onto a glass substrate that had been thoroughly cleaned.

2. A layer of photoresist (S1818) was spun onto the substrate (3000rpm), patterned using an appropriate mask which defined the transparent regions (no metal) and developed (MF319).

3. The Au and Ti are then removed by wet etching using a potassium iodide solution to remove the gold and an ammonium flouride based etchant (Laporte) to remove the Ti.

4. The substrate is then throughly cleaned in acetone and IPA to remove all traces of photoresist before spinning a second photoresist layer. The metal layers are so thin that they do not interfere with the spinning of the photoresist.

5. The photoresist is then patterned as before but the mask used this time defines the regions of reduced transmission (Ti only).

6. The Au layer is removed by wet etching to expose the Ti layer.

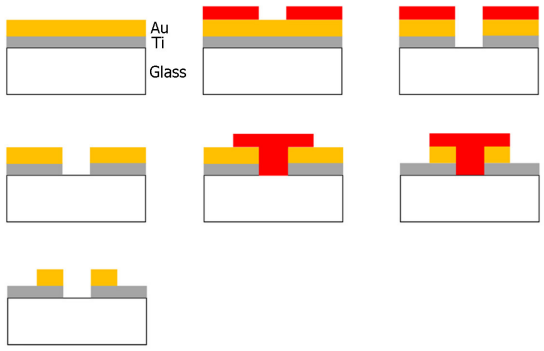

Fig. 3.35: The fabrication process used to make a transmission mask with 3 regions of different transmission coefficients (starting top left).

7. The substrate is finally cleaned with IPA, acetone and distilled water. The mask is now ready to be used to pattern Foturan.

A magnified view of a transmission mask is shown in Fig. 3.36 where the 3 different transmission regions are clearly distinguishable.

In practice the optimum exposure time could not be calculated from the UV lamp output and the transmission properties of the glass substrate used in the mask. The task of optimising the transmission mask was further complicated when the bulb of the UV lamp (H-lamp) was replaced and a second batch of Foturan was required as in each case the optimum exposure parameters and Ti thickness had to be determined by experimentation.

The importance of the exposure time and the thickness of the Ti absorbing layer is illustrated in Fig. 3.37 which shows cross-sections of 3 outlet components made using different exposure times and Ti thicknesses. Starting with the top component the exposure times were 28min and 21.9nm Ti (70s deposition time), 31 min and 25.0nm Ti (80s) and 29 min and 25.0nm Ti (80s Ti). The exposure time was varied slightly from 28min to 31min as this is an easier way to tune the exposure dose than by varying the thickness of the absorbing Ti layer. Fortunately the regions that receive a reduced energy dose are quite sensitive to the dose

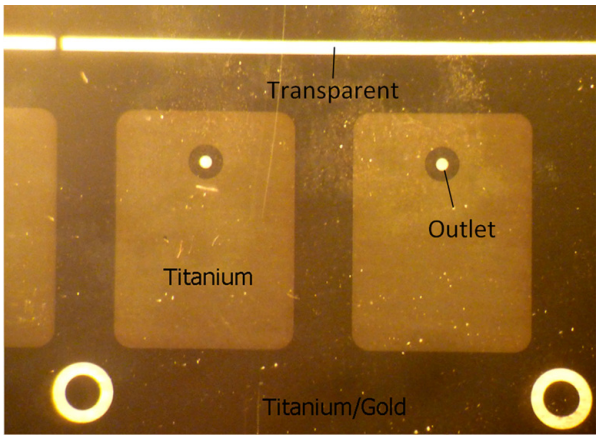

Fig. 3.36: A microscope image of a region of the transmission mask showing the 3 regions - Ti, Ti/Au, transparent. The outlet is 200μm in diameter.

received so that only small variations in exposure time (<1min) are necessary which has little effect on the etch rate of the fully crystallised regions of Foturan.

The transmission spectrum of Ti (Fig. 3.34) indicates that a 21.9nm (70s) layer transmits 21% at 312nm and 25nm (80s) transmits 17% at 312nm. Taking into account the glass substrate which transmits 60% at 312nm, we can estimate that a 21.9nm Ti layer transmits only 13% at 312nm and a 25nm layer transmits 10%.

A more quantative comparison of the bottom two cross-sections in Fig.3.37 is presented in Fig. 3.38 which compares the surface profiles of the same outlet regions found using a Veeco Dektak profilometer (the surface scans have been levelled and shifted for comparison). It is evident that an increase in the exposure time from 29mins to 31mins increases the average etch depth from around 20μm to 70μm. Local variations in etch depth of 10μm or more are common illustrating the nonuniform etch rate. The two well defined peaks on the left side of the image are the edges of the valve outlet, the outlet orifice itself appears to be only about 110μm in depth because the diameter of the profilometer stylus was larger than the outlet.

The energy delivered to the Foturan can be estimated from the exposure times and

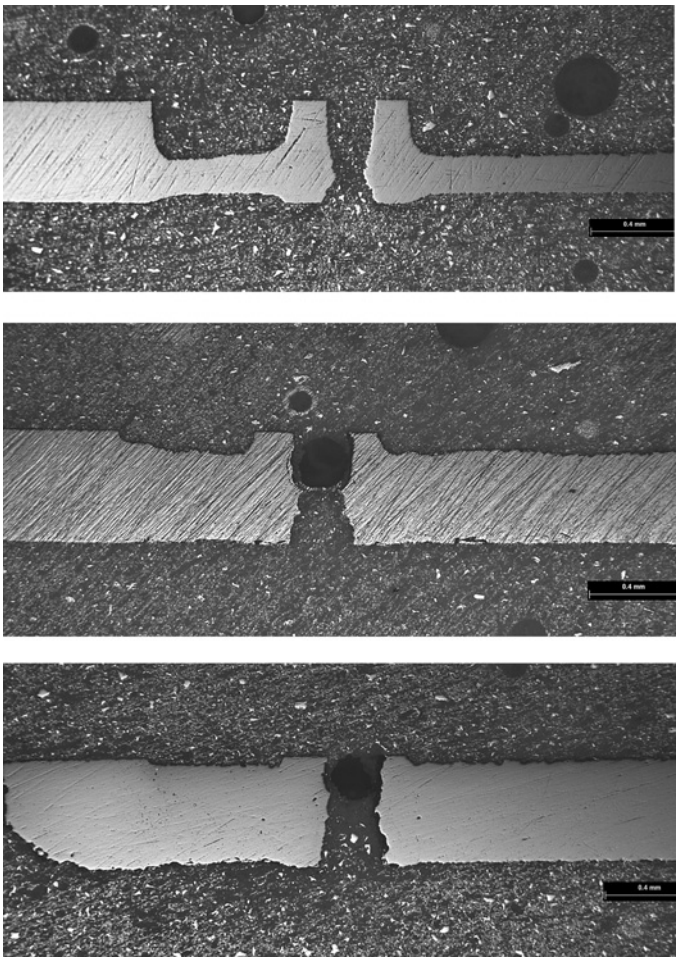

Fig. 3.37: Magnified outlet cross-sections showing the effect of different absorbing Ti layers and exposure times. Top to bottom - 28min exposure, 22nm Ti; 31 min, 25nm Ti; 29min 25nm Ti.

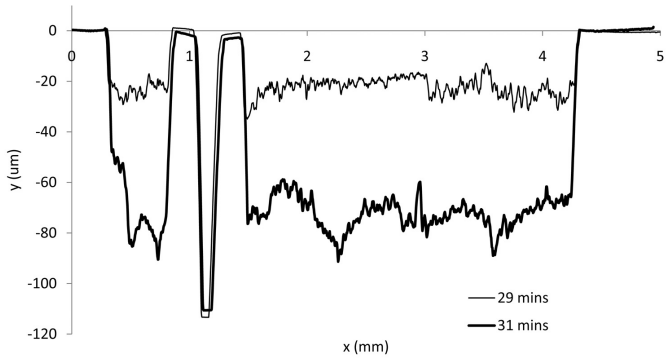

Fig. 3.38: The surface profile of two outlets - 29min/31min exposure, 25nm Ti.

the opacity of the different transmission masks. If we recall the simple calculations in the previous section that estimated the energy incident on the Foturan at 312nm (through the glass substrate without an absorbing Ti layer) to be $8.4mWcm^{-2}$ then the total energy delivered to the bottom outlet component in Fig. 3.37 in 29min is $14.6Jcm^{-2}$. As 25nm of Ti was found to transmit only 10% at a wavelength of 312nm then the delivered energy dose in these regions was only around $1.5Jcm^{-2}$. The effect that such a low exposure dose has on the etching of Foturan is illustrated in Fig. 3.39 which shows the outlet region of a valve. In this region of the Foturan the number of nucleating centres per unit volume is low enough to produce the pitting seen in the magnified image. It would appear that the small number of crystallites are surrounded by amorphous material which results in only small areas being etched. This appears to be surface crystallisation, however, the back surface of the outlet component also etches albeit to a lesser degree than the front surface. Although the thickness of the Foturan absorbs some of the intensity the back surface receives enough radiation to be partially crystallised as indicated by Fig. 3.40 which shows the surface profile of the back surface of an outlet component (exposed for 29mins through 25nm Ti). The rear surface has been etched to an average depth of around $15\mu m$ and the edge of the outlet orifice is less well defined. A direct comparison of the dimensions of the outlet at the front and rear surface of the outlet component is presented in Fig. 3.41 which superimposes them (the actuator makes contact with the front surface of the outlet). The outlet is slightly diverging as the orifice is about $110\mu m$ wider at the rear surface, this may be due to scattering of the incident UV light which will disperse and broaden the features. This etch damage on the back surface of the outlet can be removed by polishing if necessary.

As the etch rate of partially crystallised regions of Foturan is sensitive to the exposure dose another factor that must be considered is the *uniformity* of the lamp output over the dimensions of the sample. Changes in the intensity of $0.4mWcm^{-2}$ (at 405nm) over 4cm were observed in the sample chamber of the UV

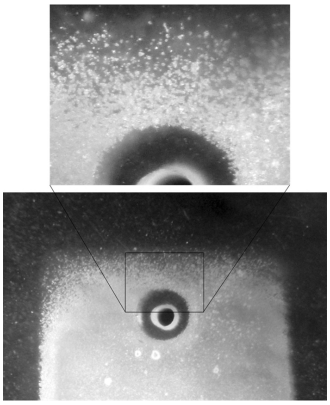

Fig. 3.39: Detail of the Foturan surface after exposed through the transmission mask and etching (circular outlet diameter = 200μm).

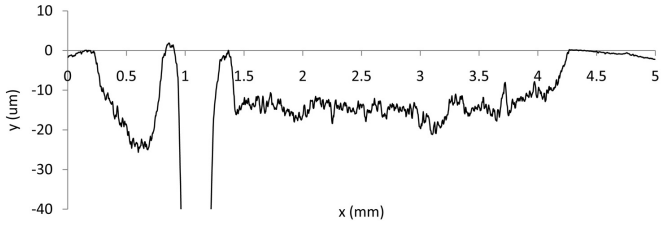

Fig. 3.40: The surface profile of the rear surface of an outlet (29min exposure, 25nm Ti)

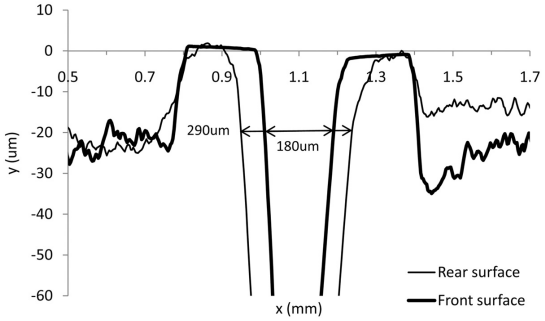

Fig. 3.41: Lateral etching of the Foturan causes the outlet orifice to diverge from 180μm to 290μm.

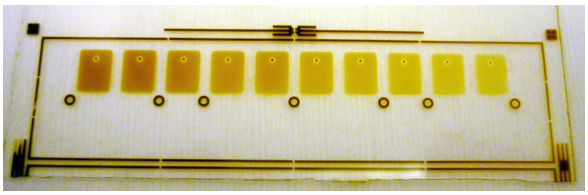

Fig. 3.42: This outlet component shows the effect of a non-uniform UV source.

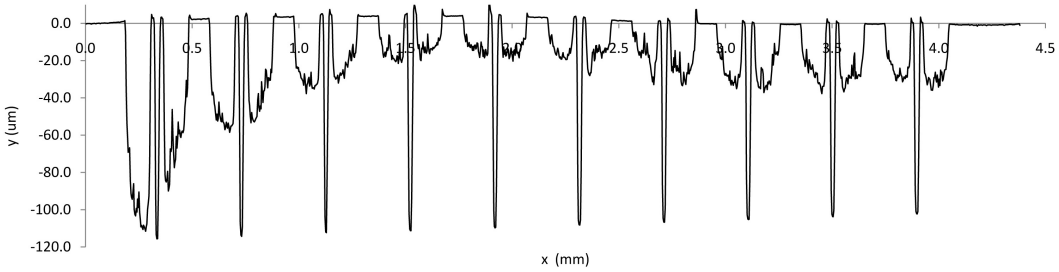

Fig. 3.43: The surface profile of an array of ten outlets shows the non-uniform etching caused by a non-uniform UV source.

source. While this would have little effect on the regions that will be fully crystallised, the effect of this variation in intensity on the regions that will be partially crystallised is illustrated by Fig. 3.42. The colour of the Foturan after heat treatment is a good indication of the amount of crystallisation, the darker the glass the greater the crystallisation. The variation in colour of the partially crystallised regions is clear and would result in the etch rate dropping from left to right. The surface profile of all 10 outlets in this valve array after etching and release is shown in Fig. 3.43. The etch depth of the partially crystallised regions around the outlet varies from around $100\mu m$ to $30\mu m$ over the width of the array (45mm). A surface profile like this could lead to mechanical failure if such a valve is pressurised as the valve body is considerably thinner where the etch rate was higher. Another contributing factor to this effect could be variations in the thickness of the Ti layer, however, this was not investigated.

The final stage of the fabrication process is the bonding of the components. This

was done by first cleaning the components with IPA and acetone and then applying a small amount of UV sensitive epoxy (Dymax 9-20553). The alignment holes allowed the components and actuators to be stacked and aligned before mounting a 2kg mass on the stack to seal the stack. The epoxy was hardened by exposing it for 2 mins under the same UV lamp used to sensitise the Foturan.

3.5.4 Microvalve Fabrication - Summary

The final microvalve design consisted of six Foturan components which are shown in Fig. 3.44 along with an assembled microvalve array. Two of the components require metal electrodes (1 and 6) and only one component requires the use of a transmission mask (1). Components 5 and 6 work together so that a single inlet of component 6 can supply two valves via the larger cavities in component 5, this approach simplifies the inlet connections to the valve. These two components could be replaced by a single component with 10 inlets, one inlet per valve, which would allow control of the individual valves. The fabrication process can be detailed as follows:

(**Note**: The following process assumes that the optimum exposure conditions of the Foturan have been found to maximise the etch rate, a transmission mask has been made with a suitable absorbing layer of Ti for the outlet component and a shadow mask has been made for the deposition of the electrodes)

1. Expose the Foturan components through the mask for the optimum time taking care to consistently position the components in a region of uniform intensity.

2. Bake the Foturan components for 1hr at 500°C (3°C/min ramp rate) then at 600°C for 1hr (1°C/min ramp rate). Allow to cool slowly to room temperature.

3. Prepare a solution of 40% by weight of Apiezon Black Wax (BW) in toluene and spin a $10\mu m$ layer on a rigid, flat polishing disk (4-inch glass wafer about 10mm thick). Bake the disk on a hotplate at $120°C$ under a fume hood for 5mins to remove the solvent.

4. Apply a uniform layer of BW onto one side of the Foturan components and bake on a hotplate to remove the solvent (there may be bubbles in the BW).

5. Allow the components to cool and sandwich them with a second glass polishing disk (BW surface to BW surface).

6. Put the sandwiched components in a vacuum oven and allow them to reach $120°C$ under vacuum. This will help to remove bubbles from between the Foturan components and the substrate. Also place a 2kg mass in the oven to heat up to temperature.

7. When temperature has been reached open the oven and put the mass on top of the sandwich before pumping down the oven and leaving the sandwich for 1hr under vacuum. Take care that the sandwich is on a flat surface otherwise the top and bottom glass disks will slowly slide over one another moving the Foturan components.

8. After 1hr remove the sandwich from the oven and allow it to cool with the mass in place.

9. Clean the excessive BW from the surface of the Foturan components and the supporting glass disk and lap with $9\mu m$ and $3\mu m$ calcined aluminium oxide powder until the surface is flat (around 1 hour at 70rpm per component for each grade of abrasive). Finer abrasive can be used for the components that will have electrodes sputtered on the surface.

10. The components can be removed from the substrate by heating it to $120°C$ and *carefully* sliding the components off, or by putting the substrate in

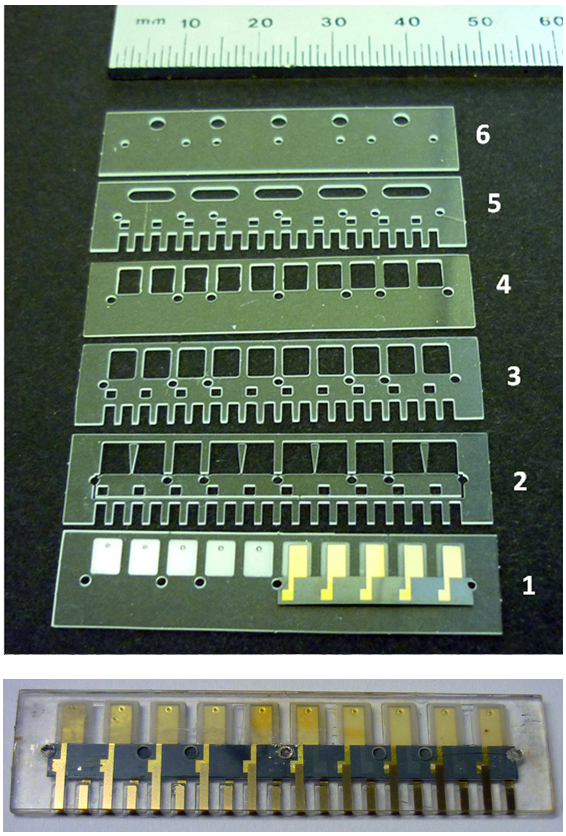

Fig. 3.44: The Foturan components used to construct the microvalve (top) and an assembled microvalve array (bottom) with dimensions 11x46x2mm.

toluene. The components should be cleaned with toluene and acetone before turning them over and repeating the above process for the second surface.

11. Now that the components have been planarised and polished they can be etched in 10% HF solution in an ultrasonic bath, which should take between 30-40minutes to etch away all of the crystallised Foturan.

12. The Ti/Au electrodes can now be sputtered using an appropriate shadow mask (depending on the condition of the Foturan surface they may benefit from further polishing using a fine abrasive before sputtering).

13. The components and actuator are ready to stack and bond with a suitable epoxy.

3.6 Microvalve Testing - Pitot Probe

To investigate the behaviour of the microvalve under different operating pressures and applied voltages, a clamp was designed to secure the microvalve to a plenum chamber as shown in Fig. 3.45. The plenum chamber and three ports were machined out of a transparent acrylic block, two of the ports were for the compressed air supply and the third port allowed a pressure gauge to be attached to indicate the internal pressure of the plenum chamber. The plenum acts as a settling chamber to provide a low dynamic pressure and uniform flow at the inlets to the microvalve. Relative to the total size of the microvalve outlet the plenum chamber cross-sectional area was approximately 3 orders of magnitude greater, consequently, for the total mass flows encountered during this study, the expected plenum flow velocity is expected to be in the order of 0.1 m/s therefore the dynamic pressure in the plenum chamber is almost negligible and the plenum static pressure is considered as the reference total pressure for the jet (P_0). The aluminium plate that clamped the microvalve array to the plenum chamber was 2mm thick and had chamfered holes (1mm smallest diameter, 3mm largest diameter) which allowed the air jets to develop freely as they expanded out of the microvalve outlets. Before clamping the microvalve array the surface of the plenum and the aluminium clamping plate were carefully cleaned with IPA and blown with compressed air to remove dust and a silicone gasket (2mm thick) was cut to size and placed around the perimeter of the microvalve array. A small amount of vacuum grease was applied to the periphery of the microvalve surface that will contact the plenum and around the microvalve outlets. A thin polyimide film was also placed between the array and the aluminium plate and windows were carefully cut to expose the outlet holes. For accurate measurements of the internal pressure of the plenum chamber it is important that there are no leaks.

Although the measurement of jet flows is well established at larger scales, there is very little work reported at the small scales considered in this study.Most

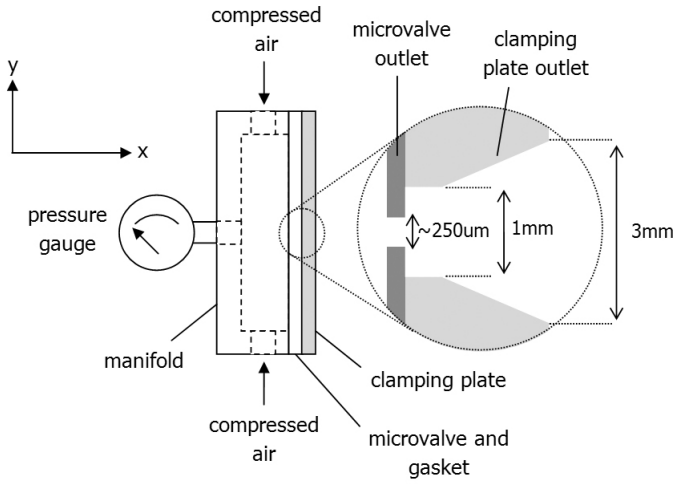

Fig. 3.45: Details of the plenum chamber and clamp that is used to test the microvalve.

aerodynamic measurement techniques are not well suited to such small flows and although there have been recent developments in the use of non-intrusive methods for micro-scale flows these are primarily focused on studies where the fluid is a liquid. For air flows, the main difficulties arise simply due to the relative size of the flow features and the measurement tool. The objective of this study was to determine the basic operating characteristics of the jet and therefore a relatively simple approach was adopted.

A Pitot probe was used to measure the jet stagnation pressure at a range of streamwise (in the direction of the flow) and spanwise (in a direction perpendicular to the flow) positions relative to the jet outlet. The Pitot probe is a conventional tool used to examine the characteristics of a uniform flow of an incompressible liquid or gas [66]. A typical Pitot probe is placed in a flow as shown in Fig. 3.46 (top). The flowing fluid builds up and is brought to rest at the mouth of probe, this is called a *stagnation point*. Bernoulli's equation relates the pressure and velocity at point 1 to the total or *stagnation pressure* at 2:

$$P_1 + \frac{\rho U_1^2}{2} = P_2 \tag{3.6}$$

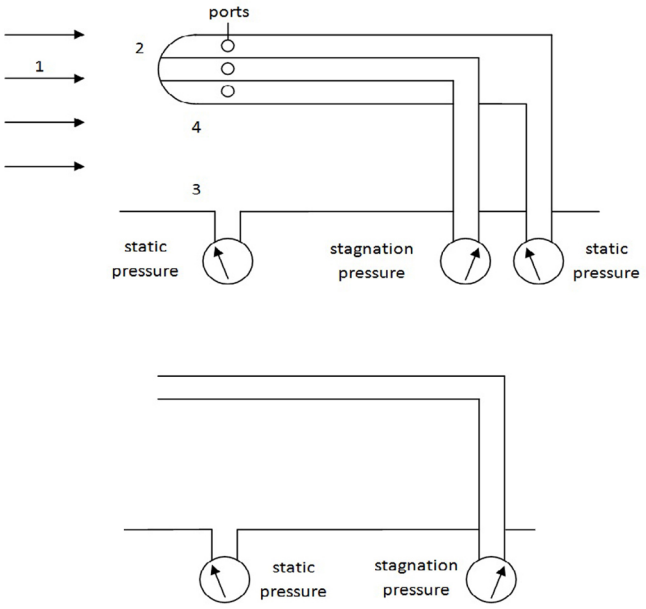

Fig. 3.46: the principle of operation of a Pitot probe.

where ρ is the fluid density and $\frac{\rho U_1^2}{2}$ is the *dynamic pressure*. The velocity can therefore be described in terms of the difference between the *static pressure* at 1 and the *stagnation pressure* at 2:

$$U_1 = \sqrt{2\left(\frac{P_2 - P_1}{\rho}\right)} \tag{3.7}$$

If the flow is approximately parallel near the probe and the probe is slim and streamlined enough so that the flow is approximately parallel around the probe then the static pressure at 1 is approximately equal to the pressure at the wall 3 and near to the probe 4, that is $P_1 \simeq P_3 \simeq P_4$. The time averaged flow velocity is found by measuring the difference between the stagnation pressure P_2 and the static pressure P_1 or between P_3 an P_4. We are only interested in the stagnation pressure P_2 so Fig. 3.46 (top) can be simplified to give the bottom figure.

For the case of incompressible flow the static pressure and stagnation pressure are related by [67]:

$$\frac{P_2}{P_1} = \left(1 + \frac{\gamma - 1}{2} M^2\right)^{\frac{\gamma}{\gamma - 1}} \tag{3.8}$$

The Mach number is given by $M = U_1/C_1$ where C_1 is the speed of sound in the free stream and γ is the ratio of specific heats for air. This is valid if the fluid is incompressible and $M < 0.3$. If $0.3 < M < 1$ then the flow is supersonic and a shock wave forms upstream of the probe mouth and the above relation is no longer valid. The Mach number can be used to calculate the local flow velocity using the expression:

$$U = M\sqrt{\gamma RT} \tag{3.9}$$

where R is the ideal gas constant, T the static temperature and U the gas velocity.

While Pitot probes are relatively simple there can be several sources of error that must be considered such as misalignment with the flow, shear and turbulence in the flow, wall interference, vibrations, viscosity and compression. Pitot probes with a square cross-section are least sensitive to misalignement errors and can tolerate misalignments of $< 20°$. If the Pitot tube is too narrow, the Reynolds number too low, or the fluid is highly viscous then strong viscous effects take place which introduce uncertainty. Errors are also introduced if the probe is placed in regions of strong turbulence or shear as the probe will sense the average pressure. Wall effects are significant if the probe is closer than 3 tube diameters to the wall as the wall causes the flow around the probe to be asymmetric and the velocity measurement will be less than the actual. It has been stated that the overall accuracy of total pressure measurements is <0.25% provided that the Reynolds number (based on the probe diameter) >100, the probe is aligned within $\pm 10°$ to the flow, turbulence is <5%, the total pressure does not change more than 2% across the probe diameter, the probe is not near a wall and the compressible flow equations apply (M<0.3). Generally, all of these criteria are rarely satisfied so some errors should be expected.

The small dimensions of the airjet generated by the valve outlet meant that conventional Pitot probes were too large therefore the probe used in this investigation was a 30G gauge hypodermic needle which was ground flat at its tip

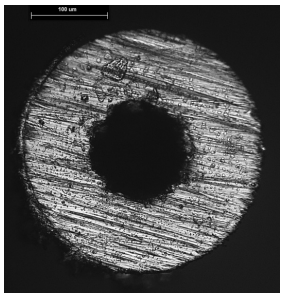

Fig. 3.47: The cross section of a 30 gauge hypodermic needle used as the Pitot tube (scale = $100\mu m$).

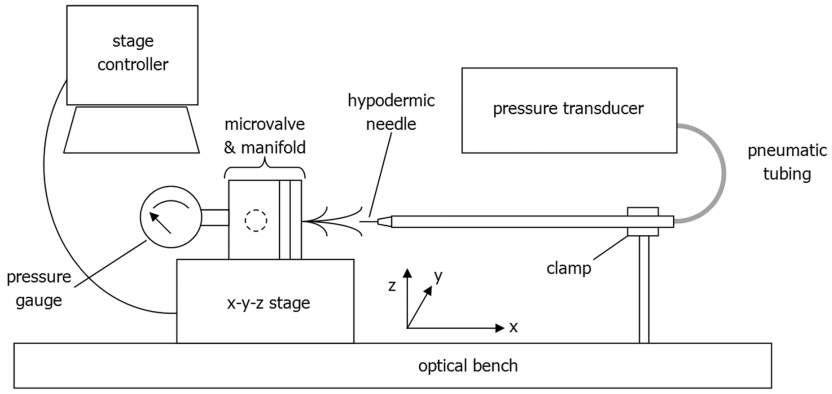

Fig. 3.48: The experimental setup used to make Pitot probe measurements of the jet flow.

to present the Pitot probe orifice as normal to the flow direction. It has an unchamfered tip with an inner diameter of $140\mu m$ and an outer diameter of $310\mu m$ (Fig. 3.47), consequently, the size of the Pitot probe is of the same order of magnitude as the jet diameter. The Pitot probe effectively provides a pneumatically averaged measurement of the local stagnation pressure, therefore in regions of the jet where there are flow gradients this will result in the Pitot probe providing a spatially averaged reading. As the aim of this work is to determine the basic jet characteristics and the sensitivity to the microvalve operation, this simple measurement approach is sufficient.

The arrangement of the testing equipment is given in Fig. 3.48. The Pitot probe was fixed in space and the microvalve was mounted on an x-y-z stage to provide relative positioning between the jet and the measurement location. The axial resolution (x direction) of the pressure measurements was 0.5mm and the lateral resolution (y direction) was 0.25mm. Pressure measurements were made in a planar region along the jet plane of symmetry to provide measurements in both streamwise (x) and spanwise (y) locations. The Pitot probe was connected via pneumatic tubing to a Druck DPI145 differential pressure indicator which is a 70kPA sensor with an uncertainty of 0.025% of full-scale. The Pitot pressure measurements (P_{Jet}) were taken relative to the atmospheric pressure (P_{atm}). The same pressure indicator was also used to measure the total pressure (P_0) in the plenum chamber. For these tests the plenum pressures relative to atmospheric pressure were 20, 40, 60 and 80kPa. Given the very small size of the jet diameter, a key aspect was to position the Pitot probe at the centre of the jet. This was achieved by determining the location of the measured total pressure maximum in the x,y, and z directions 1mm from the outlet.

The temporal sensitivity of the Pitot measurement system depends on the time for the pressure wave to propagate from the probe to the transducer. In turn, this time increases as the tubing bore reduces and also increases with tubing length. In this arrangement, due to the very small bore hypodermic tubing, a conservative approach was taken and a 120s settling time was used at each new Pitot measurement location before pressure data was recorded. Due to the low bandwidth of the transducer and the damping in the hypodermic tubing, the pressure measurements did not capture any of the *unsteady* aspects of the flow field, however, the system does provide a time mean measurement of the jet total pressure. The jet pressure data is presented in the form of the non-dimensional ratio P_{Jet}/P_0 where P_{Jet} is the gauge total pressure in the jet and P_0 is the gauge total pressure in the manifold . The axes which indicate spatial position are also non-dimensionalised with respect to the jet hole diameter, D (i.e. $x/D, y/D$).

Chapter 4

Results and Discussion

The results of this project can be separated into three categories (1) calibration of the silicon springs, (2) characterisation of the actuators and (3) characterisation of the microvalve.

As described in the previous chapter the silicon springs were defined by dry etching a $300\mu m$ silicon wafer. The normal spring constants of the springs were determined by dimensional models and both static and dynamic techniques. The dimensional models were analytical descriptions of the spring constant that were based on the material properties and geometry of the springs. These models were the conventional Euler-Beroulli model of a bending beam, a modified Euler-Bernoulli model which accounted for the trapezoidal cross-section of the beam and a finite-element model. The mechanical resonance of the springs was found by laser-Doppler-vibrometry and substituted for the spring thickness in Clifford and Seah's dimensional model in what can be described as a semi-dynamic method. The other dynamic technique used the change in resonance frequency of the spring after the addition of a small end mass to calculate its spring constant. The results of these methods are compared to the static method of applying a known mass to the spring tip and measuring its deflection.

The characterisation of the bimorph actuators was mainly focused on measuring the tip deflection and force with respect to the applied voltage. The deflection

hysteresis tells us something of the state of the piezoelectric ceramic and the poling conditions used to prepare the bimorph. The force measurements are made off-end and require correcting so details of how these correction factors are calculated and applied are also presented. The behaviour of the actuators under dynamic operation is important for applications involving the generation of synthetic gas jets and so the dynamic deflection as a function of applied AC and DC offset voltage is presented. The dynamic response of the bimorph actuators is discussed in the context of the electromechanical coupling coefficient.

The behaviour of the actuators has a direct impact on the performance of the microvalve as will be described in the sections dealing with the static and dynamic behaviour of the microvalve. Due to the small scale of the microjets a simple Pitot probe was used to determine the pressure profile outside the valve outlet. While unable to give time-dependent information about the microjet it provides a relatively easy way to estimate the mean velocity of the airjets.

4.1 Spring Calibration

The important data that is needed to calibrate a reference spring (i.e. determine its normal spring constant) using static and dynamic methods is either its deflection under a given static load or the fundamental resonance frequency of the spring. The deflection per unit load gives a direct measure of the spring constant while the resonance frequency of the spring needs to be combined with other information about the reference spring such as its dimensions, material properties and the magnitude of any off-end masses to determine the spring constant. Dimensional methods only require the spring dimensions and material properties to calculate the spring constant. The calibration methods which will be used in this section have already been described in previous chapters and they should be referred to for further details. Rather than present the results of the various calibration methods separately in each subsection they will be presented together so they can be compared. The data presented in this section relates mostly to the rectangular cantilever springs as there was insufficient time to adequately test the V-shaped springs. Dimensional and finite element results for the V-shaped springs are presented, however, static and dynamic added mass results are not presented as they were extremely scattered and showed little connection to the spring dimensions. Unfortunately, end masses were also sintered onto the V-shaped springs and there was no time to try to remove them and repeat the measurements (the resonance frequency of the V-shaped springs is presented in Appendix B).

The DRIE process that defined the reference spring dimensions consisted of two steps, etching and passivation, that were repetitively alternated (see Table 3.1). The passivation step deposits a polymer over the surface of the wafer which is easily removed from horizontal surfaces but which remains on sidewalls and improves the directionality of the etch and increases the aspect ratios of etched features. Figure 4.1 shows the profile and cross-section of a cantilever spring etched from a $300\mu m$ <111> silicon wafer using DRIE. A small amount of lateral

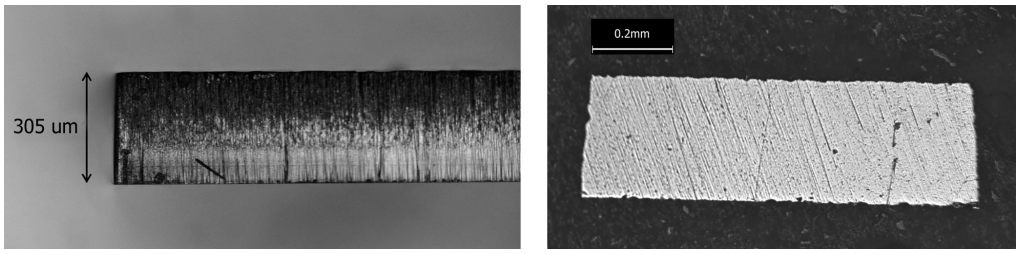

Fig. 4.1: The profile and crosss-section of a cantilever reference spring.

etching during the DRIE process is indicated by the trapezoidal cross-section of the spring. The lateral etching was measured optically and found to be around $50\mu m$ at the top surface and $8\mu m$ at the bottom surface of the spring. The average wall angle was 4°. These dimensions were used in Poggi's dimensional model of a cantilever spring with a trapezoidal cross-section [20]. Once the spring dimensions were measured it was a simple matter to insert this information into the dimensional and finite-element models to determine the normal spring constant and the resonance frequency.

The fundamental resonance frequencies of the cantilever springs as found from the finite-element model and from the LDV spectra are presented in Fig. 4.2. There is good agreement particularly for longer springs (tabulated data can be found in Appendix B). Fig. 4.3 presents the spring constants calculated using the dimensional models. The results of the static mass measurements are also shown for comparison though details of these measurements will be described in the next section. As expected the FE model closely corresponds with the Euler-Bernoulli and Poggi models which are themselves indistinguishable. This is not surprising because the moment of inertia of a beam with a trapezoidal cross-section (as used by Poggi) converges to that of a rectangular beam (Euler-Bernoulli) when the difference between the top and bottom dimensions falls to zero.

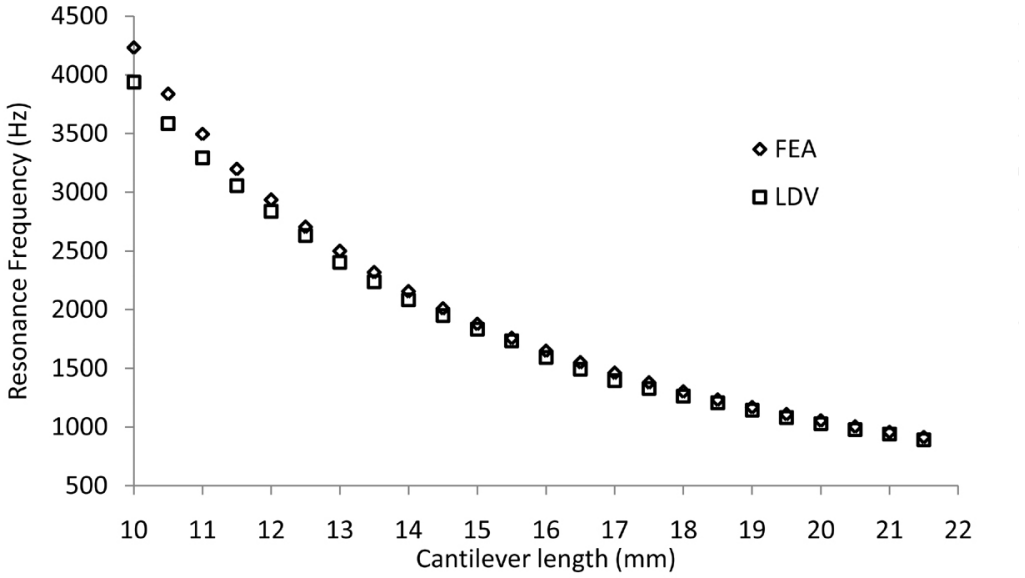

Fig. 4.2: The fundamental resonance frequency of cantilever springs found using LDV and FEA.

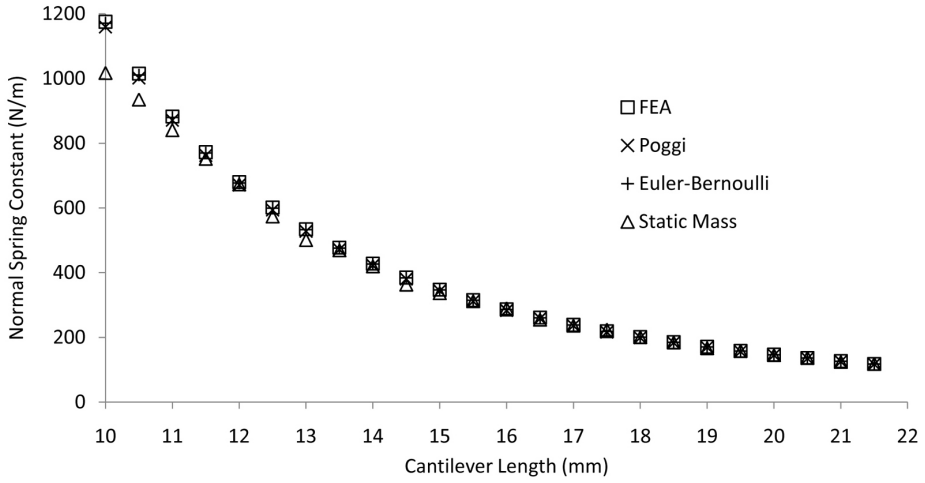

Fig. 4.3: The normal spring constant of the cantilever springs determined using dimensional models.

4.1.1 Static Calibration

The static calibration measurements shown in Fig. 4.3 were subject to two main sources of error that must be corrected: the error in the magnitude of the static mass due to off-end loading and the error in the deflection magnitude due to off-end measurements. To correct for these errors we first convert the off-end deflection to a tip deflection. This deflection error is simply a product of the tip gradient and the off-end distance. The larger the tip deflection, the larger the gradient of the spring will be near it's tip and hence the deflection error. To correct this the finite-element model was used to determine the tip gradient of the springs by applying different loads (2-10mN) and extracting the tip profile. The tip gradient was determined by listing the deflections of nodes defined by a user specified path which extended from the tip to the off-end distance. The first step in this process is illustrated in Fig. 4.4 which relates the deflection measured at an off-end distance to the deflection at the tip of a 10mm cantilever spring. It is useful to present the data in the form of Fig 4.5 which plots the deflection error that is associated with a measured deflection. As expected the off-end deflection increases linearly with tip deflection as the spring deflections are small and the spring bends relatively uniformly along its length. The gradient of the line in Fig.4.5 can therefore be used to estimate the necessary deflection correction for any measurements made on the 10mm cantilever with an off-end distance of $500\mu m$. For example, for a measured deflection of $7\mu m$ the deflection error will be given by 0.079×7 which gives $0.55\mu m$. These plots were repeated for all the fabricated springs as shown in Fig. 4.6 which conveniently contains all the information that is needed to correct for deflection measurements made $500\mu m$ from the spring tip. Fig.4.6 also shows that the deflection error of the V-shaped springs is well approximated by the deflection error of a cantilever spring. This is expected as the width of the arms of the V-spring is about half of the width of the cantilever spring so the parallel beam approximation applies.

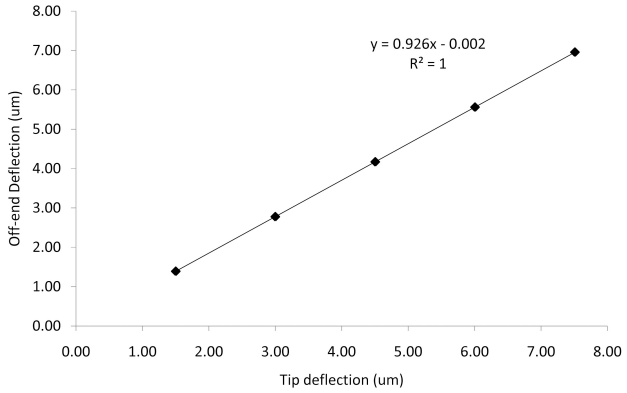

Fig. 4.4: The off-end deflection against tip deflection for an off-end distance of $500\mu m$ and a 10mm cantilever spring.

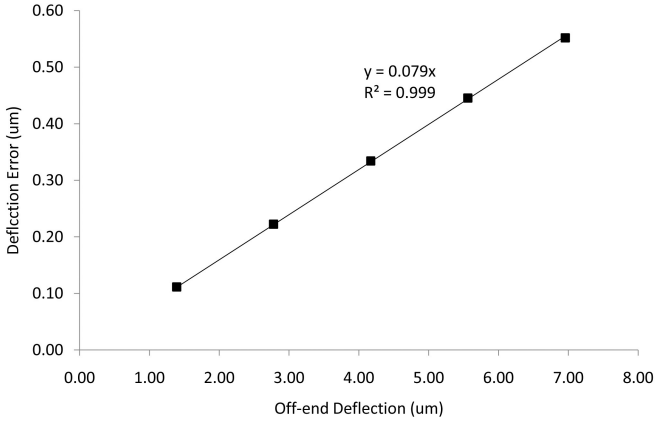

Fig. 4.5: Deflection error as a function of the measured (off-end) deflection (off-end distance=$500\mu m$, 10mm cantilever spring).

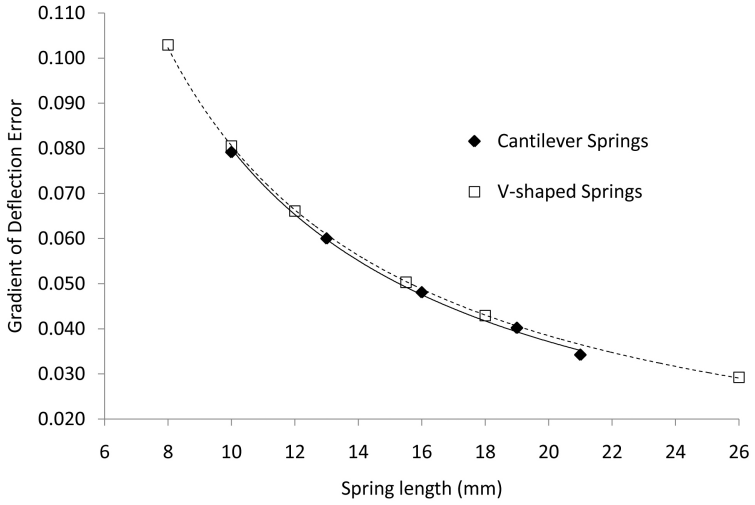

Fig. 4.6: The gradient of the deflection error as a function of spring length for cantilever and V-shaped springs.

After calculating the tip deflection the next step is to convert the off-end mass to a tip mounted mass by using equation 2.48:

$$M_{eff} = M_{meas}\left(\frac{L-\Delta L}{L}\right)^3$$

where M_{meas} is the magnitude of the loaded mass found using a precision balance, M_{eff} is the effective mass of an equivalent mass perfectly mounted at the tip of the spring, L is the length of the spring and ΔL is the off-end loading position of the mass. Now that the tip deflection and tip force are known the spring constant shown in Fig. 4.3 was calculated.

4.1.2 Determining the Resonance Frequency

All dynamic calibration methods use the fundamental resonance frequency to determine the spring constant of the calibrated spring. The resonance frequency of the reference springs was determined using a Polytec laser-Doppler-vibrometer. This instrument physically excites the springs over a range of frequencies with a piezoelectric element while simultaneously measuring the magnitude of the vibration of the spring at a user defined point. In this way a spectrum is obtained that shows how the amplitude of the mechanical vibrations changes as the driving frequency changes. The vibration amplitude reaches a maximum at the fundamental resonance frequency of the spring structure. An example of such a spectrum is given in Fig. 4.7 which presents a plot of vibration amplitude as a function of excitation frequency (500-20kHz) for a 21.5mm long cantilever spring. The spectrum clearly shows the first three vibration modes of the spring, the fundamental frequency being around 1kHz. It is interesting to note the secondary peaks around these three vibration modes which are more visible in Fig. 4.8. These peaks arise because the reference springs are fabricated in groups of six and behave as coupled resonators.

To determine the position of the resonance frequencies a Matlab script was used which employed a simple peak-finder function to extract the fundamental resonance frequency along with the frequencies of the secondary resonance peaks due to adjacent reference springs.Table 4.1 presents the resonance frequencies extracted from the spectra. The six columns in Table 4.1 present the six resonance peaks corresponding to the six reference springs and the number in bold is the position of the primary resonance for the reference spring indicated in the left-hand column. If the magnitude of the resonance peak was very small it was difficult to correctly identify them without also picking out the anti-resonance peaks and any small ripples due to noise. For example, in Fig. 4.8 all six resonance peaks can be visually identified, however, the peaks due to spring 19 and 20 are not listed in

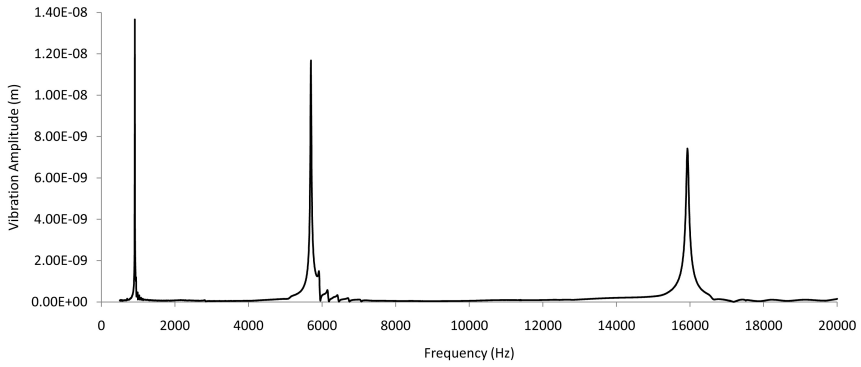

Fig. 4.7: The frequency dependence of the amplitude of the vibrations of an externally driven 21.5mm cantilever spring.

Spring No.	***Length (mm)***	**Resonance Frequencies (Hz)**					
19	19	-	947	984	1031	1078	**1134**
20	19.5	-	947	988	1031	**1081**	1131
21	20	906	947	988	**1034**	1078	1131
22	20.5	906	947	**988**	1031	1078	1131
23	21	906	**950**	988	1031	1078	-
24	21.5	**909**	947	984	1031	-	-

Table 4.1: Resonance peaks for cantilever springs 19-24. The bold numbers indicate the fundamental frequencies and the other numbers indicate the frequencies of the satellite peaks caused by the other springs in the array.

Table 4.1 as they were too small for the Matlab algorithm to easily identify.

By overlapping the resonance spectra for all the cantilever springs in the array (Fig. 4.9) we can see that, as expected, the secondary peaks closely correspond to the fundamental resonance peaks of the neighbouring springs. Table 4.1 lists the positions of the peaks in Fig. 4.9 which indicates that the secondary peaks are consistently identified to within about 4Hz which is close to the frequency resolution of the LDV (Δf =3.25Hz). A single spectra can therefore be used to find the resonance frequencies of an array of springs as long as the spring that is measured is in the middle of the spring array, in this case spring numbers 21 or 22.

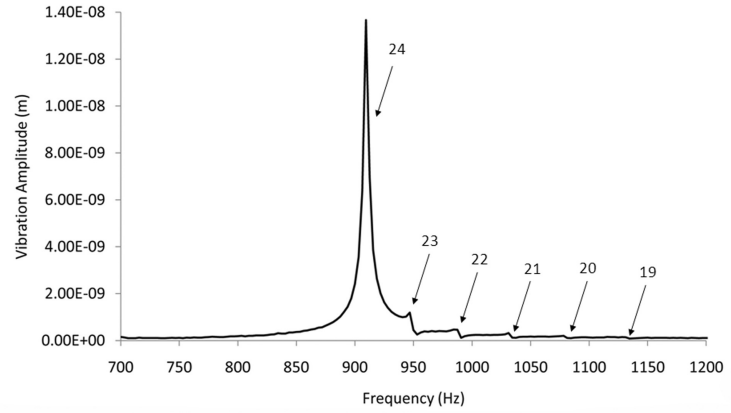

Fig. 4.8: The fundamental resonance frequency of a 21.5mm cantilever in an array of six springs. The numbers indicate the neighbouring springs that correspond to the smaller resonance peaks.

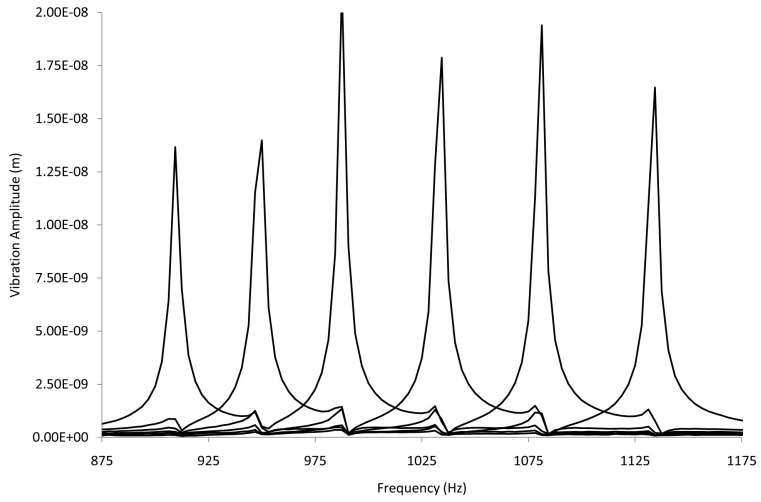

Fig. 4.9: The vibration amplitude spectra of six cantilever springs (19-21.5mm). Note how the smaller secondary resonance peaks closely correspond to the fundamental resonance frequencies of the neighbouring reference springs in the array.

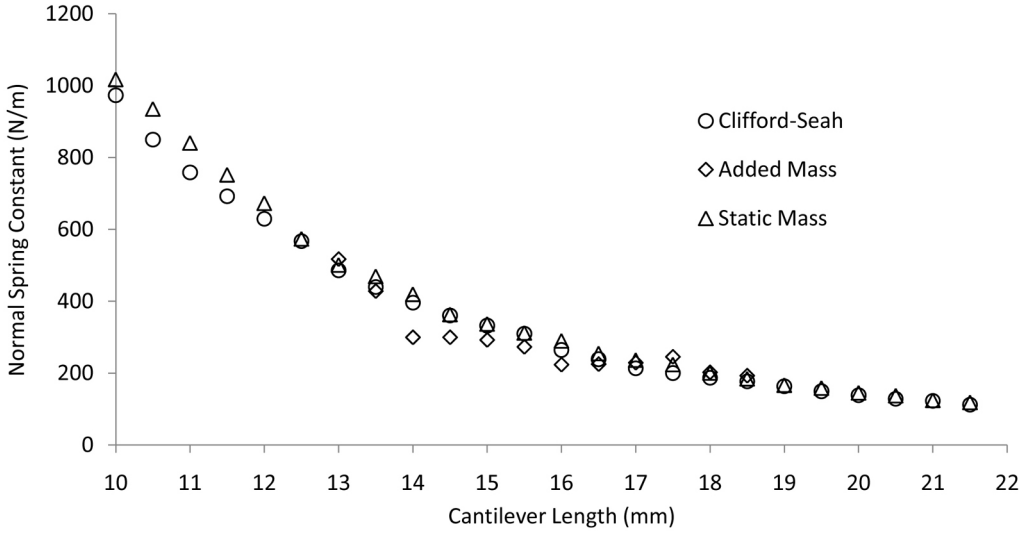

Fig. 4.10: The spring constants of the cantilever springs found using dynamic calibration methods. Static deflection results are included for comparison.

4.1.3 Dynamic Calibration

The resonance frequencies determined from the LDV spectra were substituted into a dimensional expression for the spring constant of a cantilever (Clifford and Seah's method, equation 2.34), the results of which are shown in Fig.4.10 along with the static mass and dynamic added mass results. As described in the previous section the dynamic added mass method is very time consuming and rather tedious to implement so it was only used to characterise cantilever springs of length 13-19mm (spring no. 7-18). A graph of the added mass m vs $1/(2\pi f_0)^2$ was plotted and the gradient of the line, which represents the spring constant, was found (see section 2.2.3 and equation 2.39). The spring constants for the cantilever springs found using this method are shown in Fig. 4.10 and an example of a m vs $1/(2\pi f_0)^2$ plot for a 16mm cantilever spring is shown in Fig. 4.11. These results will be discussed in the next section.

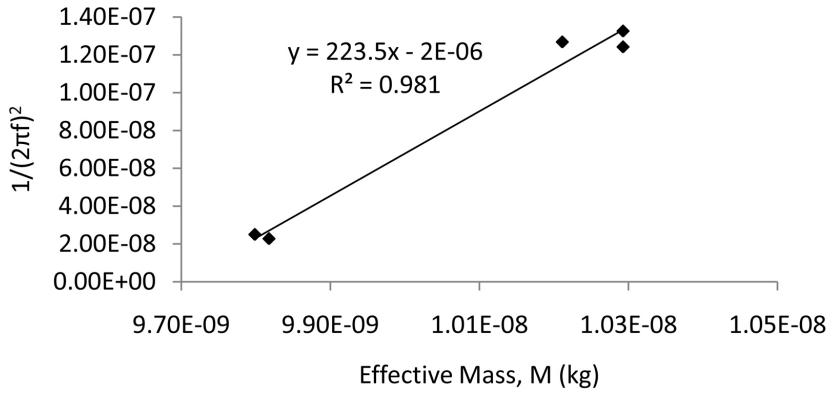

Fig. 4.11: An example of how the spring constant of a 16mmm cantilever spring is found from a plot of the effective added mass M vs $1/(2\pi f_0)^2$ where f_0 is the new resonance frequency after addition of the mass.

4.1.4 Overview - Spring Calibration

The calibration methods used to determine the normal spring constant varied in complexity and difficulty to implement. The easiest calibration methods were the dimensional models that required knowledge of the spring dimensions which were easy to determine from optical measurements and the material properties that were available from the manufacturer. The spring constants calculated over a reduced range for the methods used in this investigation are shown in Fig. 4.12. This reduced range of spring lengths is presented as the added-mass method was only applied to these springs due to the time required for testing. As seen in the previous section the dimensional models, including the finite-element model are in close agreement. The standard deviation of the spring constants calculated using the dimensional models was consistenly less than 1% even for relatively small spring aspect ratios (10:1). The dimensional models make the assumption that $L \gg w \gg t$ which breaks down as the aspect ratio decreases and causes the divergence between the static measurements and the dimensional models. Despite this, however, the standard deviation (with respect to the static results) settles below 4% for aspect ratios around 11:1 and even falls below 2% for aspect ratios

larger than 15:1. We are assuming that the static mass measurements are the best representation of the actual properties of the springs due to the simplicity of this technique. If we briefly consider the errors involved in the measurements we will see that this is a reasonable assumption. Firstly, the deflection measurement was corrected for the off-end laser position using the FEA results for the tip gradient and the off-end distance. For an off-end distance of $500\mu m$ this error was 8.0% for the shortest cantilever springs (10mm) and 3.5% for the longest (21.5mm). Once the tip deflection was determined the spring constant was calculated and corrected by a factor of $(1 - \Delta L/L)^3$ which can be simplified using the binomial theorem to get $1 - 3\Delta L/L$. This factor is not overly sensitive to ΔL and reduces the spring constant by 1.5% for a 10mm spring and by <1% for a 21.5mm spring, therefore, even if there were large errors in the position of the static mass the errors would be small. What is more, these errors were minimised because only the 3 longest springs were used for the force measurements so we can be confident that the static measurements are valid.

Measurements of the resonance frequency using LDV showed that the spectrum of the vibration amplitude response of one of the springs in an array could be used to identify the fundamental resonance frequencies of all of the other springs in the array which could save time when characterising a large number of springs. This effect was employed by Ghatnekar-Nilsson *et al* who measured the vibration amplitude frequency spectrum of a small array of silicon cantilevers fabricated by focused-ion-beam milling and measured the sensitivity of the fundamental resonance position to the mass load of the beams [68].

The dynamic techniques that require positioning masses on the reference springs are time consuming and difficult to implement, however, measuring the fundamental resonance frequency of the springs is relatively easy using LDV. For these reasons the dynamic added mass method was only applied to springs of length 13-18.5mm as shown in Fig. 4.12 (bottom). Clearly the dynamic methods

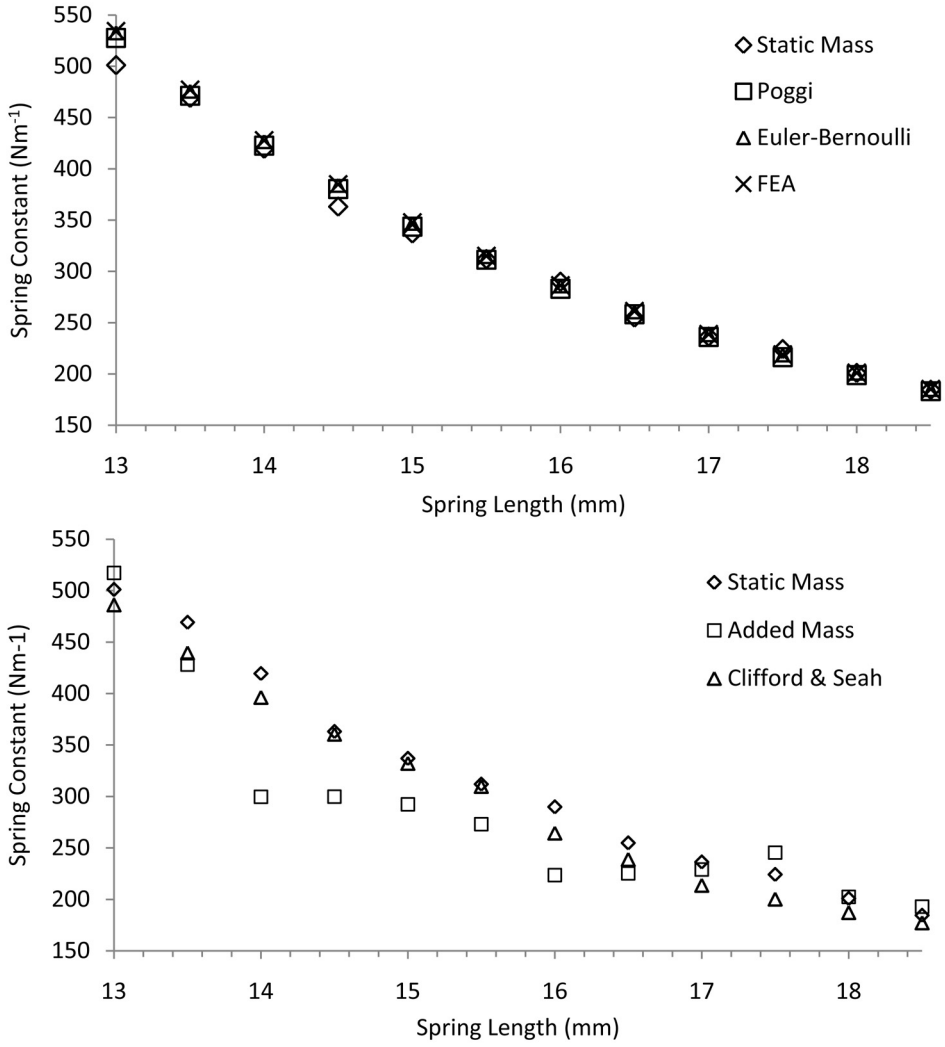

Fig. 4.12: A comparison of the calculated spring constants of the rectangular reference springs in the length range 13-18.5mm using dimensional models and static measurements (top) and dynamic methods (bottom).

show a larger variation in the calculated spring constant with a standard devitation of about 50%. The dynamic added mass results in particular show poor agreement with the static mass measurements which is a result of the many corrections and calculations that must be made in this technique. First of all the magnitude of the glass end mass was calculated based on optical measurements of their major and minor axes and on the assumption that they were ellispoidal in shape. The glass microspheres were often irregularly shaped with visible bubbles and surface deformities that would contribute to errors in the calculated mass. Also the density of the glass microspheres was relatively low in comparison to other materials such as tungsten microspheres which are often used for end-masses and would have produced larger changes in the resonance frequency. The mass sensitivity of the resonance frequency of a cantilever beam can be found from the expression for the fundamental frequency of a simple harmonic oscillator:

$$f = \frac{1}{2\pi}\sqrt{\frac{k}{m}} \tag{4.1}$$

where k is the spring constant of the cantilever and m is the mass of the beam. The differential is therefore

$$\frac{df}{dm} = \frac{1}{4\pi}\sqrt{\frac{k}{m^3}} \tag{4.2}$$

By substituting for m from equation 4.1 and rearranging we find:

$$\frac{df}{dm} = 2\pi^3\frac{f^3}{k} \tag{4.3}$$

The mass sensitivity is therefore proportional to f^3. As the mass of the beam can be written as $m = Lwt\rho$ it is clear from 4.2 that the mass sensitivity increases as the dimensions (and therefore the mass) of the beam decreases and springs with small spring constants will show larger changes in resonance frequency. Therefore if dynamic calbration methods are used to determine the spring constant then the mass sensitivity is limited by the dimensions of the cantilever.

As described previously, the axial position of the end masses is also crucial and

must be accurately measured so that the effective end-mass can be found. Another factor that may have contributed to the errors in the added mass method was the way that the masses were secured to the spring. A small amount of petroleum jelly was used to "stick" the mass to the spring, however it is unknown whether the mass of this jelly or its viscous properties will also contribute to changes in the measured resonance frequency of the loaded spring. This way of securing the masses to the spring is far more convenient for the dynamic added mass method than sintering the mass to the spring as it is relatively easy to change the added mass and does not require high temperatures which will form surface oxides that may affect the springs mechanical properties.

The small forces generated by the actuators necessitated the use of the longer reference springs to generate an adequate deflection. On one hand this is beneficial as for longer springs (higher aspect ratio) the dimensional and static methods show better agreement and the errors associated with off-end loading are reduced. As the spring constant falls, however, the resonance frequency also decreases and as there is a $1/f$ noise contribution when using laser-Doppler-vibrometry, the measurements are more prone to noise. This may not be a problem when determining the resonance frequency by externally driving the reference spring, however, as the spring constant decreases the techniques that use the thermal oscillations of the spring (Sader method and thermal tuning) become more appealling and these will suffer more from this noise contribution.

Considering the time taken to implement the added-mass method and the uncertainties in the results it is clear that this method is not the best choice of calibration technique. It may be possible to improve the accuracy of this method by further experimentation, however, the simplicity and accuracy of both the dimensional and static methods make them a better choice for quick and accurate spring calibration.

It should be remembered that the dimensional models were formulated for

cantilever shaped reference springs. For other spring geometries these models will not apply and finite-element models must be more heavily relied upon. Even the relatively simple V-shaped spring design results in a considerable increase in complexity and difficulty in finding an analytical solution for the spring constant and deflection profile. In this situation the static mass method and even the dynamic added mass method may be preferable as they make no assumptions about the geometry of the spring.

4.2 Actuator Perfomance - Static

4.2.1 Deflection Measurements

The bimorph actuator consists of two piezoelectric layers that can be made to contract or expand in the plane of the layer by applying a voltage across the layer. If the layers are actuated individually then the actuator is a *unimorph* where the layer that is not actuated acts as a restricting elastic layer. Assuming that both of the piezoelectric layers have the same piezoelectric and elastic properties we would expect that the response of each of the layers would be similar. By examining the deflection response of each individual layer we can determine whether the poling conditions are optimised. The static deflection response of a series poled ($2v/\mu m$, $120°C$) $2mm \times 3.75mm$ actuator is shown in Fig. 4.13. The measurements were made with the laser spot of the triangulation deflection sensor $200\mu m$ from the very edge of the bimorph. The top and middle figures show the deflection response of the actuator when only the bottom and top layers (respectively) are actuated. The responses of the individual layers are dependent on both the poling conditions and the actuation conditions. During poling the bottom electrode is grounded and the poling potential is applied to the top electrode (the middle electrode is ignored) whereas during actuation the middle electrode is grounded and the actuation potential is applied to both the top and the bottom electrodes. For this reason, the applied electrical field is always antiparallel to the poling direction in one of the piezoelectric layers, the layer that is affected changes as the actuation potential changes its polarity.

In Fig. 4.13 the electric field in the bottom layer (top) is antiparallel to its poling field when the applied voltage is positive and when the applied voltage is negative then this situation applies to the top layer (middle). The hysteresis is more asymmetric in the bottom layer with a larger reversal in deflection direction which indicates that there is more domain switching in the bottom ceramic layer than in

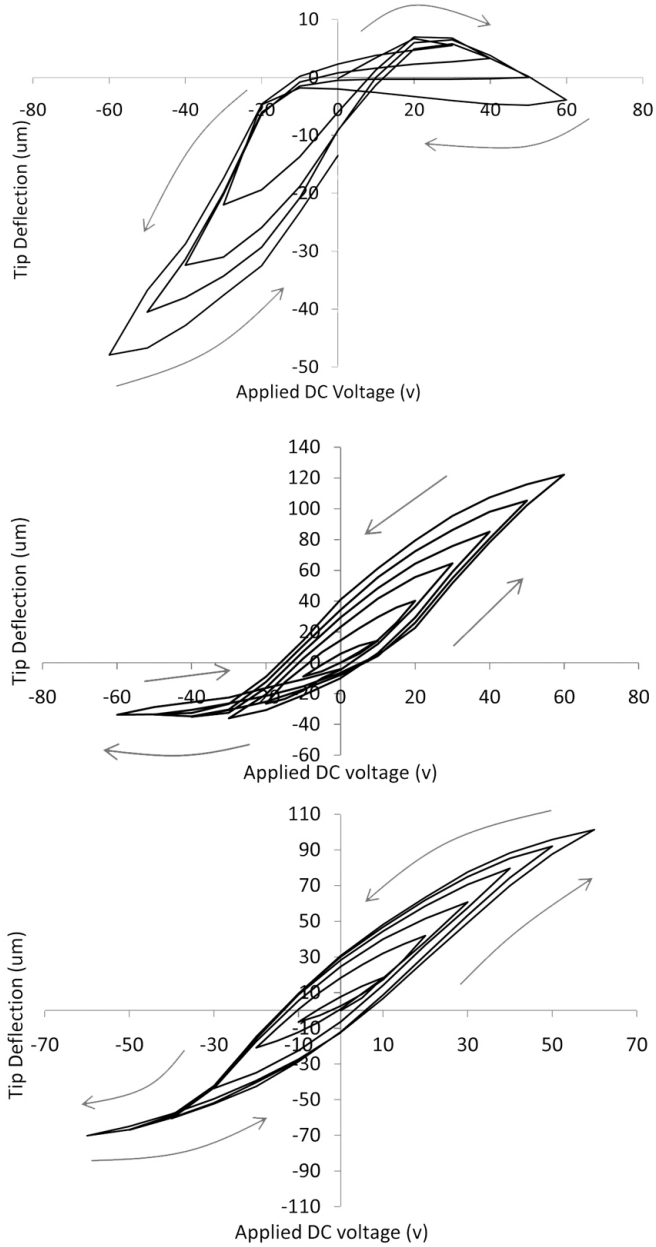

Fig. 4.13: The tip deflection of a $3.75 \times 2mm$ bimorph actuator with applied DC voltage. The active layers of the bimorph were actuated separately - bottom layer only (top), top layer (middle) and both layers (bottom).

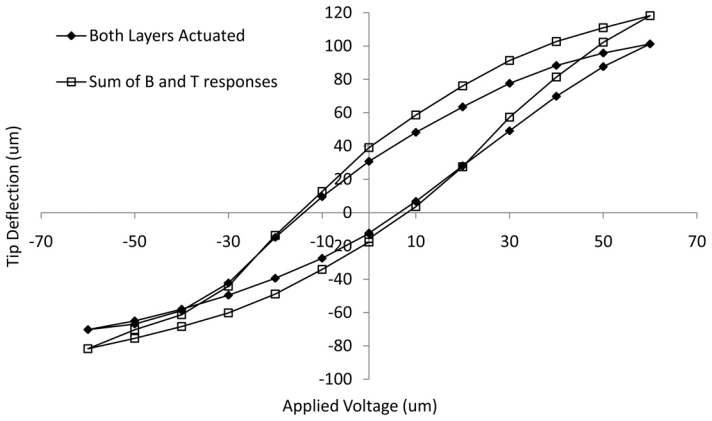

Fig. 4.14: The tip deflection of a bimorph can be considered as the superposition of the deflection generated by each layer separately ($3.75 \times 2mm$ bimorph).

the top layer which is likely a result of a nonuniform electric field through the thickness of the bimorph. This change in the direction of the tip deflection well illustrates the change in mode of operation from the d_{31} mode to the d_{33} mode as the polarisation of the domains switches under the influence of the applied electric field (see section 2.1.2 for a description of this effect). One way to prevent domain switching from reducing the tip deflection during actuation is to use a simple potential divider circuit to control the electric field of the layer that displays more domain switching. The values of the resistors in the potential divider should be chosen so that the maximum applied field does not exceed the value at which switching is observed to occur. For example, for the actuator in Fig. 4.13 if the applied field is parallel to the direction of the polarisation then a voltage of 60V can be applied, however, if the field direction is antiparallel to the polarisation direction then only 20V can be applied before switching starts to reduce the tip deflection.

The displacement of a bimorph can be described as the superposition of the individual response of each layer [69]. This is illustrated by Fig. 4.14 which compares the sum of the deflection responses of the individual layers to the

deflection response when both layers are actuated simultaneously. The shape of the deflection hysteresis curves are closely matched though the difference between them increases with applied voltage. This is likely because the field is antiparallel to the poling of one of the layers and this layer is no longer a passive elastic layer as in the case when only one layer is actuated (the tip deflection of a $1.2mm \times 3.75mm$, $1.6 \times 3.5mm$ and a $1.4mm \times 2mm$ actuator are presented in Appendix E). A useful observation was made by Li *et al* who found that the dielectric constant as found from polarisation hysteresis ($\epsilon = dP/dE$) was asymmetric. As the electric displacement is constant in the top and bottom ceramic layers and given by $D_3 = E_3^T \epsilon_{33}^T = E_3^B \epsilon_{33}^B$ (Li ignored the polarisation caused by stress as it was calculated to be only 7% of the polarisation generated by the electric field) an asymmetric dielectric constant will result in asymmetric electric fields experienced by the ceramic layers. Even if the total applied field is larger than the coercive field E_C (the field required for $P = 0$) the redistribution of the field caused by the asymmetric dielectric constant would reduce the field below E_C and hence affect the response of the actuator. Unfortunately, the polarisation hysteresis was not investigated due to the limitations of the equipment so we can not say for certain if this effect applies here, however it seems likely.

The bimorph actuators are prestressed due to the different coefficients of thermal expansion of the elastic and ceramic layers. The internal stress of a piezoelectric actuator affects its electro-mechanical properties as domain switching can be caused by mechanical stresses as well as by minimising the electrostatic energy of the domains in an external field. As described in section 2.1 the unit cell of a Perovskite material is tetragonal below its Curie temperature and is asymmetric. Changes in the orientation of the polarisation domains in response to stresses within the ceramic (to minimise its total energy) result in changes in mechanical strain. These changes in internal stress of the actuator will affect its mechanical stiffness. A simple way to observe how the mechanical stiffness of an actuator changes with its internal state is to measure its resonance frequency which is

directly dependent on the actuator's stiffness constant. An external voltage was applied as in the deflection measurements and the vibration deflection spectra of the actuator was found using laser-Doppler-vibrometry. The change in resonance frequency of a $1.6 \times 3.75mm$ bimorph (series poled, $2v/\mu m$) with applied DC voltage is given in Fig. 4.15. For positive applied voltages the resonance frequency, and hence the mechanical stiffness of the actuator, tends to decrease, whereas negative applied voltages increase the mechanical stiffness. Negative applied voltages have a larger effect on the stiffness as the resonance frequency increases by around 200Hz whereas positive voltages change the resonance frequency by only around 20Hz (note the difference in scale). It is interesting to note that for positive voltages the resonance frequency shows a minima around 40V before increasing again, whereas negative voltages only produce an increase in resonance frequency. According to equation 2.34 the spring constant of a cantilever beam with a uniform cross-section is proportional to f_0^3. We can use this information to estimate the *change* in spring constant that is indicated by the change in resonance frequency of the bimorph. Using this assumption we calculate that the spring constant changes by about 4% and 25% for positive and negative voltages respectively.

To investigate the effect of the poling conditions two $1.6 \times 3.75mm$ bimorphs were series and parallel poled at $2v/\mu m$ and at $2.5v/\mu m$. Poling fields higher than $2.5v/\mu m$ caused sparking during the poling process which severely damages the actuators and fields smaller than $2.0v/\mu m$ produced actuators with very poor displacement characteristics. Fig.4.16 shows the tip displacement of the series (top) and parallel (middle) poled actuators. The deflection generated by the individual layers are shown along with the tip deflection when the voltage is applied to both layers (bottom). The "butterfly loop" of the bottom ceramic layer of the series poled device indicates more domain switching than in the top layer which may indicate that the bottom layer is experiencing a larger electric field caused by an asymmetric dielectric constant as described earlier. This would indicate a smaller dielectric constant for fields applied antiparallel to the poling

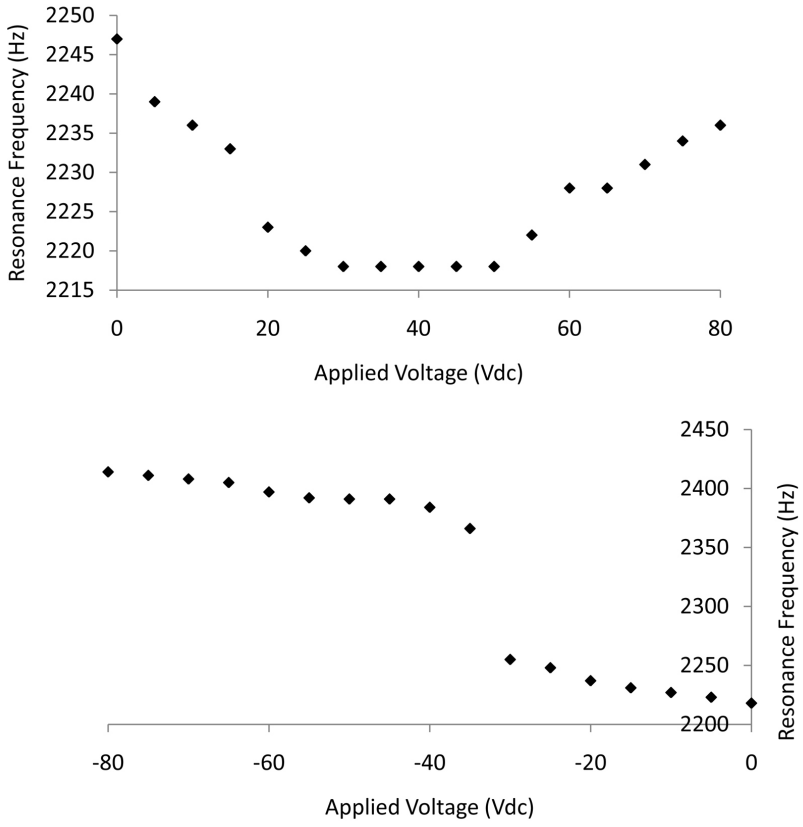

Fig. 4.15: The change in resonance frequency of a $1.6 \times 3.75mm$ actuator as a DC voltgage is applied.

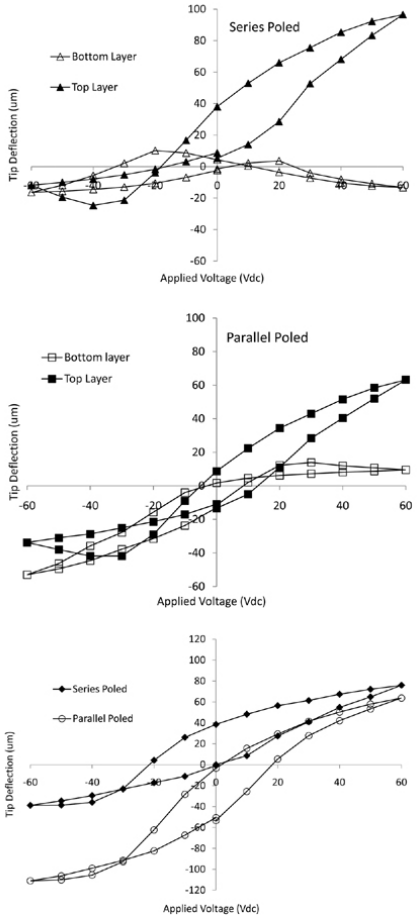

Fig. 4.16: The deflection of a $1.6 \times 3.75mm$ cantilever series and parallel poled at $2v\mu m^{-1}$. The PZT layers were actuated separately (top, middle) and then together (bottom).

direction (negative voltage). As we would expect in a parallel poled device where the voltage drop across each ceramic layer is the same, the behaviour of the top and bottom layers is similar though inverted due to the relative polarity of the applied field to the poling direction of each layer. Even the maximum tip deflection is almost the same for the top and bottom layers in the parallel poled device. It should be noted that vertical position of the hysteresis loops is dependent on the actuation history of the device, generally the measurements were taken in three loops, first the deflection generated by the bottom layer, then the top layer then both layers together, hence some loops do not start at (0,0).

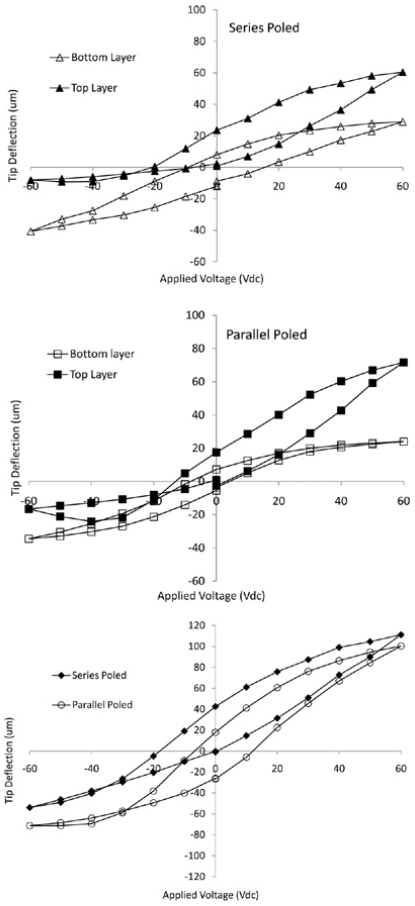

Fig. 4.17: The deflection of a $1.6 \times 3.75mm$ cantilever series and parallel poled at $2.5v\mu m^{-1}$. The PZT layers were actuated separately (top, middle) and then together (bottom).

Similar trends are seen in the behaviour of the top and bottom layers of the device poled at $2.5v/\mu m$ though the difference in the shape of the hysteresis loops for the top and bottom layers of the series device is smaller (Fig. 4.17). It appears that domain switching is not occuring in the bottom layer to the same extent as in the series poled device. This suggests that the applied field is unable to generate the domain switching seen in the device poled in a lower field. This may simply be due to natural variations in the ceramic or perhaps the difference between the poling fields is too small to be conclusive. Generally speaking, as the poling field is increased the remanent polarisation and coercive field saturate which indicates the optimum poling field [70]. The data presented here is inconclusive though we would expect the optimum field to be $2 - 3v/\mu m$.

4.2.2 Force-Displacement Measurements

The force measurements were made by bringing the tip of an actuator into contact with a cantilever reference spring with a known spring constant. When a voltage is applied to the actuator the spring deflects an amount that is directly proportional to the force applied by the actuator. As described in section 2.2.5 corrections must be made to first of all determine the tip deflection of the spring and then to compensate for the off-end point of contact between the actuator and the reference spring. Detail of the relative positions of the actuator and the reference spring for positive force measurements is given in Fig. 4.18 which shows how the point of contact between the actuator and the reference spring is the sum of the off-end distances of the reference spring and the actuator.

To determine the tip force generated by the bimorph in both positive and negative directions the reference spring must be positioned both above and beneath the actuator. The laser triangulation sensor was fixed which meant that the laser spot was incident on the reference spring when measuring forces in the positive (up) direction, and then incident on the bimorph when measuring forces in the negative

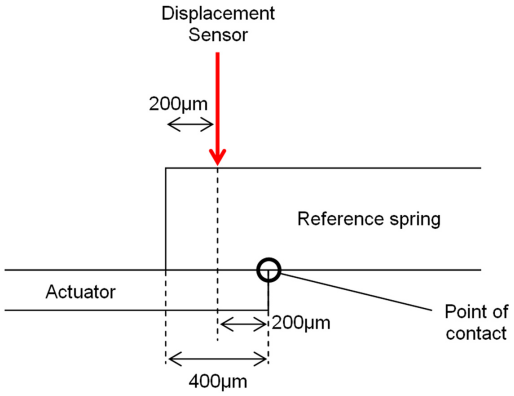

Fig. 4.18: Detail of the relative positions of the actuator and reference spring during force measurements.

direction (down). This needs to be taken into consideration when making corrections for the off-end position of the laser sensor because the deflection at the tip of the reference spring (or bimorph) is calculated from the local curvature and the off-end distance. The curvature at the tip of the reference springs was found from a finite-element model (see Fig. 4.6) and the tip curvature of the actuators was found using the analytical expression for bimorph deflection formulated by Wang and Cross. Fig. 4.19 shows the deflection correction for a given measured deflection calculated for a $2 \times 3.75mm$ actuator for a $200\mu m$ off-end distance. The dependence of the deflection correction is linear and is around 10% of the measured value. By repeating this process for actuators with different dimensions the deflection correction as a percentage of the measured deflection can be calculated. The tip deflection correction (%) as a function of the bimorph length (it is unaffected by bimorph width) for a $200\mu m$ off-end distance is presented in Fig. 4.20. This plot shows that the deflection correction can be as high as 45% for bimorphs around 1mm in length which is not surprising as the off-end distance is 20% of its length. Shorter actuators will also generate smaller forces/deflections which will be subject to the limitations of this measurement technique, however, the force generated by small actuators will likely fall in the range of commercially available force sensors.

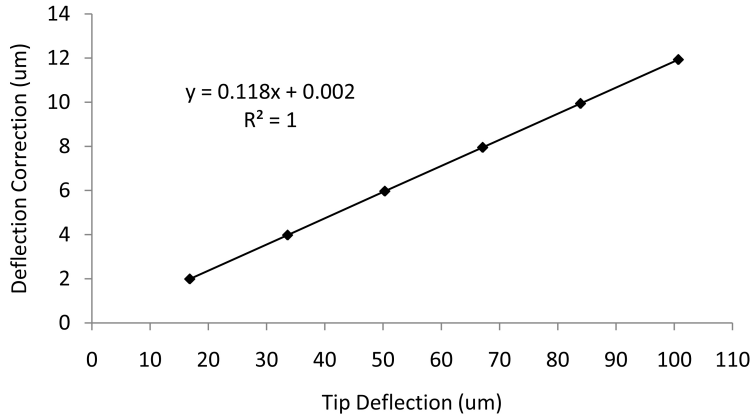

Fig. 4.19: Deflection corrections for a $2 \times 3.75mm$ bimorph actuator and off-end distance of $200\mu m$.

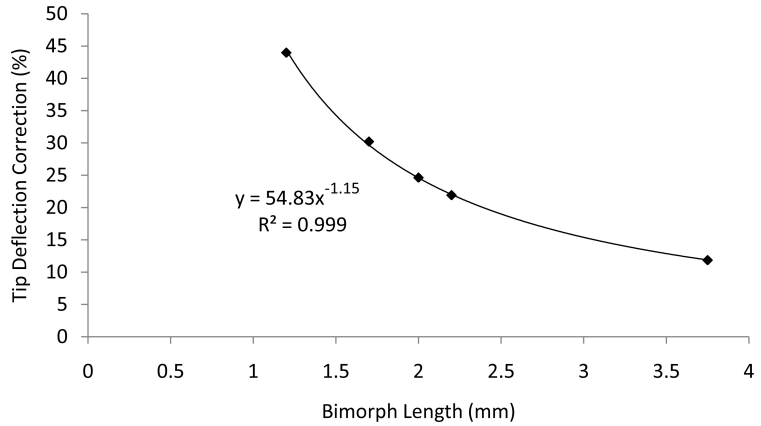

Fig. 4.20: The deflection corrections for the bimorph actuators used in this work.

Actuator Dimensions and Poling Conditions			***Mean Force (mN)***		
$w \times L \times d(mm)$	Poling Field $(V/\mu m)$	Configuration	+60V	-60V	$\pm$
$1.6 \times 3.75 \times 0.09$	2.5	Series	5.4	4.3	0.4
$1.6 \times 3.75 \times 0.09$	2.5	Parallel	6.4	2.8	0.4
$1.6 \times 3.75 \times 0.09$	2.0	Series	7.4	4.4	0.4
$1.6 \times 3.75 \times 0.09$	2.0	Parallel	4.6	4.1	0.4
$2.0 \times 3.75 \times 0.09$	2.0	Series	8.1	4.5	0.5
$1.4 \times 2.0 \times 0.09$	2.0	Series	1.1	1.6	0.1
$1.4 \times 1.2 \times 0.09$	2.0	Series	1.8	0.2	0.1
$1.4 \times 1.7 \times 0.09$	2.0	Series	1.6	0.2	0.1
$1.4 \times 2.2 \times 0.09$	2.0	Series	2.8	0.5	0.2

Table 4.2: The tip force generated by the bimorph actuators

The tip force measurements for the cantilever bimorph actuators are presented in Table 4.2. There is a clear asymmetry to the forces generated by the actuators which fall short of the predictions by the Wang and Cross model (for example the model predicts that a $1.6 \times 3.75mm$ bimorph will generate deflections of around $40\mu m$ and a tip force of 20mN). This asymmetry was expected in light of the asymmetry of the deflection measurements and the hysteresis seen in the responses of the individual ceramic layers.

The force capabilities of an actuator are often presented in a plot of Force vs Deflection as illustrated in Fig. 4.21. The *blocking force* is the tip force point when $\delta = 0$ and the free deflection is found when $F = 0$. The F vs δ plot for a $2 \times 3.75mm$ actuator is presented in Fig. 4.22. The datapoints on the x-axis correspond with the deflection of a free actuator and the other points corresepond to the deflection of the actuator when coupled to three silicon reference springs (springs 23, 21 and 19) and the resulting tip forces calculated in the previous section. To obtain a data over a larger range of deflections it would have been more instructive to use reference springs with larger spring constants, however, this would have meant that the corrected force and deflection measurements would have contained larger errors.

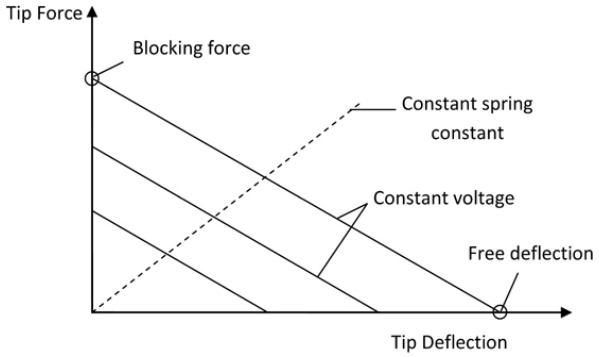

Fig. 4.21: An ideal plot of *Tip Force vs Tip Deflection* of a bending actuator.

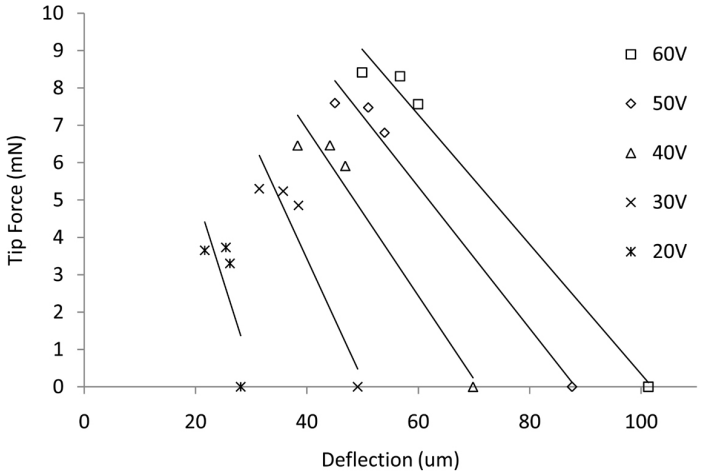

Fig. 4.22: The force-deflection plot of a $2 \times 3.75mm$ actuator. The points on the x-axis correspond to the free deflection of the actuator.

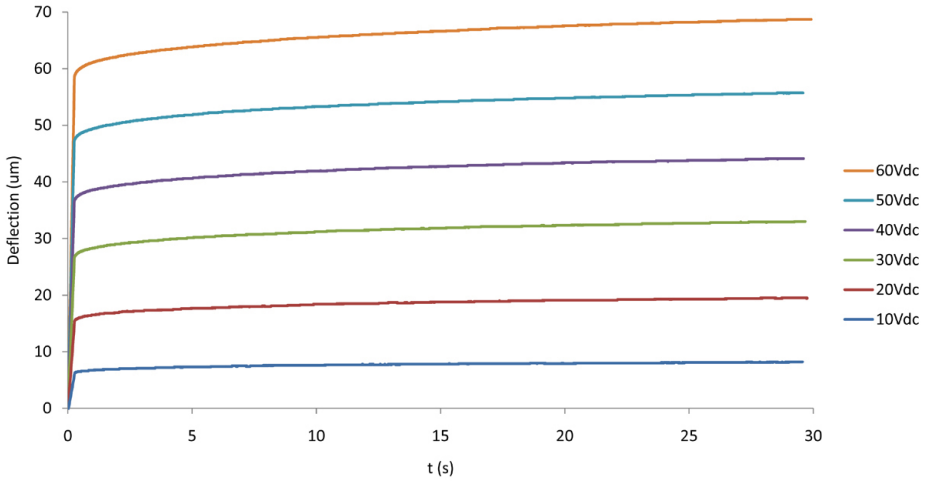

Fig. 4.23: Deflection creep of a $2 \times 3.75mm$ actuator.

4.2.3 Creep & Relaxation

An unfortunate result of domain switching within a piezoelectric material is that the strain changes over time resulting in *creep*. This creep is dependent on a variety of factors such as material properties and temperature. In the case of piezoelectric bending actuators it manifests itself as a time dependent increase in tip deflection after an electric field is applied. Creep is of great interest when piezoelectric devices are used for micropositioning and micromanipulation where the control signals depend on the current position of an actuator. By understanding the creep behaviour it is possible to use adaptive software or electronics to eliminate or minimise the effect.

The tip creep of a $2 \times 3.75mm$ actuator was investigated by applying a DC voltage and measuring the time dependence of the tip deflection using the Keyence sensor to sample at a user defined frequency. Fig. 4.23 shows the tip deflection for DC voltages of 10-60V (note that the time-deflection curves have been shifted along the x-axis so that they can be compared). After a region where the bimorph deflection increases linearly (lasting around 0.25s) the deflection increases much more slowly

as domain switching within the ceramic layers contributes to the strain, this is known as Andrade creep and can be described using the well known equation [71]:

$$\delta = \delta_0 + \beta t^{1/3} \tag{4.4}$$

where δ is the tip deflection (a function of strain), δ_0 is the deflection after 0.25s, β is a constant that scales the magnitude of the creep and the exponent (1/3) scales the rate of saturation of the creep mechanism. The δ_0 and β parameters were found from the deflection data and optimised by using the least-squares method (i.e. by minimising the sum of the square of the difference between the deflection data and the Andrade equation). An example of this is seen in Fig. 4.24 where the Andrade model is fit to the tip deflection data for an applied voltage of 60V and the parameters $\delta_0 = 67.8$ and $\beta = 3.5906$. The parameters for applied voltages of 10-60V increase linearly with voltage as shown in Fig. 4.25. The exponent can also be fitted to the data though it was kept constant at 1/3, a brief investigation where the exponent was also optimised to fit the data showed that the exponent varied from 0.330-0.334 though no trend was seen. The relaxation of the actuator after the applied voltage is removed is shown in Fig. 4.26. Unlike some bimorph devices that oscillate like a tuning fork after a voltage pulse the bimorph here appears to be overdamped likely due to the thickness of the device and the internal stresses.

4.2.4 The Effective Transverse Piezoelectric Coefficient

An important parameter for evaluating piezoelectric films in a bending device is the piezoelectric coefficient e_{31} as the bending is principally caused by the longitudinal deformation under the application of a transverse field. A common way of determining the e_{31} parameter for piezoelectric thin films is to measure the charge generated when the film is strained [72]. The effective transverse piezoelectric coefficient e_{31} is defined as :

$$e_{31} = \frac{d_{31}}{s_{11}^E + s_{12}^E} \approx \frac{d_{31}}{s_{11}^E} \tag{4.5}$$

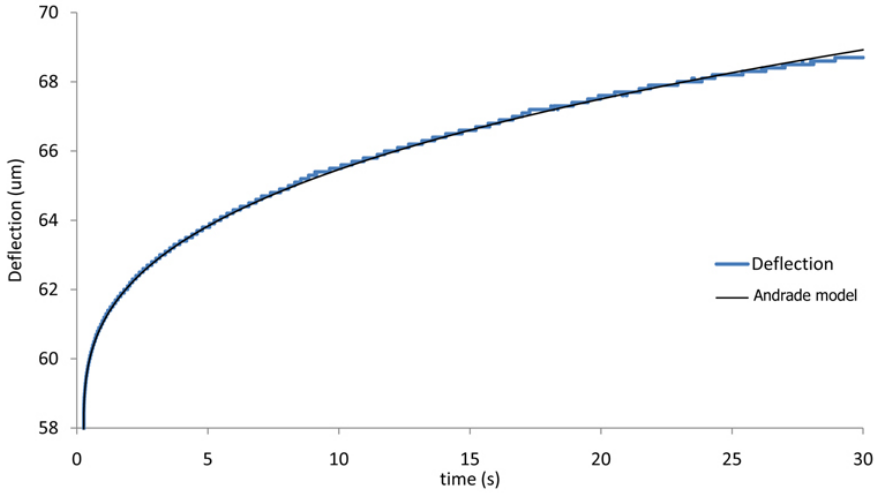

Fig. 4.24: Deflection creep of a $2 \times 3.75mm$ actuator is well described by the Andrade model.

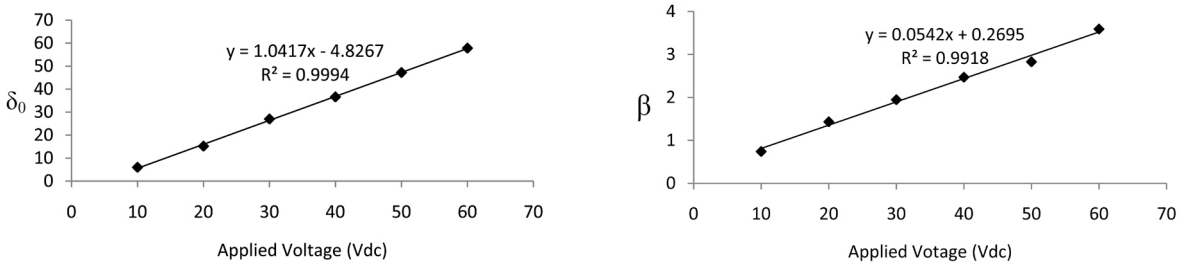

Fig. 4.25: Andrade model parameters δ_0 and β.

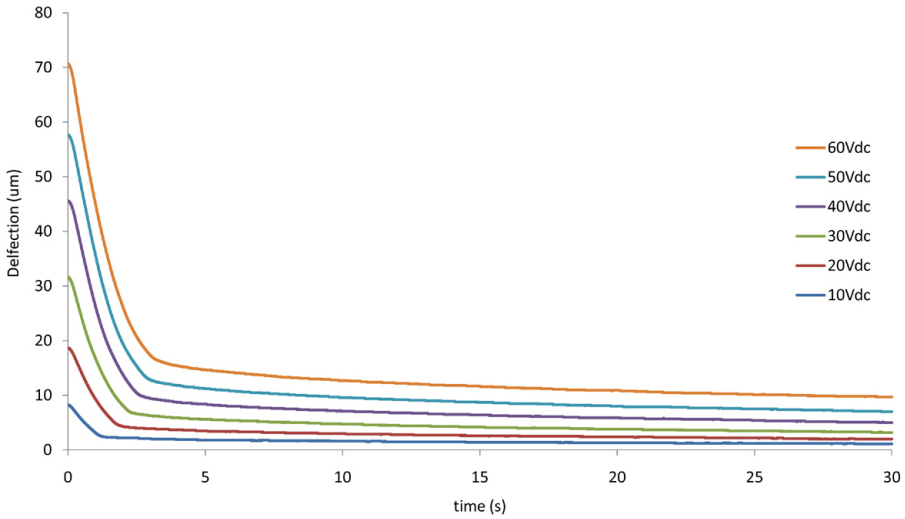

Fig. 4.26: Relaxation of a $2 \times 3.75mm$ actuator after static actuation.

which can be simplified because the strain in the 1 direction will be larger than in 2 due to the geometry of the actuator. A simple method of determining the transverse constant was described by Kanno *et al* who calculated e_{31} of thin PZT films ($2.5\mu m$) deposited on different substrates (MgO, Si) from the tip deflection response of cantilever structures ($\sim 15 \times 2.5mm$) [73]. The coefficient d_{31} was calculated from an analytical expression for the deflection of a *unimorph* and the elastic compliance s_{11} of the cantilever was estimated from the Young's moduli of the cantilever materials. This approach can also be applied to estimate the e_{31} of the thick PZT films used in this work. The devices used here are bimorphs, however, when only one layer is actuated the other ceramic layer and the shim can be treated as a composite elastic layer. To treat the bimorph as a unimorph the top ceramic layer of the bimorph is treated as the active layer of the unimorph and the bottom ceramic layer and shim act as the substrate. Kanno used the expression for the deflection of a unimorph actuator formulated by Smits and Choi [74]:

$$\delta = -V \frac{3 d_{31} s_{11}^s s_{11}^p h^s (h^s + h^p) L^2}{K} \tag{4.6}$$

where

$$K = (s_{11}^s)^2(h^p)^4 + 4s_{11}^s s_{11}^p h^s (h^p)^3 + 6s_{11}^s s_{11}^p (h^s)^2 (h^p)^2 + 4s_{11}^s s_{11}^p h^p (h^s)^3 + (s_{11}^p)^2 (h^s)^4 \tag{4.7}$$

The superscripts s and p refer to the substrate and the piezoelectric layer respectively, L and h are the unimorph length and thickness, V the applied voltage, d_{31} the transverse piezoelectric coefficient and s_{11} is the compliance. This expression can be rearranged for d_{31} and inserted into equation 4.5 to give:

$$e_{31} = \frac{d_{31}}{s_{11}^p} = -\delta \frac{X^2(h^p)^4 + 4Xh^s(h^p)^3 + 6X(h^s)^2(h^p)^2 + 4Xh^p(h^s)^3 + (h^s)^4}{3s_{11}^s h^s (h^s + h^p) L^2 V} \tag{4.8}$$

where X=s_{11}^s/s_{11}^p. The compliance is given by the reciprocal of the Young's modulus which can be estimated for the shim-ceramic substrate by scaling according to the thickness of each layer. The Young's moduli for the titanium shim and the ceramic material are 115GPa and 66GPa respectively. As the peizoelectric thin film tested by Kanno was very thin compared to the substrate, the expression for e_{31} could be simplified to remove s_{11}^p from the equation. This is useful because the elastic compliance of a thin film is not necessarily the same as bulk material. In our case, however, the piezoelectric layers and the elastic shim are of a similar thickness so such a simplification is not possible. It is possible, however, to estimate the Young's modulus of the shim-ceramic substrate by simply scaling the Young's modulus with the thickness of that layer:

$$E_{eff} = E_{Ti}\left(\frac{t_{Ti}}{t_{Ti} + t_{PZT}}\right) + E_{PZT}\left(\frac{t_{PZT}}{t_{Ti} + t_{PZT}}\right) \tag{4.9}$$

where E_{eff} is the effective Young's modulus of the bilayer. The e_{31} calculations were made using the tip displacement generated by the actuator when the ceramic layers were individually actuated. Fig.4.27 shows the results of the e_{31} calculation for the bottom and top ceramic layers. The magnitude of e_{31} varies for both layers but in particular e_{31} of the top PZT layer reflects the non-linear tip deflection indicating that domain switching contributes considerably to the transverse

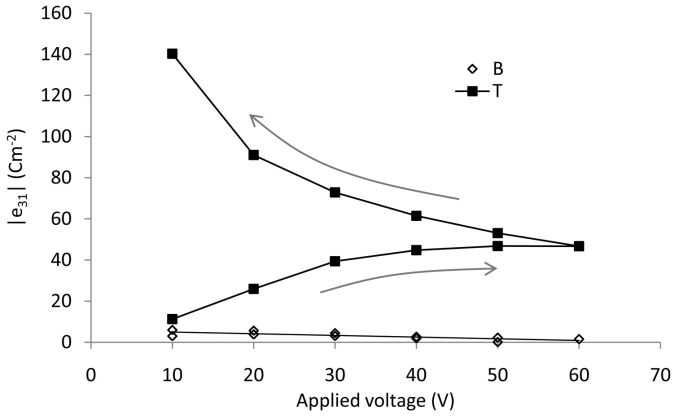

Fig. 4.27: The effective transverse piezoelectric coefficient e_{31} found from the tip deflection of a $2 \times 3.75mm$ actuator.

piezoelelctric coefficient of the film.

4.2.5 Overview - Static Performance

It is useful at this point to compare the measured deflection and tip force of our actuator with the predictions of the Wang and Cross model (WC) and some other bending actuators currently available on the market. Table 4.3 compares the deflection and tip force predicted by the WC model with the experimentally measured values. The WC model predicts the same deflection for both ± 60V the only difference being the direction of the deflection. On the other hand the measured values of force and deflection generated by our pre-stressed bimorph can vary considerably depending on the polarity of the applied voltage. Generally, the forces and deflections generated by positive voltages exceed those generated by negative voltages which is attributed to the prestress of actuators which is not accounted for in the WC model. In the force measurements of the actuators it was observed that the tip force tends to level off when the applied voltage exceeds -40V. One way of comparing the WC model and the experimental measurements is to use the ratio of deflection/tip force. Table 4.4 compares the WC and the experimental results. The magnitude of δ/F for the actuators is consistently one

Dimensions(mm)	***Wang & Cross model***		***Experiment*** $\delta(\mu m)$		**F(mN)**	
$L \times w$	$\delta(\mu m)$	***F(mN)***	+60V	-60V	+60V	-60V
1.2×1.4	4.5	40.7	9.1	-2.3	1.8	0.2
1.7×1.4	9.1	28.7	15.2	-2.4	1.6	0.2
2×1.4	12.6	24.4	13.0	-12.7	1.1	1.6
2.2×1.4	15.3	15.3	22.2	-5.5	2.8	0.5
3.75×1.6 S	44.3	14.9	75.9	-38.9	7.4	4.4
3.75×1.6 P	44.3	14.9	63.7	-111	4.6	4.1
3.75×2	44.3	18.6	101.3	-70.2	8.1	4.5

Table 4.3: A comparison of the Wang Cross bimorph model with measured deflections and tip force. P and S refer to series and parallel poled actuators.

order of magnitude larger than the CW predictions, mainly due to the larger observed deflections.

There are a variety of piezoelectric bending actuators on the market. Generally, they are much larger and thicker than those used in this work as they are fabricated using bottom up techniques such as screen printing. A summary of the capabilities of some of these actuators is presented in Table 4.5. Due to the variety of dimensions of these actuators the data is presented in the form of deflection (or force) per unit volume, further details of these actuators such as their operating voltages and dimensions are presented in Appendix G. While the force generated per unit volume is about average for these type of actuators the deflection per unit volume of Cranfield's bimorph far exceeds that of its contemporaries. Other devices may generate larger tip deflections and forces, however, the relatively large dimensions of these devices and their operating voltages certainly limit their use in the MEMS field.

Dimensions(mm)	***Deflection/Force***	
$L \times w$	***W & C model***	***Experiment***
1.2×1.4	0.11	5.1
1.7×1.4	0.32	9.5
2×1.4	0.52	11.8
2.2×1.4	0.69	8.8
3.75×1.6 S	2.97	10.3
3.75×1.6 P	2.97	13.9
3.75×2	2.38	12.5

Table 4.4: A comparison of the ratio δ/F for the measured devices and the Wang & Cross model.

Manufacturer	***Device***	δ/vol $(\mu m/mm^3)$	F/vol (N/mm^3)
Noliac [75]	CMBP07	4.7	0.001
Steminc [76]	SMBTA352D2T07M	26.5	0.002
Mide [77]	QP20n	0.001	0.0004
Physik Instrumente [78]	PL112.10	1.1	0.027
Face Int. [79]	PAB-4010	2.3	0.002
Face Int. [80]	TH-10R	0.5	0.047
Cranfield's Bimorph	$2 \times 3.75mm$	150	0.012

Table 4.5: A comparison of the force per unit volume and the deflection per unit volume of some commercially available bimorph actuators.

4.3 Actuator Performance - Dynamic

The dynamic deflection response of a bimorph piezoelectric actuator is generally only strongly affected around its resonance frequencies. Fig. 4.28 shows the frequency dependent tip velocity of an actuator with dimensions $1.6 \times 69.98 \times 0.62mm$ [81]. This is a typical response and has been reported elsewhere for bimorph actuators with varying dimensions and thicknesses [82, 83, 84]. The dynamic response of the actuators used in this investigation, however, showed a considerably different response. The dynamic response of a $2 \times 3.75 \times 0.09mm$ actuator ($2v/\mu m$, series poled) from 0-1000Hz and 10-60Vac is presented in Fig. 4.30 for a sinusoidal applied voltage and in Fig. 4.31 for a square-wave applied voltage. The data was acquired by measuring the actuator oscillation in response to Vac (50kHz sampling frequency) and then finding the maximum positive and negative deflection amplitudes. The response of the actuator to a sinusoidal or square-wave supply shows the same frequency dependence though the amplitude of the actuator oscillations is slightly reduced for a square-wave supply. At low frequencies (25-150Hz) the oscillation amplitude is roughly constant when using a square-wave supply which may be important for some applications.

The resonance frequency of this actuator is around 1.9kHz as seen from its vibration amplitude spectra in Fig. 4.29. The actuator was part of of an array of three devices which is why there are two smaller peaks to the right of the main resonance peak. The dynamic amplitude response of the actuator was not investigated above 1kHz due to the limits of the amplifier used, however, it is clear that there is strong frequency dependence even at these relatively low frequencies. The amplitude of oscillations quickly falls to zero at 200Hz and then oscillates as the frequency of actuation is increased further. The dynamic response of actuators with dimensions $1.6 \times 3.75 \times 0.09mm$ and $1.4 \times 2.0 \times 0.09mm$ are also shown in Fig. 4.33. In these figures the amplitude of oscillation also falls to zero at 200Hz,

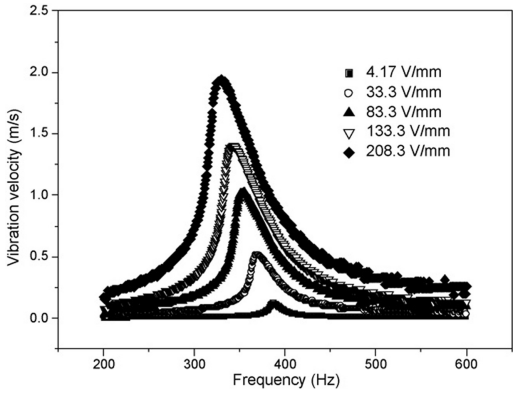

Fig. 4.28: The dependence of tip velocity of a bimorph actuator as a function of actuation voltage [81]

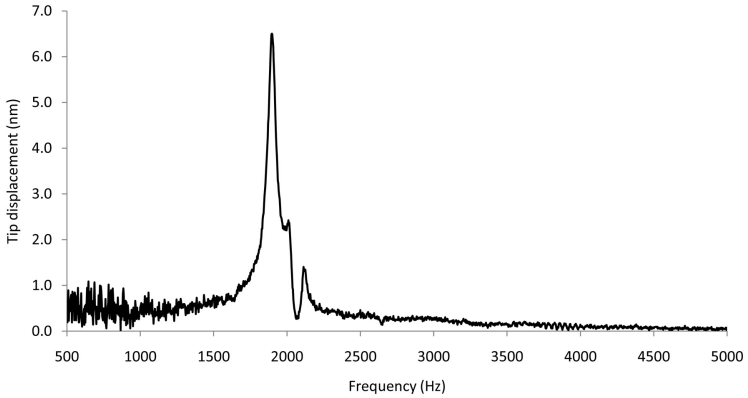

Fig. 4.29: The resonance spectrum of a $2 \times 3.75mm$ actuator found using LDV.

400Hz and 600Hz. This frequency dependency of the deflection response is not observed for the bimorph actuators investigated by Li, Smits, Wood and Kursu which may be because the ceramic layers in their devices are considerably thicker than in the devices used in this investigation.

To investigate the bimorph shape during dynamic actuation the laser displacement sensor was moved along the beam's longitudinal axis during actuation and the displacement of the bimorph was measured every $500\mu m$ (starting $200\mu m$ from the tip). The sampling frequency was 50kHz ($20\mu s$) to ensure that no aliasing effects

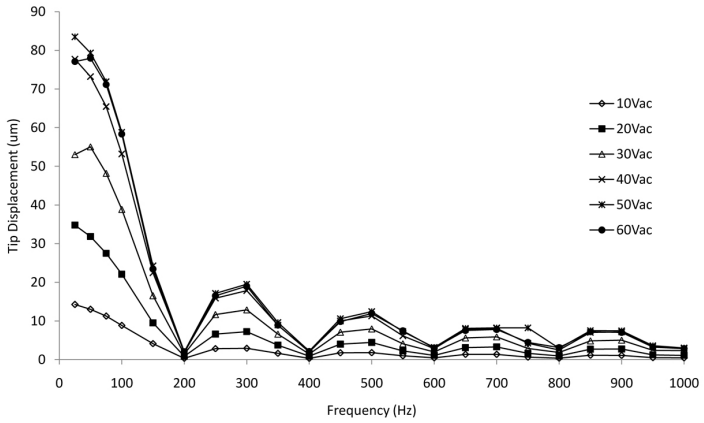

Fig. 4.30: The dynamic deflection response of a $2 \times 3.75mm$ with a sinusoidal source and Vac=10-60V.

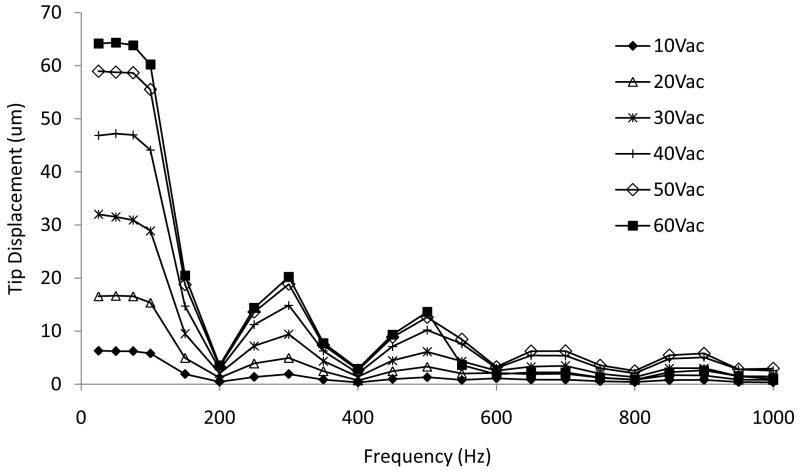

Fig. 4.31: The dynamic deflection response of a $2 \times 3.75mm$ with a square-wave source and Vac=10-60V.

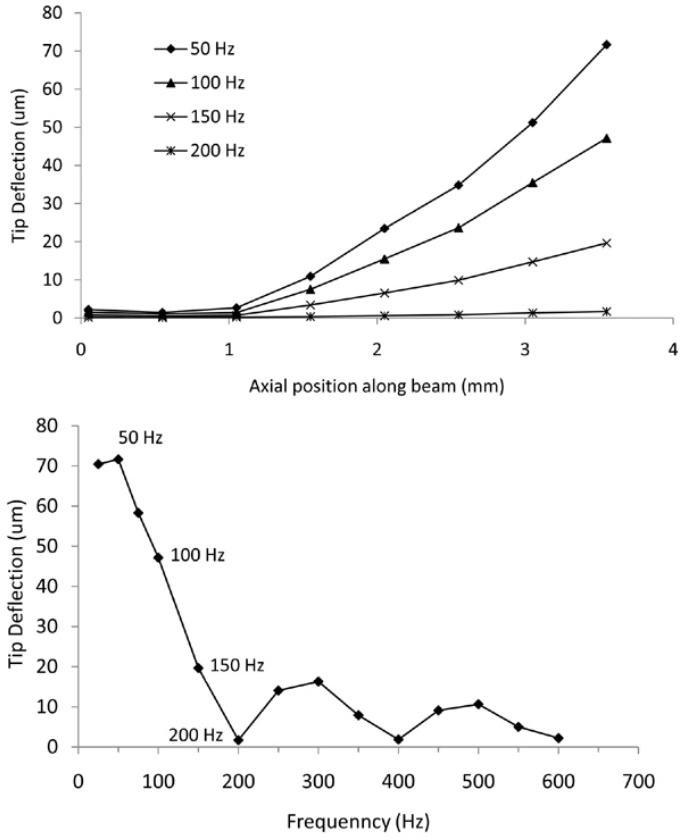

Fig. 4.32: The shape of a $2 \times 3.75mm$ bimorph during dynamic actuation.

occured. It was necessary to know the overall gradient of the actuator which was found by measuring the vertical position of the actuator base and tip before dynamic measurements were made. Fig. 4.32 shows the shape of the actuator from 50-200Hz (top) and the corresponding tip deflection (bottom). This indicates that the mode of the actuators oscillations does not change in this frequency range which is expected as we are far below the actuators fundamental mechanical resonance frequency.

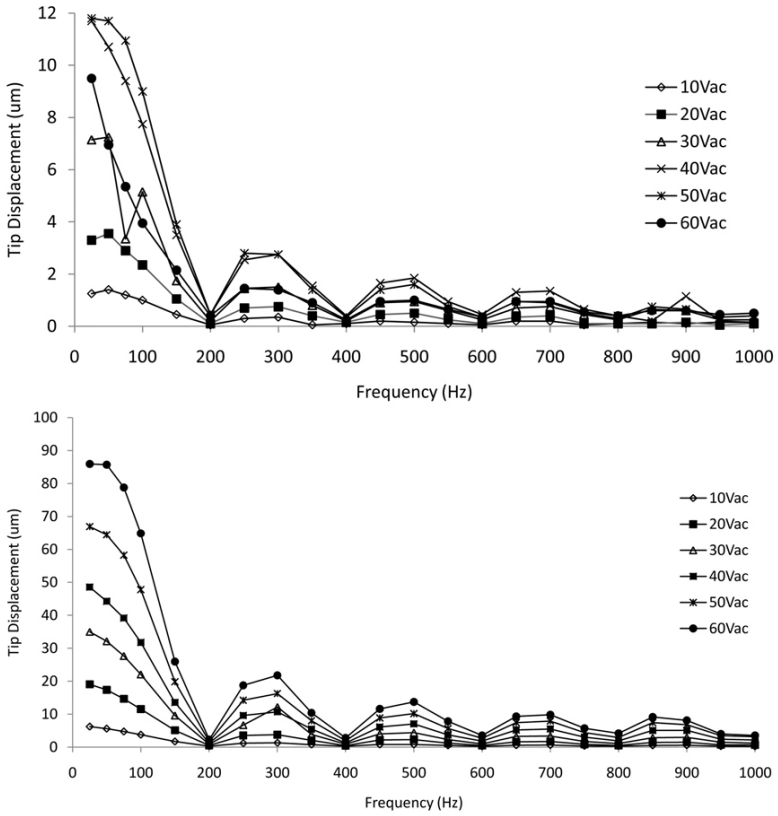

Fig. 4.33: The dynamic deflection response of $1.6 \times 3.75mm$ and $1.4 \times 2mm$ actuators with a sinusoidal source and Vac=10-60V. Note the consistent position of the minima.

4.3.1 The Electromechanical Coupling Coefficient

The dynamic electromechanical coupling coefficient of the actuators can be found from the change in impedence Z with frequency using the relation:

$$k_d^2 = \frac{\omega_a^2 - \omega_r^2}{\omega_a^2} \tag{4.10}$$

where ω_r and ω_a are the resonance and antiresonance frequencies respectively. These frequencies are determined from the impedence spectrum of a piezoelectric device, an example of which is shown in Fig. 4.34 which shows the spectrum for a $3.75 \times 2mm$ bimorph. For this actuator the coupling coefficient was found to be around $k_d = 0.2$. Chang *et al* describe the square of the EMCC as "the ratio of (mechanical) electrical energy stored in the volume of a piezoelectric body and is capable of conversion to the total mechanical (electrical) energy supplied to the body" [85]. Variations in the electromechanical coupling coefficient (EMCC) may be responsible for the frequency dependence of the dynamic deflection as Rogacheva *et al* show that the dependence of the dynamic EMCC displays a similar frequency dependence [86]. Rogacheva calculated the EMCC for a piezoelectric laminate structure and made experimental measurements which closely matched their model. The device they used to investigate the transverse bending EMCC was $10 \times 90.8mm$, the two layers of piezoelectric ceramic (Fuji Ceramics) were 0.3mm thick and the aluminium shim was 0.5mm thick (h_0/h_1=0.833). Fig. 4.35 shows a plot of the EMCC for transverse bending of the bimorph and three different ceramic materials. The variables k_d and k_e in Fig. 4.35 arise from two different definitions of the EMCC - k_d is the dynamic EMCC found from the resonance and antiresonance frequencies and k_e is the EMCC determined from the total energy of the piezoelectric multilayer structure in the open-circuit and short-circuit states. The d_{31} parameter is in turn dependent on the EMCC, k_{31}:

$$d_{31}^2 = \epsilon_{33}^T s_{11}^E k_{31}^2 \tag{4.11}$$

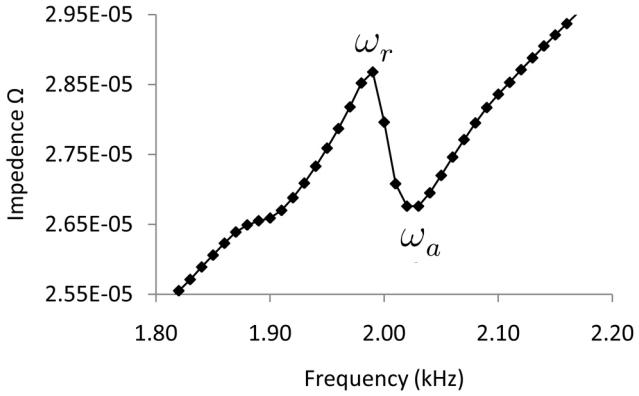

Fig. 4.34: The frequency dependence of the impendence Z of a $2 \times 3.75mm$ actuator.

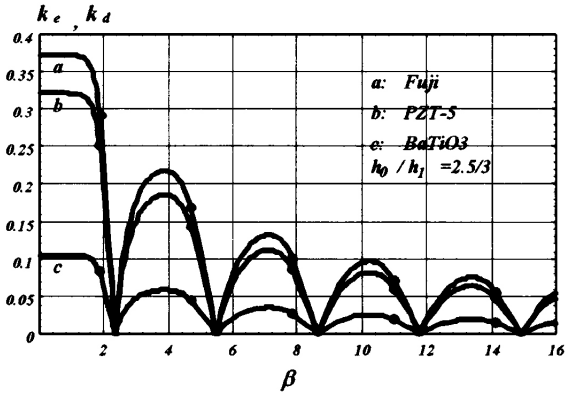

Fig. 4.35: The dynamic EMCC for a bimorph device [86]. Vtop=1.02Vbottom, β is a dimensionless frequency parameter. Three different ceramics were tested: Fuji, PZT 5, $BaTiO_3$ (h_0 is the half thickness of the elastic Aluminium layer and h_1 is the thickness of the piezoelectric ceramic).

At first glance the EMCC described by Rogacheva shows some promise in explaining the frequency dependent tip displacement, however, on closer examination the scale of β is too large, for example, 1kHz corresponds to $\beta = 0.3$ for Rogacheva's devices ($h_0/h_1 = 0.25/0.3 = 0.833$ where h_0 is the half thickness of the elastic layer and h_1 is the thickness of each active layer) and $\beta = 1$ for the actuators used in this work ($h_0/h_1 = 5/40 = 0.125$). Also the EMCC is constant in the range $\beta < 1.5$ which corresponds to $f < 2kHz$ which encompasses the range of frequencies used in the dynamic deflection measurements. Even if the EMCC did oscillate in the same range of frequencies as our actuators it would not explain why this oscillation has not been observed in similar devices.

4.4 Microvalve Performace - Static

Before the characteristics of the microvalve performance can be evaluated it is useful to establish the ideal behaviour of the microjet. This will allow us to evaluate the accuracy of the pressure measurement system and to determine the loss in pressure across the outlet. To establish these reference conditions the actuator was removed from the microvalve and a simple microjet flow was established across the pressure range (P_0 = 20, 40, 60, 80 kPa). This provides a maximum total pressure ratio of P_0/P_{atm}=1.8 which equates to an ideal Mach number of 0.96 with an associated maximum velocity of approximately $330ms^{-1}$. For the lowest pressure ratio (P_0/P_{atm} =1.2) the ideal maximum Mach number is 0.52 with a corresponding velocity of approximately $180ms^{-1}$. The microvalve design objective is a jet velocity of $200ms^{-1}$ which equates to a pressure ratio in excess of 1.26. The total pressure measurements were taken in the streamwise (axial) direction along the jet centreline at a variety of locations from x/D = 1.0 to 17.3 (Fig. 4.36).

These measurements are presented in the non-dimensionalised form of P_{Jet}/P_0 vs x/D in Fig. 4.36. This allows a direct comparison of the jet characteristics for a range of plenum total pressures. The measured jet pressure distributions for all pressure ratios exhibit a strong self-similarity with a characteristic decay profile. In addition, all of the jets exhibit a gauge total pressure ratio value close to 1.0 at the measurement nearest to the jet exit (x/D=2). As expected, due to the removal of the bimorph actuator there is very little total pressure loss and the Pitot probe measurements primarily highlight the expected inviscid core region of the jet. This is a typical sub-sonic jet characteristic and it provides confidence that the measurement system is capturing the sufficient information. Furthermore, the total pressure ratio decays with axial distance along the jet centreline as the jet entrains the surrounding ambient air and the jet mixes out at a rate which is proportional to the pressure ratio.

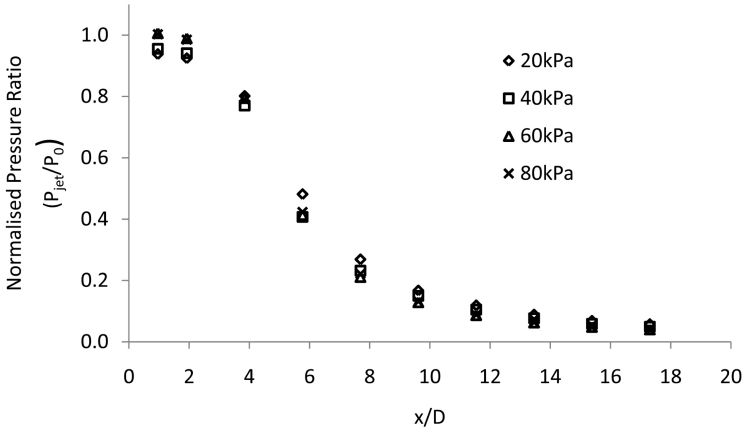

Fig. 4.36: Non-dimensionalised pressure ratio measured along the centreline of the jet generated by an "ideal" (i.e no actuator) open microvalve .

The performance of the actuated microvalve was investigated under static actuation of the bimorph where the supply voltage ranged from Vdc=30-60V. The jet flow chracteristics were examined across this range of bimorph actuation voltages in combination with a pressure ratio of 1.2, 1.4, 1.6 and 1.8. For the configurations with a pressure ratio of 1.6 (P_0=60kPa) a broader jet survey was conducted in both the streamwise and spanwise directions. Contour plots of the gauge pressure ratio distributions are presented in Fig. 4.37. The measurements show the extent and strength of the jet for a range of applied DC voltages. For Vdc=30V (Fig. 4.37(a)) there is very little evidence of the jet with only a small region of relatively low total pressure ratio. As the voltage increases to Vdc=40V, the microvalve has opened further and the jet extent and strength has increased. The maximum pressure ratio is approximately 1.41 which equates to a local jet velocity of approximately $250ms^{-1}$. There is a further increase in the jet for a voltage of Vdc=50V but there are only modest further differences as the voltage increases to 60V. Overall the maximum measured pressure ratio for this case of a gauge jet pressure of 1.52 corresponds to a velocity of approximately $280ms^{-1}$. The measurements indicate that there is a large loss in total pressure for Vdc=30V which is due to the small actuator deflection and the contorted flow path. As the

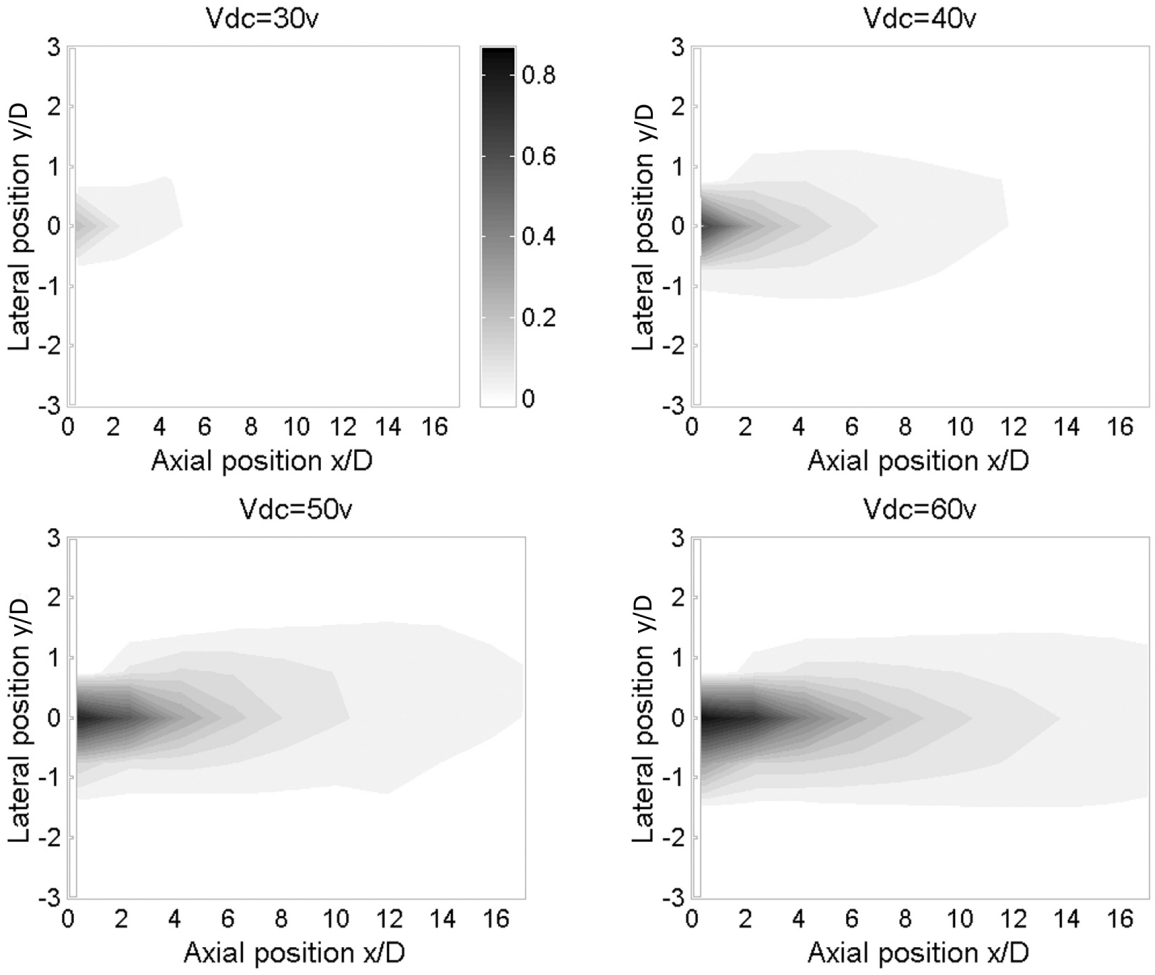

Fig. 4.37: Contour plots of the pressure ratio distributions in the microjets for Vdc=30-60V and a plenum pressure of 60kPa.

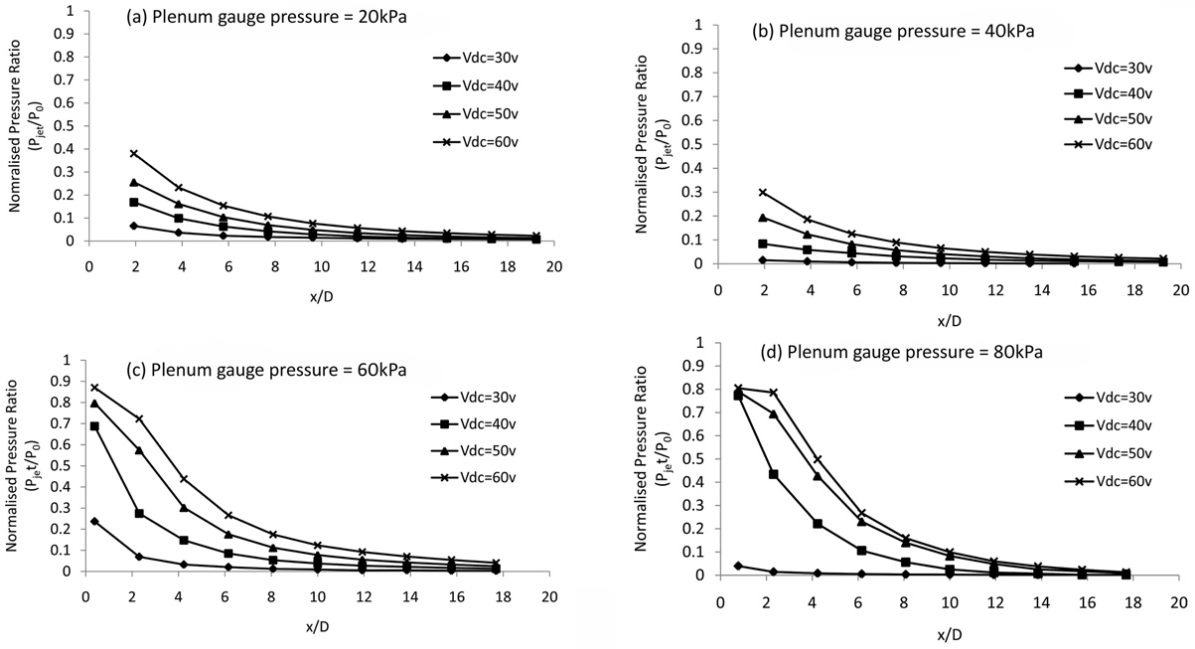

Fig. 4.38: The streamwise pressure distribution in the jet (Vdc=30-60V, P_0=20-80kPa).

bimorph deflects and the valve opens with increasing voltage this loss mechanism reduces and the jet extent and magnitude increases.

Details of the axial pressure distribution are presented in Fig. 4.38 which shows how the jet develops as both the internal pressure and actuation voltage of the bimorph are increased. As the actuation voltage is increased the microvalve outlet size will increase. With small openings the total pressure loss will be relatively large and is expected to reduce as the valve opens further. In addition, the deflection of the bimorph will depend on both the applied voltage and on the pressure in the plenum chamber which will be applying a resistive force. The lower voltage limit was Vdc=30V as values below this magnitude were not sufficient to open the outlet.

Fig. 4.38(a) and (b) show a linear rise in the pressure ratio as the actuation voltage increases. For the configuration with a plenum gauge pressure of 20kPa,

the peak value is in the order of 0.40. In comparison, for the reference valve measurement, the maximum value is approximately 1.0 (Fig. 4.36) which shows that even with the maximum voltage of Vdc=60V the flow still experiences a large total pressure loss due to the actuator. A similar trend is noticed for a pressure of 40kPa, although in this case the peak pressure ratio is slightly lower at about 0.3. This may be a combination of both the flow losses in the microvalve and the reduction in the orifice opening due to the increase in the plenum chamber pressure. Nevertheless, even for these relatively inefficient configurations at 20 and 40kPa the maximum pressure ratio equates to a peak jet velocity of approximately $140ms^{-1}$. Furthermore, once the valve is open and the flow is initiated (Vdc=30V), there is generally a linear increase in the total pressure ratio as the actuator voltage increases.

For the higher plenum pressures of 60 and 80 kPa, there is a notable difference in the jet characteristic when compared to that of the lower pressures of 20 and 40kPa. Although the jet total pressure values are still relatively low for Vdc=30V, as the voltage increases and the microvalve opens, there is a substantial increase in the maximum jet total pressure. For both 60kPa and 80kPa, and with Vdc=60V, the maximum gauge total pressure ratio is in the range of 0.8 to 0.9 (Fig. 4.38 (c), (d)). These values are similar to those measured for the reference micro-jet without the actuator (Fig. 4.36). This shows that for these higher driving pressures, once the valve is open the flow experiences modest pressure loss and the peak velocities are now in the region of $300ms^{-1}$. Finally, this behaviour is further highlighted for the 80kPa case where the increased pressure force on the valve means that when Vdc=30V, there is almost no evidence of the jet flow (Fig. 4.38 (d). The measurements at 80kPa show that once the value opens the flow quickly establishes a peak total pressure (approximately 0.8) and that the jet characteristics are non-linearly dependent on Vdc (Fig. 4.38 (d)). The differences in the microvalve performance for the maximum applied voltage of Vdc=60V is shown in Fig. 4.39 which plots the measured pressure ratio for a range of plenum

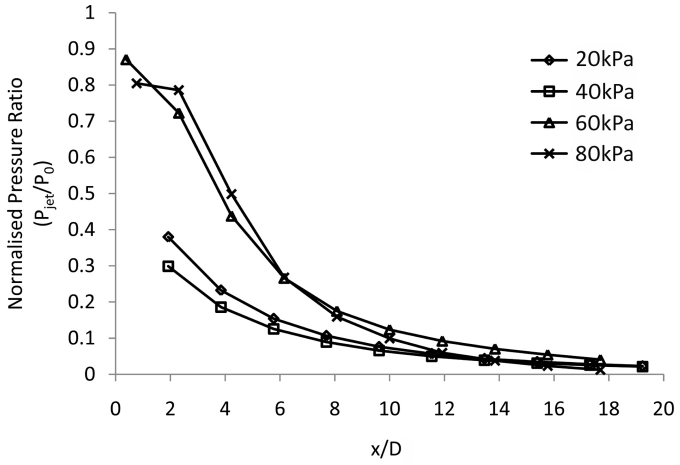

Fig. 4.39: The change in pressure ratio for a range of plenum pressures (Vdc=60V).

pressures. There is a clear change in the behaviour at the higher pressures while the total pressure losses are considerable for the 20kPa and 40kPa cases.

Another factor to keep in mind is the hysteresis response of bimorph actuator which will affect the static performance of the microvalve. To investigate the importance of this effect the pressure ratio 0.6mm (x/D=2.3) from the outlet was measured as Vdc was changed. The change in measured pressure ratio with applied voltage is shown in Fig. 4.40 where the solid lines indicate increasing Vdc and the dotted lines indicate decreasing Vdc. It is clear that the pressure ratio depends on whether Vdc is increasing or decreasing which is expected to be caused by the hysteresic deflection response of the actuator, however it is also clearly dependent on the plenum pressure. The underlying cause of the pressure dependence is unclear from this initial study and requires a more detailed analysis of the structure-fluid interaction.

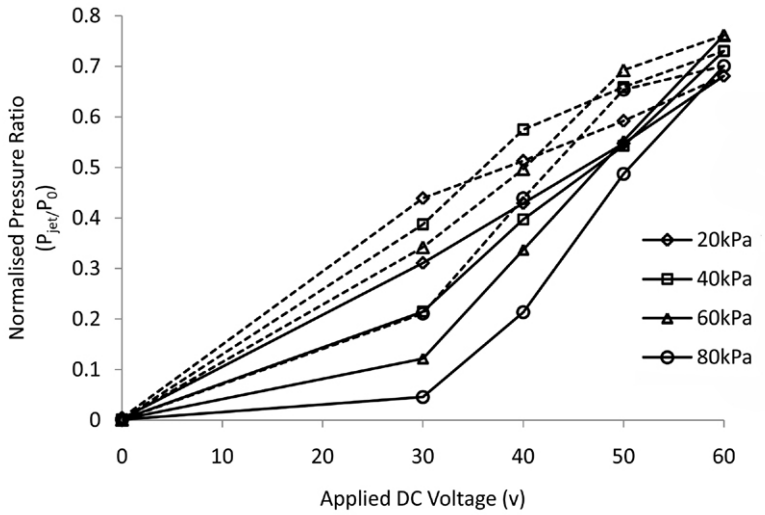

Fig. 4.40: The pressure ratio 0.6mm (x/D=2.3) from the outlet as Vdc is increased from 0V (solid line) and decreased to 0V (dotted line).

4.5 Microvalve Performance - Dynamic

To investigate the dynamic performance of the valve the bimorph was actuated with an AC signal and a positive DC offset voltage. The reason behind this was described in Fig. 3.4 in section 3.2. The bimorph motion is restricted by the valve outlet so the symmetrical response of the bimorph to an AC voltage is offset by applying a positive DC bias. The effect of static and dynamic actuation of the bimorph on the operation of the valve is illustrated by the shaded regions which indicate the fraction of the actuation cycle for which the valve is open. With a sufficiently large Vdc the the valve will be constantly open and the jet will have both steady and unsteady components.The amplitude of the AC and DC voltages must also be chosen so that (Vdc+Vac) does not greatly exceed the poling potential (60V) because high voltages may partially depole one or the other of the piezoelectric ceramic layers in the bimorph thereby reducing its deflection response to the applied potential.

The magnitude of the AC and DC components were carefully chosen so that the deflection due to Vdc was greater than the deflection due to Vac. Fig. 4.41 shows how the tip deflection of a $2 \times 3.75mm$ actuator with Vac=35V can be controlled with an offset voltage of 5-30V (the time dependent deflection profiles have been shifted along the time axis so that they can be compared). This combination of Vac and Vdc will ensure that the jet has a steady component which would increase the mass flow rate and an unsteady component which has been shown to generate a vortex ring around the outlet (these vortices are nicely visualised in Ref. [87] though Jabbal uses zero-net-mass-flux jets). The vortices entrain more fluid in the jet thereby allowing the jet to grow more rapidly perpendicular to the flow direction [88, 89]. It should be mentioned that the lateral distribution of the dynamically generated jet was not investigated here. Quiescent testing of the actuator's response indicated that for Vac=35V and Vdc=30V the tip deflection oscillated between $27\mu m$ to $120\mu m$ which would generate both steady and

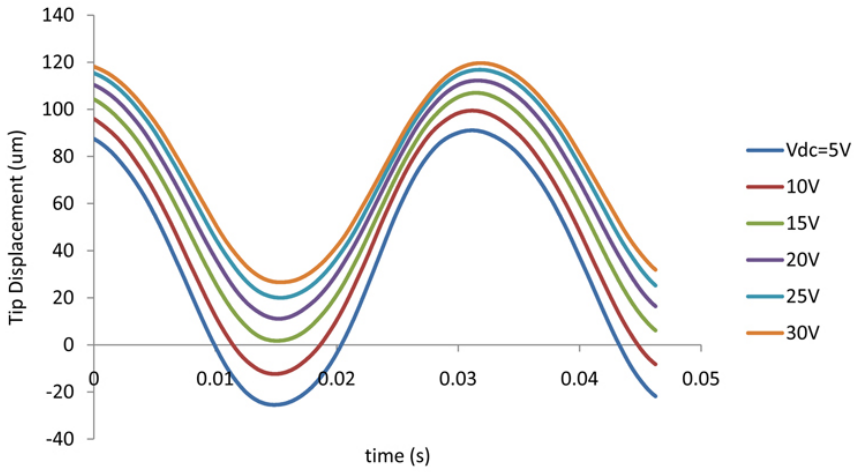

Fig. 4.41: The offset deflection behaviour of a $2 \times 3.75mm$ actuator with Vac=35V and Vdc=5-30V.

unsteady components in the jet. Fig. 4.41 shows how the actuator deflection (hence the outlet size) can be controlled by varying Vd. It is clear that the steady component of the jet can be completely removed by reducing the offset voltage to Vdc=15V which would close the outlet completely at the negative extreme of the actuator's oscillation.

Although this arrangement will provide for a modulated jet, the pressure measurement system does not have a sufficient bandwidth to capture the unsteadiness in the jet, however, it will measure the effect of the microvalve modulation on the time-averaged jet behaviour.

As the mode of operation of the valve is switched from static to dynamic there is a dramatic change in the performance. For comparison, the static cases of Vdc=30V and 60V are used as these encompass the configurations where the valve begins to open (30V) and the maximum static deflection occurs (60V). Three unsteady configurations are highlighted where the dynamic actuator voltage is applied at 25Hz, 200Hz and 500Hz which encompasses the range investigated in this study. Overall, the jet total pressure distributions for unsteady actuation (25-500Hz) lie

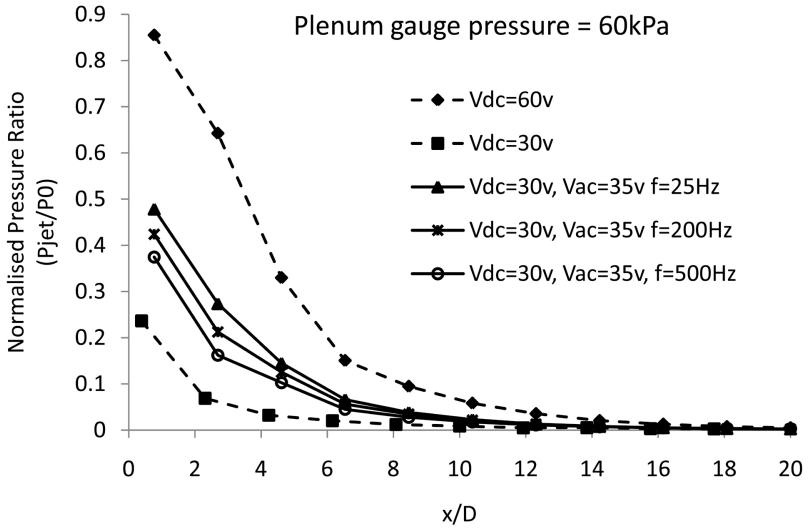

Fig. 4.42: The pressure distribution in the jet under dynamic actuation conditions.

between the minimum (30V) and maximum (60V) static configurations. The addition of the unsteady actuation at 25Hz results in a twofold increase in the total pressure ratio at the jet exit. This value is typically still half of that achieved with the valve statically actuated at the maximum voltage of Vdc=60V (Fig. 4.42). The pressure ratio decreases as the dynamic actuation frequency increases although it is relatively insensitive to this. Across the frequency range of 25-500Hz and at the measurement location closest to the jet outlet, the gauge total pressure ratio of the jet reduces by approximately 20% as the frequency increases from 25Hz to 500Hz. The measurements for all the other actuation frequencies are positioned between these extema as illustrated by the data for 200Hz which is monotonically positioned between these lower and higher frquencies (Fig. 4.42). The effect of the unsteady actuation is also observed further away from the jet exit where similar increases in the jet total pressure ratio were also measured. Although the pressure distribution is rather insensitive to the actuation frequency, to achieve the desired jet velocity of $200ms^{-1}$ with a internal pressure of 60kPa (P_{Jet}/P_0 0.43) the valve must be operated under about 300Hz.

If the deflection response of the bimorph actuator to a sinusoidal Vac is symmetrical we would expect the average actuator position for purely *static* actuation (Vdc) to be the same as for combined *static and dynamic* actuation (Vdc+Vac). Fig. 4.42 indicates, however, that the flow rate during dynamic operation (Vac=35V, Vdc=30V) is greater than the flow rate during purely static operation (Vdc=30V). This difference may be due to the larger open fraction of the actuation cycle (Fig. 3.4) or the oscillations of the actuator may be acting to assist the flow of gas through the outlet, an effect that has been observed under similar conditions [90].

Chapter 5

Conclusions

5.1 Force Measurement - Calibrated Springs

The use of calibrated reference springs to measure small forces is well established in the area of MEMS and atomic force microscopy. This technique was scaled up with the goal of measuring the tip force generated by a piezoelectric bimorph actuator. Silicon springs with a cantilever and V-shaped geometry were dry etched out of a $300\mu m$ <111> silicon wafer using the Bosch process. The normal spring constant of these springs was then investigated using a variety of dimensional models, static methods and dynamic techniques. The dimensional models were found to show good agreement with finite-element modelling and the static measurements of the springs especially as the aspect ratio of the springs increased. The dimensional models were also easy to use, however, they did require some information about the geometry of the springs and assumptions about material properties and dimension uniformity. The static mass measurements were the simplest empirical method that did not require any information about the spring shape or any assumptions about geometry, however, it was necessary to make corrections for the position of the off-end mass and deflection measurements. These corrections are small when using cantilever springs of the size used in this investigation. The dynamic methods required knowledge of the resonance frequency of the springs which was determined with LDV. The reference springs

were arranged in arrays which allowed easy measurement of the spring properties. Springs in the array were coupled so that information about the resonance frequency of all the springs could be found from the frequency response of a single spring in the middle of the array. The resonance frequency can be used in some of the dimensional models to eliminate the need to know the thickness of the spring which can be difficult to accurately measure. The dynamic methods that involved loading the springs with an off-end mass and measuring the change in resonance frequency of the spring-mass system were very time consuming to implement and contained more sources of error. It was found the normal spring constants calculated using this method had a much larger standard deviation than the static and dimensional methods and hence the results were less reliable, especially in the case of the V-shaped springs. V-shaped springs should be avoided if possible as some of the calibration options have not been extended theoretically to include V-shaped devices and physically they are larger and less robust. In conclusion we can say that, with reference springs of this magnitude (w=1mm, L=10-20mm, t=300μm), the dimensional and finite-element models are the logical choice of calibration method of cantilever springs due to the ease and speed with which they can be implemented and the consistency of the results.

5.2 The Bimorph Actuator

The bimorph actuators used in this work are prestressed due to the high temperature adhesion bonding of the ceramic and elastic layers. The prestress enhances the response of the actuators by affecting the d_{31} constant which results in improved tip deflections and tip forces. The deflection response of the bimorph actuators was directly measured with a commercailly available laser triangulaton sensor. The tip force generated by the actuators was found by measuring the deflection of a spring-actuator arrangement. To calculate the tip force from the deflection measurements it was necessary to correct for the off-end measurement

position and the off-end point of contact between the actuator and the reference spring. A finite-element model of the silicon springs and analytical expressions for the deflection of a piezoelectric bimorph were used to calculate these corrections.

The response of the bimorph can be considered to be the superposition of the responses of the individual active layers. The top and bottom ceramic layers showed different tendencies which suggested that the electric field experienced by each layer was different. Although P-E hystereses were not collected for these actuators, work in the literature suggests that the dielectric constant was dependent on the applied field polarity and magnitude which would help to explain the asymmetry of the deflection and force results.

The transverse piezoelectric coefficient was calculated for each ceramic layer by considering the deflection generated when they were individually actuated and using an analytical expression for the deflection of a unimorph. The transverse piezoelectric coefficient was found to vary considerably between the active layers which reflects the asymmetry in the tip deflection.

The dynamic deflection response of the actuators showed a strong frequency dependence that was not simply related to the natural resonance frequency of the actuators. At low frequencies (<100Hz) and particularly for a square-wave voltage source, the tip deflection is similar to the static actuation case, however, the deflection amplitude oscillates, falling to (near) zero at 200Hz, 400Hz, 600Hz. This oscillating deflection response was consistently observed for actuators with different dimensions (w, L) but has not been reported in the literature. The origin of this behaviour is unclear, however, the frequency dependence of the electromechanical coupling coefficient may contribute to this effect. Despite the fact that there is much that we do not understand about prestressed actuators and in particular the behaviour of Cranfield's bimorph, the flexibiliity of the dimensions and geometry of their multilayer structure and their favourable deflection and force per unit volume combine to make these actuators very

attractive for MEMS and microsystems applications.

5.3 The Foturan Microvalve

Foturan is a promising material for microfluidic and lab-on-a-chip applications, however, there are some limitations that arise due to the processing steps required to structure it. Firstly, the etch rate of Foturan is very sensitive to the exposure conditions so a well characterised and uniform UV source is required if this effect is to be exploited to control the etch rate. A variable transmission mask was fabricated using absorbing layers (<30nm) of titanium to control the energy through a glass mask. This method worked well to control the local etch rate of Foturan, however, the nonuniform etch rate limits the surface quality achievable with this technique. The UV sensitivity and etch rate of Foturan is also highly dependent on the precise composition of the glass although this relationship was not investigated here. If this technique were to be used to fabricate Foturan components with consistent dimensions and different channel depths it would be necessary to establish in detail the relationship between Foturan composition and its UV sensitivity/etch rate.

A bimorph actuator ($2 \times 3.75mm$) was successfully integrated into a Foturan microvalve with an outlet diameter of $260\mu m$. The microvalve was characterized under static (Vdc=30-60V) and dynamic (Vdc=30V, Vac=35V) operating conditions and 2080kPa internal gauge pressure. Total gauge pressure ratio distributions in the jet were measured using a Pitot probe. Exit velocities in excess of $200ms^{-1}$ were measured for internal pressures >60kPa and static actuation voltages Vdc>40V. Under static operating conditions and pressures of 20 and 40kPa, the jet pressure is substantially affected by losses in the system. Under these conditions the jet total pressure ratio is linearly related to the actuation voltage. At higher jet pressures (60, 80kPa), there is a change in the flow characteristics with a substantial increase in the jet pressure ratios with a

maximum jet velocity of approximately $300ms^{-1}$, however, the microjet behaviour is more sensitive to and non-linearly dependent on the applied actuator voltage.

For a 60kPa configuration with a dynamic 25Hz actuation voltage Vac=35V and an offset Vdc=30V, the time average jet total pressure ratio approximately doubles relative to the purely static actuator voltage of Vdc=30V. The jet is found to be relatively insensitive to the dynamic actuation frequency across the range 25-500Hz with approximately a 20% reduction across this range of frequencies. The design objective of a time averaged jet velocity of $200ms^{-1}$ for dynamic actuation with a driving pressure of 60kPa requires the unsteady actuation to be at a frequency <300Hz.

5.4 Future Work

There is still much that we do not understand about the effect of prestress and poling conditions on the dielectric, piezoelectric and mechanical properties of the bimorph actuators. The dynamic behaviour is especially puzzling and if these actuators are to be used in applications where their frequency response is important further study will be necessary. Preliminary studies of the capabilities of these actuators as energy harvesters has yielded promising results which could lead to more compact and efficient devices that in turn will open up a door to more applications. The main limitation of the microvalve characterisation setup was the inability to resolve the time dependent jet behaviour. If these Foturan microvalves are to be used in active flow control applications then the temporal and spatial evolution of individual microjets, the effect of an array of these devices on the macroscopic air flow and the interaction of the actuator with the air flow inside the microvalve are all topics that require further study.

References

[1] S. Stemmer, S.K. Streiffer, F. Ernst, M. Rhle, Atomistic structure of 90° domain walls in ferroelectric $PbTiO_3$ thin films, Phil. Mag. A 71 (1995) 713-724.

[2] R.G. Ballas, Piezoelectric Multilayer Beam Bending Actuators Static and Dynamic Behavior and Aspects of Sensor Integration, Springer, ch 3, 2007.

[3] Q.-M. Wang, L.E. Cross, Performance analysis of piezoelectric cantilever bending actuators, Ferroelectrics, vol. 215 (1998) 187-213.

[4] J.M. Gere, Mechanics of Materials, Brooks/Cole, 5th edition, 2001, 417-418.

[5] R.J. Roark, W.C. Young, Formulas for Stress and Strain, 5th edition, McGraw-Hill, New York, 1975, 113-115.

[6] J. Jutti, Prestressed piezeoelectric actuator for micro and fine mechanical applications, Phd Thesis, University of Oulu (2006).

[7] G.H. Haertling, Rainbow ceramics-a new type of ultra-high-displacement actuator, Am. Ceram. Soc. Bull., 73 93-6.

[8] J. Juuti, Displacement, stiffness and load behaviour of laser-cut RAINBOW actuators, J. European Cer. Soc., 24 (2004) 1901-1904.

[9] G. Li, E. Furman, G.H. Haertling, Stress-enhanced displacements in PLZT Rainbow actuators, J. Am. Ceram. Soc., 80 6 (1997) 1382-88.

[10] J.F. Campbell, A simple sensor model for THUNDER actuators, Smart MAter. Struc. 18 (2009) 095011.

[11] K.J. Yoon, K.H. Park, H.C. Park, D. Perreux, Thermal deformation analysis of curved actuators LIPCA with a piezoelectric ceramic layer and fiber composite layers, Composites Science and Technology 63 (2003) 501-506.

[12] K.Y. Kim, K.H. Park, H.C. Park, N.S. Goo, K.J. Yoon, Performance evaluation of lightweight piezo-composite actuators, Sensors and Actuators A, 120 (2005) 123-129.

[13] X. Li, J.S. Vartuli, D.L. Milius, I.A. Aksay, W.Y. Shih, W.-H. Shih, Electromechanical properties of a ceramic d_{31}-gradient flextensional actuator, J. Am. Ceram. Soc. 84, 5 (2001) 996-1003.

[14] B. Ohler, Application Note 94: Practical advice on the determination of cantilever spring constants, Veeco Technical notes (2007), www.veeco.com/library.

[15] J.E. Sader, Calibration of atomic force microscope cantilevers, Encyclopedia of Surface and Colloid Science, (2002) 846-856.

[16] N. A. Burnham, X. Chen, C.S. Hodges, G.A. Matei, E.J. Thoreson, C.J. Roberts, M.C. Davies, S.J.B. Tendler, Comparison of calibration methods for atomic-force microscopy cantilevers, Nanotechnology 14 (2003) 1-6.

[17] C.A. Clifford, M.P. Seah, The determination of atomic force microscope cantilever spring constants via dimensional methods for nanomechanical analysis, Nanotechnology 16 (2005) 1666-1680.

[18] J.M. Gere, Mechanics of Materials, Fifth edition, Brooks/Cole (2001) p646.

[19] J.M. Gere, Mechanics of Materials, Fifth edition, Brooks/Cole (2001) p877.

[20] M.A. Poggi, A.W. McFarland, J.S. Colton, L.A. Botttomley, A method for calculating the spring constant of atomic force microscopy cantilevers with a nonrectangular cross section, Anal. Chem. 77 (2005) 1192-1195.

[21] J.M. Gere, Mechanics of Materials, Fifth edition, Brooks/Cole (2001) p878.

[22] R. Proksch, T.E. Schaffer, J.P. Cleveland, R.C. Callahan, M.B. Viani, Finite optical spot size and position corrections in thermal spring constant calibration, Nanotechnology 15 (2004) 1344-1350.

[23] H.-J. Butt, M. Jaschke, Calculation of thermal noise in atomic force microscopy, Nanotechnology, 6 (1995) 1-7.

[24] J.E. Sader, J.W.M. Chon, P. Mulvaney, Calibration of rectangular atomic force microscope cantilevers, Rev. Sci. Instrum., 70 10 (1999) 3967-3969.

[25] S.M. Cook, T.E. Schaffer, K.M. Chynoweth, M. Wigton, R.W. Simmonds, K.M. Lang, Practical implimentation of dynamic methods for measuring atomic force microscope cantilever spring constants, Nanotechnology 17 (2006) 2135-2145.

[26] J.E. Sader, Atomic force microscope cantilevers (calibration method of Sader), `http://www.ampc.ms.unimelb.edu.au/afm`, last updated: Dec 1, 2010.

[27] S.A. Edwards, W.A. Ducker, J.E. Sader, Influence of atomic force microscope cantilever tilt and induced torque on force measurements, J. Appl. Phys. 103 (2008) 064513.

[28] C. Iliescu, Strategies in deep wet etching of Pyrex glass, Sensors & Actuators A 133 2007 395-400.

[29] G.A.C.M. Spierings, Review Wet chemical etching of silicate glasses in hydroflouric acid based solutions, J. Materials Science 28 (1993) 6261-6273.

[30] I. Steingoetter, H. Fouckhardt, Deep fused silica wet etching using an Au-free and stress-reduced sputter deposited Cr hard mask, J. Micromech. Microeng. 15 (2005) 2130-2135.

[31] M. Bu, T. Melvin, G.J. Ensell, J.S. Wilkinson, A.G.R. Evans, A new masking technology for deep glass etching and its microfluidic application, Sensors & Actuators A 115 (2004) 476-482.

[32] C. Iliescu, J. Ji, F.E.H. Tay, J. Miao, T.T. Sun, Characterisation of masking layers for deep wet etching of glass in an improved HF/HCl solution, Surf. Coat. Technol. 198 (1-3) (2005) 314-318.

[33] P.W. Leech, Reactive ion etching of quartz and silica-based glasses in CF_4/CHF_3 plasmas, Vacuum 5 (1999) 191-196.

[34] X. Li, T. abe, M. Esashi, Deep reactive ion etching of Pyrex glass using SF_6, Sensors & Actutors A 87 (2001) 139-145.

[35] J.H. Park, N.-E. Lee, J. Lee, J.S. park, H. D. Park, Deep dry etching of borosilicate glass using SF_6 and SF_6/Ar inductiviely coupled plasmas, Microelectronic Eng. 82 (2005) 119-128.

[36] S.D Stookey, Catalyzed Crystallization of Glass in Theory and Practice, Ind. Eng. Chem., vol. 51 no. 7 (1949).

[37] J.S. Stroud, Photoionisation of Ce^{3+} in Glass, J. of Chem. Phys., vol. 35 no. 3 844-850.

[38] S.E. Paje, Cerium doped soda-lime-silicate glasses: effects of silver ion-exchange on optical properties, Optical Materials 17 (2001) 459-469.

[39] A.M. Hu, Phase transformation of $LiO_2 - Al_2O_3 - SiO_2$ glasses with CeO_2 addition, Ceramics International, 31 (2005) 11-14.

[40] A. M. Hu, Effect of nucleation temperatures and time on crystallization behavior and properties of $LiO_2 - Al_2O_3 - SiO_2$ glasses, Materials Chemistry and Physics 98 (2006) 430-433.

[41] M. Guedes, Nucelation and crystal growth in commercial LAS compositions, J. European Cer. Soc. 21 (2001) 1187-1194.

[42] X. Guo, Nucleation of lithium alumino silicate glass containing complex nucleating agent, Ceramics International 33 (2007) 1375-1379.

[43] T.R. Dietrich, Photoetchable glass for microsystems: tips for atomic force microscopy, J. Micromech. Microeng. 3 (1993) 187-189.

[44] T.R. Dietrich, Fabrication technologies for microsystems utilizing photoetchable glass, Microelectronic Eng. 30 (1996) 497-504.

[45] Y.R Cho, Micro-etching technology of high aspect ratio frameworks for electronic devices, Materials Science and Engineering B64 (1999) 79-83.

[46] Mikroglas Chemtech GmbH, Foturan Glass, `http://www.mikroglas.com/index.php?PAGE_ID=538#`, date checked: 05/08/2011.

[47] Y. Cheng, K. Sugioka, K. Midorikawa, Microfabrication of 3D hollow structures embedded in glass by femtosecond laser for Lab-on-a-chip applications, Appl. Surface Sci., Vol. 248, No. 1-4, (2005), 172-176.

[48] Y. Hanada, K. Sugioka, H. Kawano, I.S. Ishikawa, A. Miyawaki, K. Midorikawa, Nano-aquarium for dynamic observation of living cells fabricated by femtosecond laser direct writing of photostructurable glass, Biomed Microdevices, 10 (2008) 403-410.

[49] S. Etoh T. Fujimura, R. Hattori, Y. Kurok, Fabrication of on-chip microcapillary using photosensitive glass, Microsystems Technologies, Vol. 9, No. 8, (2005) 541-545.

[50] M. Masuda, K. Sugioka, Y. Cheng, T. Hongo, K. Shihoyama, H. Takai, I. Miyamoto, K. Midorikawa, Direct fabrication of freely movable microplate inside photosensitive glass by femtosecond laser for lab-on-a-chip application, Appl. Phys. A 78 (2004) 1029-1032.

[51] K. Sugioka, Y. Cheng, K. Midorikawa, Three-dimensional micromachining of glass using femtosecond laser for lab-on-a-chip device manufacture, Apply. Phys. A 81 (2005) 1-10.

[52] U. Brokman, M. Jacquorie, M. Talkenberg, A. Harnisch, E.-W. Kreutz, D. Hulsenberg, R. Poprawe, Exposure of photosensitive glasses with pulsed UV-laser radiation, Microsystem Tecchnologies 8 (2002) 102-104.

[53] F. E. Livingston, H. Helvajian, Selective activation of material property changes in photostructurable glass ceramic materials by laser photophysical excitation, J. of Photochemistry and Photobiology A: Chemistry, 182 (2006) 310-318.

[54] Y. Cheng, K. Sugioka, K. Midorikawa, Freestanding optical fibers fabricated in a glass chip using femtosecond laser micromachining for lab-on-a-chip application, Otpics Express vol. 13, no. 18 (2005) 7225-7232.

[55] M. Masuda, K. Sugioka, Y. Cheng,, N. Aoki, M. Kawachi, K. Shihoyama, K. Toyoda, H. Helvajian, K. Midorikawa, 3-D microstructuring inside photosensitive glass by femtosecond laser excitation, Appl. Phys. A 76 (2003) 857-860.

[56] H. Helvajian, P.D. Fuqua, W.W. Hansen, S. Janson, Laser microprocessing for nanosatellite microthruster applications, RIKEN review No. 32: Focused on Laser Precision Microfabrication (LPM200), (2001) 57-63.

[57] F. E. Livingston, P.M. Adams, H. Helvajian, Influence of cerium on the pulsed UV nanosecond laser processing of photostructurable glass ceramic materials, Applied Surface Science 247 (2005) 526-536.

[58] T. Hongo, K. Sugioka, H. Niino, Y. Cheng, M. Masuda, I. Miyamoto, H. Takai, K. Midorikawa, Investigation of photoreaction mechanism of photosensitive glass by femtosecond laser, J. Appl. Phys. 97 (2005) 063517.

[59] R. Jourdain, Ultra-precision grinding of piezoelectric ceramic thick films for fabrication of pre-stressed bimorph microactuators and development of new numerical models to assess induced thermal stress in multilayer structure, PhD thesis, Cranfield University, UK, 2006.

[60] S. A. Wilson, R. Jourdain, S. Owens, Pre-stressed piezoelectric bimorph micro-actuators based on machined 40-micron PZT ceramic thick films batch scale fabrication and integration with MEMS, Journal of Smart Materials and Structures, 19, 2010, 094001.

[61] C.-O. Chang, G.-E. Chang, C.-S. Chou, W.-T. Chang Chien, P.-C. Chen, In-plane free vibration of a single-crystal silicon ring, Int. J. of Solids and Structures 45 (2008) 6114-6132.

[62] Technical Data Sheet 758: Glass Beads, `http://www.polysciences.com/SiteData/docs/TDS%20758/fd6013c6b0de06c3/TDS%20758.pdf`, date checked: 05/08/2011.

[63] Y. Gan, Invited Review Article: A review of techniques for attaching micro- and nanoparticles to a probe's tip for surface force and near-field optical measurements, rev. Sci. Instrum. 78 (2007) 081101.

[64] K.W. Oh, C.H. Ahn, Topical Review: A review of microvalves, J. Micromech Microeng. 16 (2006) R13-R39.

[65] C. Warsop, Results and lessons learned from the European AEROMEMS II project, 3rd AIAA Flow Control Conference, 5-8 June 2006, San Francisco, California, AIAA 2006-350.

[66] The Handbook of Fluid Dynamics, edited by Richard W Johnson, CRC Press, 1998, chapter 33, section 9 to 14.

[67] E. L. Houghten, P. W. Carpenter, Aerodynamics for Engineering Students, Ch 6, 5th Edition, Butterworth Heinemenn, 2003.

[68] S. Ghatnekar-Nilsson, J. Graham, R. Hull, L. Montelius, Multi-frequency response from a designed array of micromechanical cantilevers fabricated using a focused ion beam, Nanotechnology 17 (2006) 5233-5237.

[69] T. Li, Y.H. Chen, F.Y.C. Boey, J. Ma, Domain reorientation of piezoelectric bending actuators, Sensors and Actuators A 134 (2007) 544-554.

[70] J. Juuti, H. Jantunen, V.-P. Moilanen, S. Leppavuori, Poling conditions of pre-stressed piezoelectric actuators and their displacement, J. Electroceramics 15 (2005) 57-64.

[71] J.S. Forrester, E.H. Kisi, Ferroelastic switching in a soft lead zirconate titanate, J. European Ceramic Society 24 (2004) 595-602.

[72] M.-A. Dubois, P. Muralt, Measurement of the effective transverse piezoelectric coefficient $e_{31,f}$ of AlN and $Pb(Zr_x, Ti_{1-x})O_3$ thin films, Sensors and Actuators A 77 (1999) 106-112.

[73] I. Kanno, H. Kotera, K. Wasa, Measurement of transverse piezoelectric properties of PZT thin films, Sensors and Actuators A 107 (2003) 68-74.

[74] J.G. Smits, W. Choi, The constituent equations of piezoelectric heterogenous bimorphs, IEEE Trans. Ultrasonics Freq. Control 38 (1991) 256-270.

[75] Noliac, Plate bender 7 (CMBP07), `http://www.noliac.com/Default.aspx?ID=739&NPMode=View\&ProductID=31`, date checked: 05/08/2011.

[76] Steiner & Martins, Inc., Piezoelectric Parallel Bimorph Actuators,`http://www.steminc.com/piezo/PZ_SpecSheet.asp?PZ_SM_MODEL=SMBTA352D2T07M`, date checked: 05/08/2011.

[77] Mide, QP20n Piezoelectric Sensor and Actuator, `http://www.mide.com/products/qp/qp20n.php`, date checked: 05/08/2011

[78] Phisik Instrumente, PL112, PL140 PICMA Bender Actuators, `http://www.physikinstrumente.com/en/products/prspecs.php?sortnr=103000` date checked: 05/08/2011.

[79] Face International Corporation, Multilayer Piezo Bender, `http://www.prestostore.com/cgi-bin/pro23.pl?ref=thunderonline&ct=51136`, date checked: 05/05/2011.

[80] Face International Corporation, THUNDER actuator, `http://www.prestostore.com/cgi-bin/pro23.pl?ref=thunderonline&ct=36234`, date checked: 05/08/2011.

[81] T. Li, Frequency dependence of vibration velocity, Sensors an Actuators A 138, 2007 404-410.

[82] J.G. Smits, A. Ballato, Resonance and antiresonance of symmetric and asymmetric cantilevered piezoelectric flexors, IEEE Trans. Ultrasonics, 44 2 (1997) 250-258.

[83] R.J. Wood, E. Steltz, R.S. Fearing, Optimal energy density piezoelectric bending actuators, Sensors and Actuators A 119 (2005) 476-488.

[84] O. Kursu, A. Kruusing, M. Pudas, T. Rahkonen, Piezoelectric bimoorph charge mode force sensor, Sensors and Actuators A 153 (2009) 42-49.

[85] S.H. Chang, N.N. Rogacheva, C.C. Chou, Analysis of methods for determining electromechanical coupling coefficients of piezoelectric elements, IEEE Trans. Ultrasonics, 42 4 (1995) 630-640.

[86] N.N. Rogacheva, C.C. Chou, S.H. Chang, Electromechanical analysis of a symmetric piezoelectric/elastic laminate structure: theory and experiment, IEEE Trans. Ultrasonics, 45 2 (1998) 285-294.

[87] M. Jabbel, S. Zhong, The near wall effect of synthetic jets in boundary layer, Int. J. Heat and Fluid Flow 29 (2008) 119-130.

[88] S.G. Mallinson, J.A Reizes, G. Hong, P.S. Westbury, Analysis of hot-wire anemometry data obtained in a synthetic flow, Experimental Thermal and Fluid Science 28 (204) 265-272.

[89] B.L. Smith, G.W. Swift, A comparison between synthetic jets and continuous jets, Experiments in Fluids 34 (2003) 467-472.

[90] R. S. Wiederkehr, M. C. Salvadori, J. Brugger, F. T. Degasperi, M. Cattani, The gas flow rate increase obtained by an oscillating piezoelectric actuator on a micronozzle, Sensors and Actuators A 144 (2008) 154-160.

Appendix A

Finite-element model of the cantilever and V-shaped springs

This appendix lists the ANSYS script used to perform (1) a *static* analysis to determine the static deflection of the springs under a static load at a tip node of the beam and (2) a *modal* analysis to determine the resonant frequency of the spring.

A.1 Cantilever Springs

```
! SIMPLE CANTILEVER - DEFLECTION UNDER STATIC LOAD
! - linear elastic, anisotropic material, no tip, no base, no hole.
FINISH
/clear
/output,term
/units,SI
/show
/prep7
! Define cantilever dimensions
L=10.5e-3 !Ideal length
W=1e-3  !Ideal width
! Reduce these dimensions to take into account lateral etching
LT=L-7e-6
LB=LT-40e-6
WT=W-7e-6
WB=WT-40e-6
delW=(WT-WB)/2
th=318e-6
load=2e-3 ! STATIC LOAD
et,1,solid64  ! Anisotropic 3D solid
! MATERIAL PROPERTIES ******************************************
MP,DENS,1,2330 ! Density (Kg/m^3)
```

```
!"In-plane free vibration of a single-crystal silicon ring"
! Chia-Ou Chang et al
! Int. J. of Solids and Structures 45 2008 p6114-6132
C11=194.4e+9    !Anisotropic Stiffness matrix values
C12=54.3E+9
C13=44.8E+9
C15=-13.5E+9
C33=204E+9
C44=60.5E+9
C66=70E+9

TB,ANEL,1       !Activate table for anisotropic stiffness matrix

TBDATA,1,C11
TBDATA,2,C12
TBDATA,3,C13
TBDATA,5,C15
TBDATA,7,C11
TBDATA,8,C13
TBDATA,10,-C15
TBDATA,12,C33
TBDATA,16,C44
TBDATA,18,-C15
TBDATA,19,C44
TBDATA,21,C66

! DEFINE GEOMETRY ************************************************

! Specify keypoints for volume
k,1,0,0,0                ! K, NPT, X, Y, Z - Defines a keypoint.
k,2,LT,0,0
k,3,LT,WT,0
k,4,0,WT,0

k,5,0,delW,th
k,6,LB,delW,th
k,7,LB,delW+WB,th
k,8,0,delW+WB,th

V,1,2,3,4,5,6,7,8

! MESHING ********************************************************
VSEL,S,,,1
TYPE,1              !element type
MAT,1
ESIZE,100e-6,!Specifies element size. Try LESIZE to change spacing ratio
MSHAPE,0,3D      !0=quadrilateral elements, 1=tetrahedral elements
VMESH,1

! SOLVE **********************************************************
/SOLU                  !Enter solution processor
ALLS

DA,5,ALL,UX,,,,,UY,UZ !Apply constraints to base, DOF=0

! IF THE LENGTH OF THE BEAM IS CHANGED THE NODE
! AT WHICH THE STATIC FORCE IS APPLIED MUST BE CHANGED HERE.

!F,107,FZ,load  !10mm beam
!F,212,FZ,load  !10mm beam  Esize=50um
F,112,FZ,load  !10.5mm beam

!F,117,FZ,load  !11mm beam
!F,122,FZ,load  !11.5mm beam

!F,127,FZ,load  !12mm beam
!F,132,FZ,load  !12.5mm beam

!F,137,FZ,load  !13mm beam
!F,142,FZ,load  !13.5mm beam

!F,147,FZ,load  !14mm beam
```

```
!F,152,FZ,load  !14.5mm beam

!F,157,FZ,load  !15mm beam
!F,162,FZ,load  !15.5mm beam

!F,167,FZ,load  !16mm beam
!F,172,FZ,load  !16.5mm beam

!F,177,FZ,load  !17mm beam
!F,182,FZ,load  !17.5mm beam

!F,187,FZ,load  !18mm beam
!F,192,FZ,load  !18.5mm beam

!F,197,FZ,load  !19mm beam
!F,202,FZ,load  !19.5mm beam

!F,207,FZ,load  !20mm beam
!F,212,FZ,load  !20.5mm beam

!F,217,FZ,load !21mm beam   Esize=100um
!F,432,FZ,load !21mm beam   Esize=50um
!F,222,FZ,load !21.5mm beam

ALLS
ANTYPE,STATIC             ! Static analysis
SOLVE                       ! Solve current load step
FINISH                        ! Exit active processor

/POST1
/EFACET,1
PLNSOL, U,SUM, 0,1.0

! Plot path - beam deflection
PATH,edge,2,30,20,
PPATH,1,0,0,0,0,0,
PPATH,2,0,LT,0,0,0,
AVPRIN,0, ,

! Map average beam deflection along path
PDEF,edge,U,Z,AVG
/PBC,PATH, ,0

! Plot path data
PLPATH,EDGE
PRPATH,EDGE

FINISH
```

To determine the resonant frequency of the springs a *modal* solution can be used by using the same geometry as the static solution and by substituting the following steps into the above script.

...

```
! MESHING ***************************************************
VSEL,S,,,1
TYPE,1              !element type
MAT,1
MSHKEY,1           ! mapped mesh
ESIZE,100e-6,         ! divisions set by ESIZE
MSHAPE,0,3D      !0=quadrilateral elements, 1=tetrahedral elements
VMESH,1

! SOLVE ******************************************************
/SOLU                  !Enter solution processor
ALLS

ANTYPE,2  !Modal analysis - calculate 1st and 2nd modes.
MODOPT,SUBSP,1 !Subspace,1 mode
```

```
EQSLV,FRONT !Frontal solver
MXPAND,5 !Expand 5 modes
DA,5,ALL,UX,,,,,UY,UZ !Apply constraints to base, DOF=0
SOLVE                        ! Solve current load step
FINISH                         ! Exit active processor
/POST1
SET,LIST  !list the resonant frequencies
```

A.2 V-shaped Springs

```
! SIMPLE V SPRING - STATIC ANALYSIS
! - linear, anisotropic, no tip, no base, no hole etc
FINISH
/clear
/output,term
/units,SI
/show
/prep7
*AFUN,DEG  !Angles in degrees
!Spring dimensions
L1=10.0e-3 !User defined
theta=30  !Angle of V beams
width=0.5e-3 !width of each beam
L2=L1-(width/(sin(theta/2)))       !Inner length of V spring
W1=2*L1*tan(theta/2)      !Outer width of V spring
W2=2*L2*tan(theta/2)      !Inner width of V spring
tht=318e-6
thb=318e-6
load=2e-3 !Load
et,1,solid186 ! Anisotropic elements (or solid64)
! MATERIAL PROPERTIES ****************************************
MP,DENS,1,2330 ! Density (Kg/m^3)
!"In-plane free vibration of a single-crystal silicon ring"
! Chia-Ou Chang et al
! Int. J. of Solids and Structures 45 2008 p6114-6132
C11=194.4e+9    !Anisotropic Stiffness matrix values
C12=54.3E+9
C13=44.8E+9
C15=-13.5E+9
C33=204E+9
C44=60.5E+9
C66=70E+9
TB,ANEL,1       !Activate table for anisotropic stiffness matrix
TBDATA,1,C11
TBDATA,2,C12
TBDATA,3,C13
TBDATA,5,C15
TBDATA,7,C11
TBDATA,8,C13
TBDATA,10,-C15
TBDATA,12,C33
TBDATA,16,C44
TBDATA,18,-C15
TBDATA,19,C44
```

```
TBDATA,21,C66
! DEFINE GEOMETRY ********************************************
! Specify keypoints
k,1,0,0,0                 ! K, NPT, X, Y, Z - Defines a keypoint.
k,2,W1/2-W2/2,0,0
k,3,W1/2,L2,0
k,4,W1/2,L1,0
k,5,0,0,thb                 ! K, NPT, X, Y, Z - Defines a keypoint.
k,6,W1/2-W2/2,0,thb
k,7,W1/2,L2,tht
k,8,W1/2,L1,tht
V,1,2,3,4,5,6,7,8
!reuse kps 3,4,7,8
k,9,W1-(W1/2-W2/2),0,0
k,10,W1,0,0
k,11,W1-(W1/2-W2/2),0,thb
k,12,W1,0,thb
V,9,10,4,3,11,12,8,7
VADD,1,2
! MESHING *****************************************************
VSEL,S,,,3
TYPE,1
MAT,1
ESIZE,100e-6, !Specifies element size.
MSHAPE,1,3D   !Choose tetrahedral element shape
VMESH,3
! SOLVE *******************************************************
/SOLU                   !Enter solution processor
ALLS
!ANTYPE,0 !Allow large displacements
DA,2,ALL,UX,,,,,UY,UZ !Apply constraints to base, DOF=0
DA,8,ALL,UX,,,,,UY,UZ
F,1,FZ,load
!F,146,FZ,load  !4mm V - apply force to tip node
!F,186,FZ,load  !5mm V - apply force to tip node
!F,230,FZ,load  !6mm V - apply force to tip node
!F,274,FZ,load    !7mm V - apply force to tip node
!F,318,FZ,load  !8mm V - apply force to tip node
!F,362,FZ,load  !9mm V - apply force to tip node
ALLS
ANTYPE,STATIC              ! Static analysis
SOLVE                       ! Solve current load step
FINISH                      ! Exit active processor
/POST1
!PRNSOL,u,z
/EFACET,1
PLNSOL, U,Z, 0,1.0
! Plot path - tip deflection
PATH,tip01,2,30,20,
PPATH,1,0,w1/2,L2,0,0,
PPATH,2,0,w1/2,L1,0,0,
AVPRIN,0, ,
PDEF,tip01,U,Z,AVG
/PBC,PATH, ,0
```

```
PLPATH,TIP01
PRPATH,TIP01
```

As in the case of the cantilever springs, the *modal* analysis uses the same geometry as the *static* analysis with the following substituted for the meshing and solution steps.

```
! MESHING ************************************************
VSEL,S,,,1
TYPE,1              !element type
MAT,1
MSHKEY,0          ! 0=free mesh
MSHPATTERN,0
MOPT,AORDER,ON
ESIZE,100e-6,         ! divisions set by ESIZE
MSHAPE,1,3D     !0=quadrilateral elements, 1=tetrahedral elements
VMESH,1
! SOLVE ***************************************************
/SOLU                  !Enter solution processor
ALLS
ANTYPE,2  !Modal analysis
MODOPT,SUBSP,1 !Subspace,1 modes
EQSLV,FRONT !Frontal solve5
MXPAND,1 !Expand 1 modes
DA,5,ALL,UX,,,,,UY,UZ !Apply constraints to base, DOF=0
DA,8,ALL,UX,,,,,UY,UZ
SOLVE                        ! Solve current load step
FINISH                         ! Exit active processor
/POST1
SET,LIST
```

Appendix B

The Resonance Frequencies of the Reference Springs

This appendix presents tabulated results of the resonance frequency of the reference springs found using the FE model described in Appendix A and LDV. The V-spring results found using LDV differ from the FE results as the measurements were made after a $420 - 500\mu m$ diameter microsphere was sintered onto the spring tip.

Cantilever Reference Springs

Spring No.	***Spring Length (mm)***	***FEA*** f_0 ***(Hz)***	***LDV*** f_0 ***(Hz)***
1	10	4232	3938
2	10.5	3837	3584
3	11	3496	3294
4	11.5	3197	3056
5	12	2936	2838
6	12.5	2705	2631
7	13	2500	2403
8	13.5	2318	2238
9	14	2155	2084
10	14.5	2008	1950
11	15	1876	1834
12	15.5	1757	1734
13	16	1649	1594
14	16.5	1550	1494
15	17	1460	1397
16	17.5	1377	1328
17	18	1302	1263
18	18.5	1232	1206
19	19	1168	1144
20	19.5	1109	1081
21	20	1054	1028
22	20.5	1003	978
23	21	956	941
24	21.5	912	891

Table B.1: The fundamental resonance frequencies of cantilever reference springs found by FEA and LDV.

V-shaped Reference Springs

Spring No.	***Spring Length (mm)***	***FEA*** f_0 ***(Hz)***	***LDV*** f_0 ***(Hz)***
1	8	8269	7011
2	8.5	7221	6189
3	9	6360	5530
4	9.5	5643	4894
5	10	5041	4380
6	10.5	4530	3978
7	11	4092	3669
8	11.5	3715	3302
9	12	3388	3022
10	12.5	3102	2772
11	13	2850	2576
12	13.5	2628	2391
13	14	2431	2209
14	14.5	2255	2047
15	15	2098	1917
16	15.5	1956	1673
17	16	1829	1480
18	17	1608	1313
19	18	1425	1173
20	19	1272	759
21	24	780	634

Table B.2: The fundamental resonance frequencies of V-shaped reference springs 1-21 found by FEA and LDV with a single $420 - 500\mu m$ diameter microsphere end mass.

Appendix C

Spring Constants

Tabulated spring constants of cantilever reference springs found using the different dimensional, static and dynamic methods. The dynamic added mass method was only applied to some of the reference springs due to time limitations.

Cantilever Reference Springs - Spring Constants

Spring No.	***Spring Length (mm)***	***FEA k (N/m)***	***Euler-Bernoulli k (N/m)***	***Poggi k (N/m)***	***Clifford-Seah k (N/m)***	***Added Mass k (N/m)***	***Static Mass k (N/m)***
1	10	1180	1170	1159	973		1017
2	10.5	1020	1011	1002	850		935
3	11	883	879	871	758		841
4	11.5	772	770	762	692		752
5	12	680	677	671	629		673
6	12.5	601	599	594	567		574
7	13	534	533	528	486	517	501
8	13.5	477	476	471	439	428	469
9	14	428	427	423	396	300	420
10	14.5	385	384	380	360	300	363
11	15	348	347	344	332	292	337
12	15.5	315	314	311	310	273	312
13	16	286	286	283	264	224	290
14	16.5	261	261	258	239	225	255
15	17	239	238	236	213	229	236
16	17.5	219	218	216	200	245	224
17	18	201	201	199	187	202	201
18	18.5	185	185	183	177	193	184
19	19	171	171	169	164		167
20	19.5	158	158	156	149		159
21	20	146	146	145	139		145
22	20.5	136	136	135	129		137
23	21	126	126	125	123		124
24	21.5	118	118	117	112		119

Table C.1: The spring constants of the cantilever reference springs using the various dimensional, static and dynamic methods described in the main text.

Appendix D

TRS610HD Ceramic Properties

The material properties of the TRS ceramic using in the fabrication of the bimorph actuators.

Dielectric and Piezoelectric Properties (±10%)

Property		***TRS610HD***
Relative Dielectric Constant	Free K3	3900
	Clamped K3	1250
	Loss	0.018
Curie temperature	$Tc(^{\circ}C)$	210
Remanent polarisation	$Pr(mCcm^{-2})$	35
Dielectric field strength	$Ec(kVcm^{-1})$	7.8
Piezoelectric charge coefficient	$d_{33}(pCN^{-2})$	690
	$d_{31}(pCN^{-2})$	-340
Electromechanical coupling coeff.	k_{33}	0.8
	k_{31}	-0.46
	k_P	0.73
	k_t	0.56
Frequency constant	$N_{33}(Hzm)$	1300
	$N_{31}(Hzm)$	1414
	$N_P(Hzm)$	1850
	$N_t(Hzm)$	2000
PZT type	PZT 5H Type VI	

Physical and Elastic Properties (±10%)

Property		***TRS610HD***
Density	gcm^{-3}	7.95
Mechanical quality factor	Qm	46
Elastic compliance (constant E)	$S_{33}^E(\times 10^{-11}m^{-2}N^{-1})$	2.11
	$S_{11}^E(\times 10^{-11}m^{2}N^{-1})$	1.65
	$S_{12}^E(\times 10^{-11}m^{2}N^{-1})$	-0.37
	$S_{13}^E(\times 10^{-11}m^{2}N^{-1})$	-0.91
Elastic compliance (constant D)	$S_{33}^D(\times 10^{-11}m^{-2}N^{-1})$	0.77
	$S_{11}^D(\times 10^{-11}m^{2}N^{-1})$	1.31
	$S_{12}^D(\times 10^{-11}m^{2}N^{-1})$	0.71
	$S_{13}^D(\times 10^{-11}m^{2}N^{-1})$	0.24
Stiffness coefficient (constant E)	$C_{33}^E(GPa)$	120
	$C_{11}^E(GPa)$	123
	$C_{12}^E(GPa)$	74
	$C_{13}^E(GPa)$	85
Stiffness coefficient (constant D)	$C_{33}^D(GPa)$	120
	$C_{11}^D(GPa)$	123
	$C_{12}^D(GPa)$	74
	$C_{13}^D(GPa)$	85

Appendix E

Tip Deflection Response of Other Bimorph Actuators

The tip deflection behaviour of the $1.4 \times 2mm$ and $1.4 \times 1.2, 1.7, 2.2mm$ bimorph actuators.

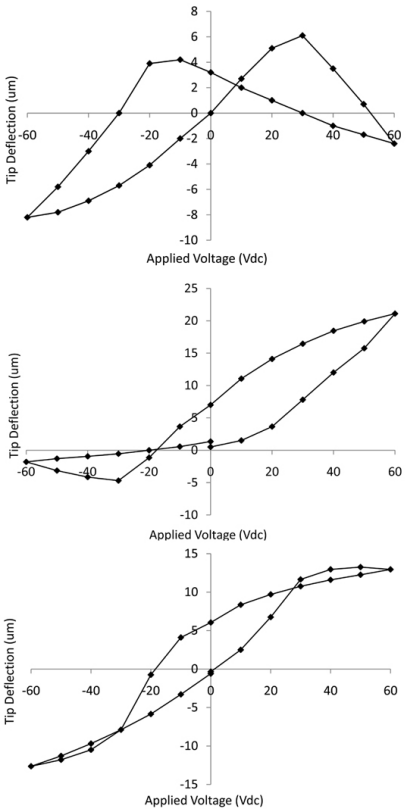

Fig. E.1: The deflection response of a $1.4 \times 2mm$ cantilever during static actuation of the bottom ceramic layer (top), top ceramic layer (middle) and both ceramic layers (bottom).

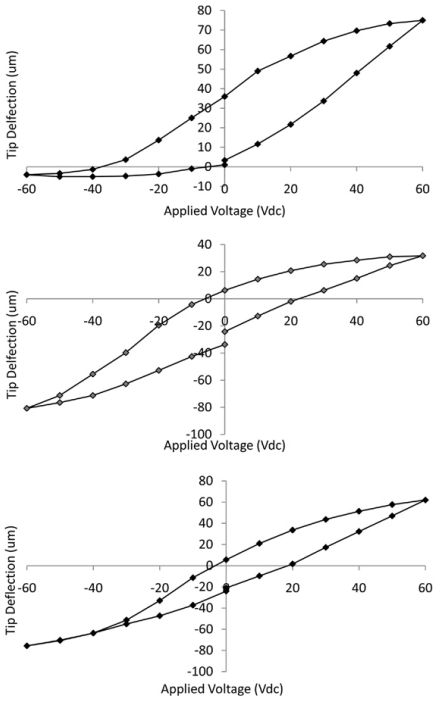

Fig. E.2: The deflection response of a $1.6 \times 3.75mm$ cantilever during static actuation of the bottom ceramic layer (top), top ceramic layer (middle) and both ceramic layers (bottom).

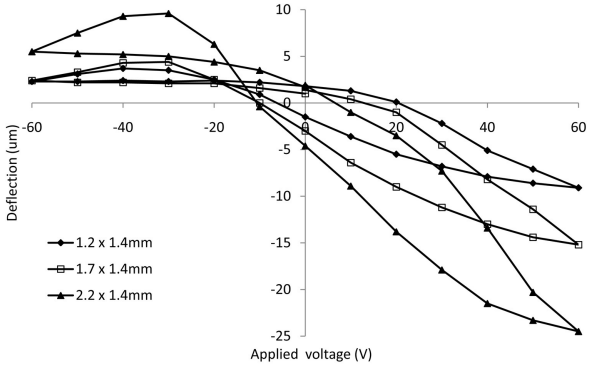

Fig. E.3: The deflection response of the $1.4 \times 1.2, 1.7, 2.2mm$ actuators during static actuation of both ceramic layers (Vmax=60v)

Appendix F

The Wang and Cross Bimorph Model

Tip deflection and blocking force predictions of Wang and Cross' bimorph model for the actuators used in this work.

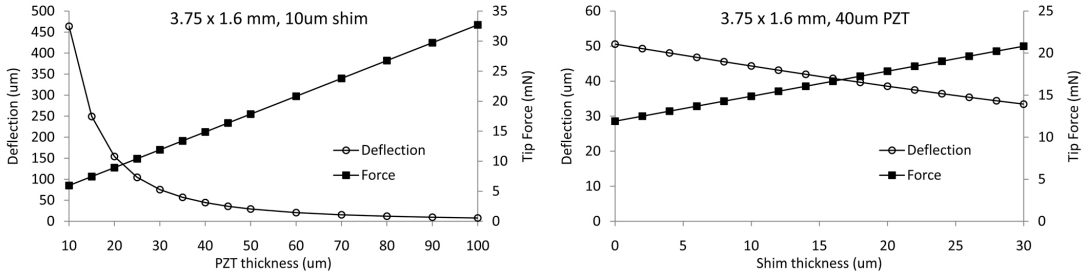

Fig. F.1: Wang and & Cross model - $1.6 \times 3.75mm$ cantilever bimorph actuator.

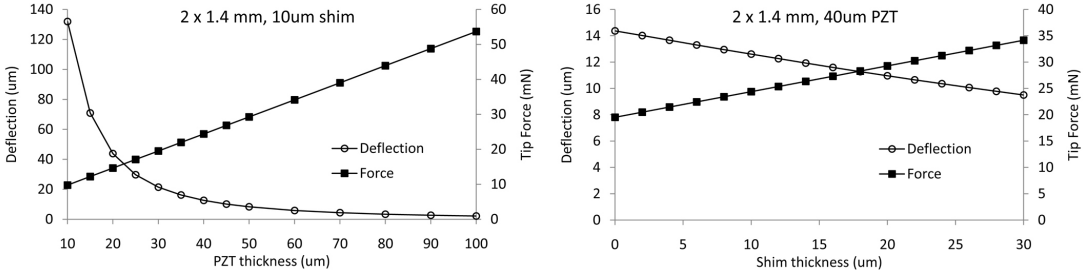

Fig. F.2: Wang and & Cross model - $1.4 \times 2mm$ cantilever bimorph actuator.

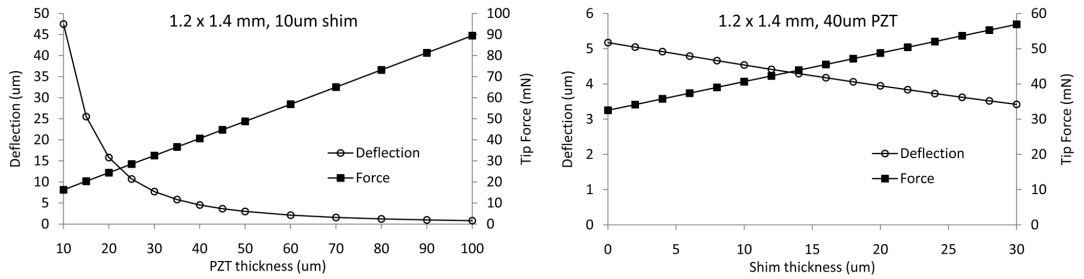

Fig. F.3: Wang and & Cross model - $1.4 \times 1.2mm$ cantilever bimorph actuator.

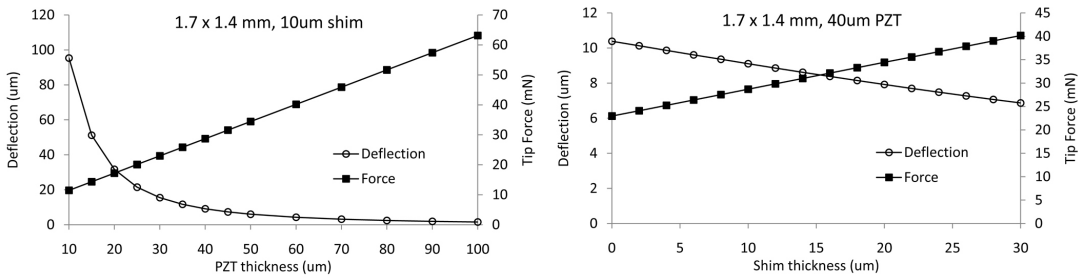

Fig. F.4: Wang and & Cross model - $1.4 \times 1.7mm$ cantilever bimorph actuator.

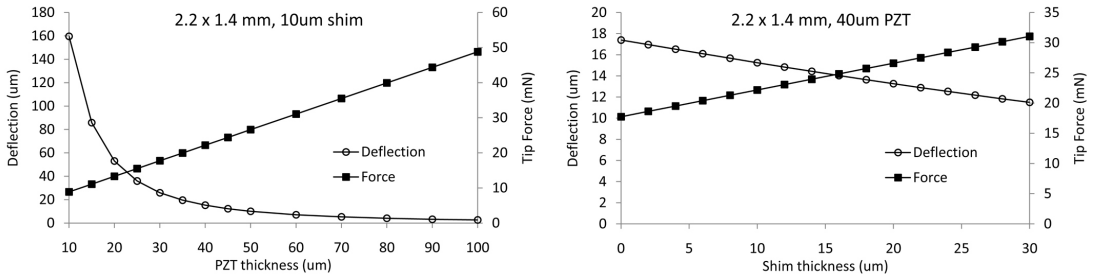

Fig. F.5: Wang and & Cross model - $1.4 \times 2.2mm$ cantilever bimorph actuator.

Appendix G

Other Bending Actuators

A selection of piezoelectric bending type actuators commercially available at the time of writing.

Manufacturer	***Device***	***w*** *(mm)*	***L*** *(mm)*	***t*** *± (mm)*	***Operating Voltage*** *(V)*	***Deflection*** *(μm)*	***Blocking Force*** *(N)*
Noliac [75]	CMBP07	7.8	50	0.7	200	1270	0.4
Steminc [76]	SMBTA352D2T07M	2	35	0.7	160	1300	0.12
Mide [77]	QP20n	25.4	50.8	0.76	200	1.27	0.417
PI [78]	PL112.10	9.6	12	0.65	30	80	2
Face Int. [79]	PAB-4010	10	40	0.55	100	500	0.4
Face Int. [80]	TH-10R	13.7	25.4	0.43	240	70	7

Table G.1: A comparison of some "off-the-shelf" actuators from a variety of manufacturers.